HIGH POWER, HIGH FREQUENCY MODE-LOCKED SEMICONDUCTOR LASERS

VINCENZO PUSINO

UNIVERSITY
of
GLASGOW

A Thesis submitted for the degree of

Doctor of Philosophy (Ph.D.)
Electronics and Nanoscale Group
School of Engineering
December 2013

Alla mia famiglia, con affetto.

We all live under the same sky,
but we don't all have the same horizon.
In an instant age, perhaps we must relearn
the ancient truth that patience, too, has its victories.

— Konrad Adenauer

ABSTRACT

Integrated mode-locked laser diodes are effective sources of periodic sequences of optical pulses, which have always been of great interest for a range of spectroscopy, imaging and optical communications applications. However, some disadvantages prevent their widespread use, such as the restricted tuning of their repetition rate and their output power levels never exceeding a few mW. This thesis reports on the work done to address those limitations. Two main findings are presented, the first being the generation of ultra-high repetition rate optical signals through external injection of two continuous wave signals. This mechanism is much simpler than other techniques previously proposed to increase the repetition rate of monolithic mode-locked laser, and has proved successful in generating optical signals up to quasi-THz. It is based on injection of two continuous wave signals whose spacing is an integer multiple of the pulsed cavity free spectral range and whose injection wavelengths coincide with two of the monolithic laser modes. This technique allows discrete tunability of the repetition rate with a step equal to the injected cavity free spectral range, and the injected laser has been shown to lock up to a repetition rate of 936 GHz, corresponding to 26 times that of the free-running semiconductor laser (36 GHz). The presented scheme is suitable for integration, opening the way for a successful on-chip generation of ultra-high repetition rate optical signals exploiting coupled cavity phenomena.

The second main finding of this thesis regards the changes induced on the pulsed operation of monolithic passively mode-locked lasers by a blue bandgap detuning applied to their saturable absorber. The quantum well intermixing technique has been used for attaining an area-selective bandgap shift on the fabricated chip, being fully post-growth. The lasers with a detuned absorber were found to have an extended range of gain section currents and absorber voltages in which stable mode-locking operation took place. Furthermore, a comparison of mode-locked devices fabricated on the same chip, respectively with and without a bandgap detuned absorber, showed that the emitted pulses had greater peak power and were less affected by optical chirp when the bandgap of the absorbing section was shifted. A new intermixing technique has also been developed as part of this work to address some inconsistencies of the pre-existing one; the newly introduced approach has been found to provide better spatial resolution and a more precise control of the attained bandgap shift.

DECLARATION AND COPYRIGHT

DECLARATION

Unless otherwise acknowledged, the content of this thesis is the original and sole work of the author. No portion of this has been submitted by the author in support of any application for any degree or qualification, at this or any other university or institute of learning. The views expressed in this thesis are those of the author, and not necessarily those of the University of Glasgow.

Glasgow, December 2013

Vincenzo Pusino

COPYRIGHT

PUBLICATIONS

Vincenzo Pusino, Marc Sorel and Michael J. Strain, Generation of ultra-high repetition rate optical pulses through external injection in passively mode-locked monolithical semiconductor lasers. *Laser and Electro-Optics Europe, Conference on, and International Quantum Electronics Conference (CLEO® Europe/IQEC)* 2013, May 2013.

Vincenzo Pusino, Gábor Mezősi, Michael J. Strain and Marc Sorel, Ultra-high repetition rate mode-locking in optically injected Monolithical Semiconductor Lasers, poster presentation, *The Celebration of the* 50^{th} *Anniversary of the Diode Laser Conference*, September 2012.

Vincenzo Pusino, Michael J. Strain, Gábor Mezősi and Marc Sorel, Dynamics of passively mode-locked semiconductor lasers with bandgap shifted saturable absorbers, to be submitted to *Optics Letters*.

Piotr M Stolarz, Vincenzo Pusino, Gábor Mezősi, Lianping Hou, A. Catrina Bryce, Anthony E. Kelly and Marc Sorel, High power and low noise mode-locking operation of Al-quaternary laser diodes, to be submitted to the *IEEE journal of Quantum Electronics*.

Alexandre Delisle Simard, Michael J. Strain, Vincenzo Pusino, Marc Sorel and Sophie LaRochelle, Multiwavelength Laser Based on Superimposed Bragg Gratings on Multiquantum Well AlGaInAs-InP. *Laser and Electro-Optics Europe, Conference on, and International Quantum Electronics Conference (CLEO® Europe/IQEC)* 2013, May 2013.

Ning Zhang, Siyuan Yu, Vincenzo Pusino and Marc Sorel A Photonic Integrated Circuit for the Generation of Tunable and Narrow Linewidth Radio Frequency Signal, 12^{th} *International Conference on Optical Communications and Networks (ICOCN)* 2013, July 2013.

Cosimo Lacava, Vincenzo Pusino, Paolo Minzioni, Marc Sorel, and Ilaria Cristiani, Nonlinear properties of AlGaAs waveguides in CW operation regime, *Optics Express*, Vol. 22, No. 5, pp.5291-5298, Mar. 2014.

Marc Sorel, Michael J. Strain, Vincenzo Pusino, Siyuan Yu, Huanlu Li and Xinlun Cai, Micro-ring resonators for vertical optical emission, *Photonics West* 2014, invited paper.

ACKNOWLEDGEMENTS

Do I have to write acknowledgements? The danger of missing someone out is great, as the temptation to skip the task. That, however, would be an injustice to all the people who contributed to my PhD experience. I'll do my best to remember everyone, blame my recent brain upgrade if you're not mentioned! My thanks go:

To my supervisor, Dr Marc Sorel, for his invaluable support throughout my PhD, and for his informal and direct approach which helped a creative and productive atmosphere.

To Marco, Gabor, Steven, Piotr and Michael, for introducing me to joys and pains of lasers design, fabrication and testing, in between social gatherings and pub nights out.

To all other current and former members of the Optoelectronics group in Glasgow for many useful discussions, especially Barry, Corrie, Philippe and Lianping.

To the staff of the James Watt Nanofabrication Centre, and to the technicians of the Rankine building, especially Bill, keeping the Opto labs running, and Tam, who did countless sputtering runs for me.

To the people who shared the office with me: Olesya, Moss, Carla, Wout, Jehan, Kamran, Azhar, Shahid and Saima, and later Cosimo, Piero, Cui, Khaled, Ope, Ameze and Ifeoma. Many people came and went over the years, but they always tolerated my loud Italian presence, becoming friends other than just officemates.

To all the departmental people met during this adventure, who joined me for countless social events or simply for lunch: Salah, Sankar, Kirsty, Lourdes, Johnny, Sara, Antonio, Laura and Andrea.

To the lucky people who have known me both as friend and flatmate: Marco, Felice, Irmak, Lydia, Guillaume, Sankar and Olesya.

To the WSWD people, Adam, Martin, Nikki, David, Claire, Aisling and Denise, providing a breath of artsy fresh air after many hours in the lab.

To all other people who I know in Glasgow, particularly Marcos, Nina, Maurizio, Becca, Stef, Hatim and Antonella.

To all my friends in Italy who despite years gone by are always there for me, in particular Daria, Erika, Ilaria, Valeria and Eugenia.

To Simone, Gilles and Luca, surely we would raise Ichnusas to celebrate, if only it were possible.

To my one and only Dorogaya.

To the surgeons of the Southern General Hospital, for most likely saving my life.

And finally, but most importantly, to my family, alla mia famiglia perché c'é sempre stata e so che ci sará sempre.

CONTENTS

LIST OF FIGURES

LIST OF TABLES

ACRONYMS

ACPML Anti Colliding Pulse Mode-Locking

AR Anti-Reflection

BAL Broad Area Laser

BR Butt-joint Regrowth

CCML Compound Cavity Mode-Locking

CMOS Complementary Metal Oxide Semiconductor

CPML Colliding Pulse Mode-Locking

CW Continuous-Wave

DBR Distributed Bragg Reflector

DFB Distributed feedback

DMLD Discrete Mode Laser Diode

EBL Electron Beam Lithography

EDFA Erbium-Doped Fibre Amplifier

EPSRC Engineering and Physical Sciences Research Council

FBG Fibre Bragg Grating

FP Fabry-Pérot

FRL Far-Field Reduction Layer

FROG Frequency Resolved Optical Gating

FSR Free Spectral Range

FWHM Full-Width at Half Maximum

FWM Four-Wave Mixing

GRINSCH GRaded INdex Separate Confinement Heterostructure

HF Hydrofluoric Acid

HR High-Reflectivity

HSQ Hydrogen SilsesQuioxane

IAC Intensity Auto-Correlation

ICP Inductively-Coupled Plasma

ICR Intra-Cavity Reflector

IFVD Impurity Free Vacancy Disordering

IID Impurity Induced Disordering

IPA Iso-Propyl Alcohol

JWNC James Watt Nanofabrication Centre

LI Light-Current(I)

LPCVD Low Pressure Chemical Vapour Deposition

MIBK Methyl Iso-Butyl Ketone

ML Mode-Locking

MLA Multi Laser Array

MLL Mode-Locked Laser

MMI Multiple Mode Interference

MO Master Oscillator

MOPA Master Oscillator Power Amplifier

MQW Multi-Quantum-Well

OQW Offset Quantum-Wells

OSA Optical Spectrum Analyser

PA Power Amplifier

PECVD Plasma Enhanced Chemical Vapour Deposition

PL Photo-Luminescence

PML Passive Mode-Locking

PMLL Passively Mode-Locked Laser

PMMA Poly Methyl Meth-Acrylate

QCSE Quantum Confined Stark Effect

QW Quantum-Well

QWI Quantum-Well Intermixing

RF Radio-Frequency

RIE Reactive Ion Etching

ROW Resonant Optical Waveguide

RTA Rapid Thermal Annealing

SA Saturable Absorber

SAG Selective Area Growth

SCPML Self Colliding Pulse Mode-Locking

SCOWL Slab-Coupled Optical Waveguide Laser

SEM Scanning Electron Microscope

SISA Selective Intermixing in Selected Areas

SL Semiconductor Laser

SMSR Side-Mode Suppression Ratio

SOA Semiconductor Optical Amplifier

SOI Silicon-on-Insulator

SP Self-Pulsation

SRIM Stopping and Range of Ions in Matter

SRL Semiconductor Ring Laser

TBP Time-Bandwidth Product

TE Transverse Electric

TEC Thermo Electric Cooler

TM Transverse Magnetic

TMAH Tetra-Methyl-Ammonium Hydroxide

3QW Three Quantum-Well

5QW Five Quantum-Well

Part I

THESIS BACKGROUND

The first part of this thesis outlines the theoretical background of the project, reviews the literature on high power and high frequency semiconductor mode-locked lasers and provides an overview of the fabrication methods used for devices implementation, with particular attention to the quantum well intermixing technique.

1 INTRODUCTION

The work described in this thesis is part of the project *High Power, High Frequency Mode-locked Semiconductor Lasers* [1], funded by the Engineering and Physical Sciences Research Council (EPSRC). The purpose of the project is to provide compact and low cost devices for the generation of ultra-short and highly energetic pulses with high repetition rates.

Monolithic pulsed optical sources at frequencies in the hundreds of GHz range and beyond are of interest for next generation optical communications networks, as well as for sensing and security applications [2]. The EPSRC project developed devices operating over the two main wavelength windows centred at 800 nm and 1550 nm. These two spectral regions are of importance because they constitute, respectively, the wavelength operating range in short and long haul fibre optics communications systems. Moreover, the excellent power performance of semiconductor lasers operating over the 800 nm wavelength range make them suitable candidates for THz generation and nonlinear applications. The work described in this thesis refers to the second window, with central wavelength of 1550 nm.

Within the EPSRC project frame, this PhD project focussed on two main themes:

1. The generation of quasi-Terahertz rate optical pulses from semiconductor Passively Mode-Locked Lasers (PMLLs) through two main approaches, the first exploiting injection locking through external injection of continuous wave signals and the second based on mutual coupling between two integrated Semiconductor Ring Lasers (SRLs) through the Vernier effect.

2. The increase of the emitted average power in the mode-locked region from few mW to few tens of mW, in order to boost the energy of the optical pulses in PMLLs. This has been sought by bandgap shifting of the saturable absorber.

The reasons for targeting these two particular aspects will be explained in the next paragraph.

1.1 PROJECT MOTIVATION

The devices studied in this project are fabricated on standard Multi-Quantum-Well (MQW) semiconductor epi-layers[1] based on an alu-

1 www.iqep.com

minium quaternary compound. This MQW material has been extensively used at the University of Glasgow for the fabrication of a number of devices, such as Distributed feedback (DFB) lasers [3], Semiconductor Ring Lasers (SRLs) [4], and devices based on Fabry-Pérot (FP) geometries for mode-locked operation [5]. The Mode-Locking (ML) dynamics of this material platform are well understood in the Optoelectronics group at the University of Glasgow following extensive characterisation [6, 7]. Such analysis has proved these devices as very attractive sources of ultra-short optical pulses [5].

However, one of their major drawbacks is the output power performance because optimum ML happens for relatively low current injection. Even considering higher current regions where poor quality ML can still be achieved, the average emitted power does not exceed few tens of mW [8]. This constraint has prevented a wider diffusion of semiconductor PMLLs operating over the 1550 nm wavelength range, since a number of reasons make high output power desirable, e. g. eliminating the need for optical amplification, thus improving noise performance and expanding the possible range of applications. Despite very active research in the field the performance of monolithic mode-locked devices is still limited, especially in comparison to their solid-state or fibre counterparts which easily achieve output powers of a few Watts [9]. There have been several attempts to increase the emitted power [10], but none of the approaches proposed so far has been able to tackle the issue effectively, or to gain a leading edge over the other ones. The method of choice for future PMLLs has not been clearly defined yet. There are several routes for increasing the peak power of the ML peak power, but they can be divided in two groups:

1. The techniques focussing on the design of epi-layer structures especially targeted for optimised mode-locked operation, for example through mode expander layers [11].

2. The techniques targeting an increase of the pulses peak power by changing the interplay between the different sections within the cavity, either through bandgap engineering (like the Quantum-Well Intermixing (QWI) technique [12], introduced later in this chapter), or through the introduction of wavelength-selective elements within the laser cavity (e.g Distributed Bragg Reflectors (DBRs) [13]).

Another topic which has seen a substantial research effort over the years is the realisation of passively mode-locked monolithic devices that could produce ultra-short optical pulses with ultra-high repetition rates (hundreds of GHz). Tuning of the pulse train frequency would also be desirable, adding flexibility and reconfigurability to the continuously evolving scenario of possible applications. The maximum achievable repetition rate is limited to few tens of GHz when considering the most elementary monolithic passively mode-locked

design, based on a single FP cavity incorporating an element with saturable absorption characteristics. The technical impracticability of cleaving devices shorter than few hundreds of microns limit the maximum achievable repetition rate to approximately 100 GHz for the considered material platform. Moreover, an accurate definition of the repetition rate as required by some applications might prove problematic because of the limited resolution of conventional scribing tools. Very short devices can be implemented through wet-etch facilitated cleaving processes and high-precision automated scribers but they would suffer low gain and be limited in terms of maximum attainable power. The difficulties in attaining high repetition rates and the lack of tunability clash with the needs of next generation optical communication networks, and several emerging applications such as metrology and THz generation. Several methods and techniques have been proposed over the years to bring the repetition rate to values greater than the cavity Free Spectral Range (FSR), with most of the proposed solutions relying on multiple cavity geometries, thus complicating the fabrication and operation of the lasers, as it will be described later in this chapter.

With the described issues in mind, the present work has focussed on techniques and methods to attain effective ML at ultra-high repetition rates (hundreds of GHz) while at the same time providing wide tunability (from $\sim$ 36 GHz, the fundamental mode spacing of the laser diodes used in this work, to quasi-THz frequencies) and solutions suitable for integration. The proposed scheme relies on external injection of continuous wave optical signals and will be detailed in Chapter 3. The rest of this chapter instead will provide a brief introduction to ML, from the basic mechanism to an outline of the methods proposed so far to boost the repetition rate and output power performance. Also the Injection Locking theory and the QWI phenomenon will be discussed, as they constitute the basis on the original work reported in this thesis is based.

1.2 MODE LOCKING

ML is a pulse generation technique based on the introduction of a fixed phase relationship between different longitudinal modes in a laser, first proposed in [14]. The theoretical analysis reported here is based on the one reported in [15].

For simplicity the considered device will be a laser emitting on a single transverse mode and oscillating at $N = 2m + 1$ longitudinal modes. ω_0 is the frequency of the mode at the centre of the gain bandwidth curve, and $2\pi/t_r$ is the frequency spacing between adja-

cent modes, with t_r being the cavity round trip time. The electric field $E(t)$ in the time domain can be expressed as:

$$E(t) = \sum_{n=-m}^{m} E_n e^{i[(\omega_0 + n\frac{2\pi}{t_r})t + \varphi_n]} \tag{1.1}$$

with E_n and φ_n being, respectively, the electric field and the phase associated with the n^{th} mode. Without imposing a fixed phase relationship between the modes, each one of them oscillates independently and the resonator output presents a Continuous-Wave (CW) output with random fluctuations in the time domain. In a mode-locked scenario, all the phases are the same, so if one assumes the centre mode to have zero phase, this is true for all the modes ($\varphi_n = 0$). If one also assumes for simplicity all modes to have equal strength ($E_n = E_0$) the electric field summation can be expressed as:

$$E(t) = E_0 \sum_{n=-m}^{m} e^{i(\omega_0 + n\frac{2\pi}{t_r})t} \tag{1.2}$$

The associated intensity can be derived from the electric field, leading to the following expression:

$$I(t) = E(t)E^*(t) = E_0^2 \frac{sin^2(N\pi t/t_r)}{sin^2(\pi t/t_r)} \tag{1.3}$$

The evolution of intensity over time is shaped as a series of short pulses propagating between the resonator mirrors, with a time separation between two successive pulses corresponding to the cavity round-trip time. The temporal width of the pulses is inversely proportional to the number of longitudinal modes lasing, as Figure 1.1 shows. The sharp increase in intensity as more modes are locked is due to the assumption of all of them having equal strength ($E_n = E_0$); a more realistic model would have the field amplitudes changing according to the gain profile, with a Gaussian function being a typical envelope.

Depending on the method of choice to induce a fixed phase relationship between the longitudinal modes, one can distinguish between active and passive ML [16]. Active ML is based on external gain modulation at the desired repetition rate, whereas passive ML exploits an intra-cavity nonlinear element, normally a Saturable Absorber (SA), which locks the modes in phase. Pulses may be obtained also by combination of the two techniques, in a configuration known as hybrid mode-locking. Performance in actively Mode-Locked Lasers (MLLs) is limited by the speed of the electronic signal generator used to modulate the gain. In PMLLs it is the pulse itself which modulates the absorption: this allows much shorter pulses compared to active ML.

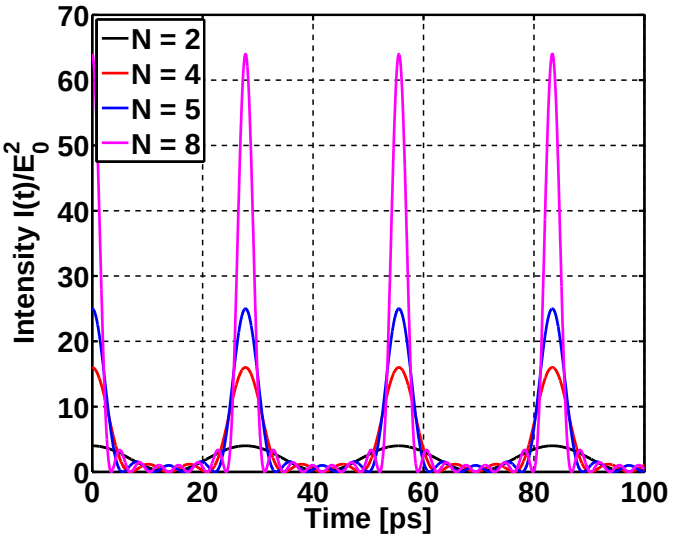

Figure 1.1: Normalised electric field intensity vs. time for a pulse repetition rate of 36 GHz, showing the intensity and pulse width dependence on the number of modes locked, N.

A further classification of PMLLs identifies two main categories, depending on the ratio between the SA recovery time and the width of the generated pulse [17]. When the intra-cavity pulse energy is much lower than the saturation energy of the gain medium, the generated net gain window must not exceed the pulse duration: it is up to the absorber to bring the losses back to a high level rapidly. This case is known as fast SA ML, and it generally applies to solid-state lasers [18]. In semiconductor lasers the pulse has enough energy to saturate the gain medium and, if the absorber has lower saturation energy, then a short net gain window can still arise, which is closed by the pulse itself as it bleaches the gain. This case is known as slow SA ML, and its pulse formation mechanism is almost independent of absolute recovery times, as long as the absorber recovers faster than the gain [19]. Since the devices studied in this work fall in the slow SAs category, a more detailed description of this case will follow.

1.2.1 *Slow Saturable Absorber Passive Mode Locking*

Semiconductor lasers usually have large gain cross sections, therefore intra-cavity pulse energies may become large enough to saturate the gain in a single pass. In order to allow pulse formation, there needs to be a net gain window, which only occurs if the absorber reaches saturation before the gain. This situation is illustrated in Figure 1.2.

The pulse formation mechanism can be qualitatively explained as follows [20]; noise is present in the pumped cavity, and the electric field displays incoherent fluctuations with randomly varying intensity. The fluctuating components with high intensity experience

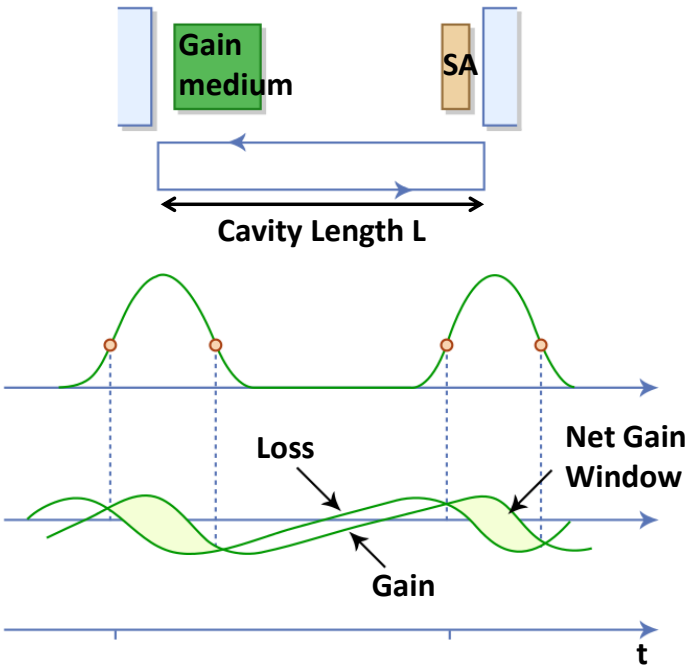

Figure 1.2: Temporal evolution of gain, losses and optical power in a passive ML device.

less loss due to the nonlinear absorption characteristics of the SA, so that their amplitude builds up at every round trip. On the contrary, the low intensity components are strongly attenuated. Eventually the laser reaches a steady state with a single pulse travelling in the cavity. In the narrow time window where the gain exceeds the loss, various phenomena contribute to pulse shaping, the first being that on the leading edge of the pulse the absorber is not yet saturated and losses are high. In the centre of the net gain window, the pulse intensity increases, the SA is bleached and amplification occurs. Eventually the energy of the pulse becomes high enough to deplete the gain, thus by this time the SA has begun to recover and losses are high again. This temporally corresponds to the trailing edge of the pulse.

In order for this mechanism to lead to a stable train of pulses, the device must satisfy some conditions, primarily that the SA should recover faster than the gain section. This means that the temporal evolution of losses and gain within the cavity should lead to the gain exceeding the loss only over a limited temporal frame. The recovery times of semiconductor SAs on MQW material platforms are generally greater than typical cavity round trip times, but there are several techniques to overcome this issue. The most widely adopted and standardised one is the split contact technique [21], which relies on dividing the laser cavity into two sections, with the longer one forward biased and the shorter one reverse biased, referred to, respectively,

as the gain and the SA section. Generally the optimum ratio between the absorbing length and the amplifying one is a few percent. The application of an adequate reverse voltage to the SA section reduces the recovery time, ensuring the previous condition is satisfied and that ML can take place. Another requirement regards the energy of the intra-cavity pulse, that always needs to be greater than the saturation value of both absorbing and gain sections, so that both can be bleached by the pulse in a single pass. Moreover, as previously stated, the saturation energy of the absorber should be less than that required to deplete the gain for the SA to saturate before the gain. In MQW systems this condition is always verified, since the saturation energy of a given section is inversely proportional to the differential gain; thanks to the nonlinear relationship between gain and carrier density a short SA section will always have higher differential gain than a long amplifying one.

The description of the mechanisms underlying passive ML in semiconductor lasers has so far been intentionally qualitative. It is worth mentioning that several fast nonlinearities, like dynamic carrier heating [22] and spectral hole burning [23] play an important role in the pulse shaping mechanism, especially for short pulse widths, but an in-depth analysis of those phenomena goes beyond the scope of this work, whose focus is on high power and high frequency semiconductor lasers. For this reason the next paragraphs will review the main techniques to generate optical pulses with high repetition rate and high energy.

1.3 GENERATION OF HIGH REPETITION RATE OPTICAL PULSES

The minimum length of a FP semiconductor laser resonator is limited by cleaving to a few hundreds of microns and therefore the highest repetition rate cannot exceed 100-150 GHz. Particular conditions can induce the simultaneous formation of multiple pulses travelling within the cavity, with equal temporal spacing, in what is known as harmonic ML. Several ways to lock a semiconductor PMLL at harmonics of its fundamental frequency exist, but they all share the same challenge, which is obtaining a pulse train with constant pulse energy and low timing jitter. Temporal instability is often related to the so-called *supermode* noise [24], which arises from the fact that N pulses are travelling inside the cavity, but only the N^{th} resonator mode is excited. The laser does not oscillate on a stable set of modes and might jump to a different one, or simultaneously oscillate on two sets of modes. Various methods can be adopted to suppress this kind of instability and achieve stable harmonic ML. Historically the first two techniques that have been introduced for semiconductor PMLLs are the so-called Colliding Pulse Mode-Locking (CPML) [25] and the Compound Cavity Mode-Locking (CCML) techniques [26]. More recently, passive ML

of Discrete Mode Laser Diodes (DMLDs) has been reported [27], showing some promising results. The strengths and weaknesses of each of these techniques will be discussed in further detail in the following paragraphs.

1.3.1 *Colliding Pulse Mode-Locking*

CPML was originally introduced as a mean to generate ultra-short, transform limited pulses in dye lasers [28]. This ML technique exploits the interaction of two counter-propagating pulses in a medium with saturable absorption characteristics, as Figure 1.3 illustrates for the case of CPML implementation in a monolithic device, with a semiconductor SA placed in the middle of the cavity.

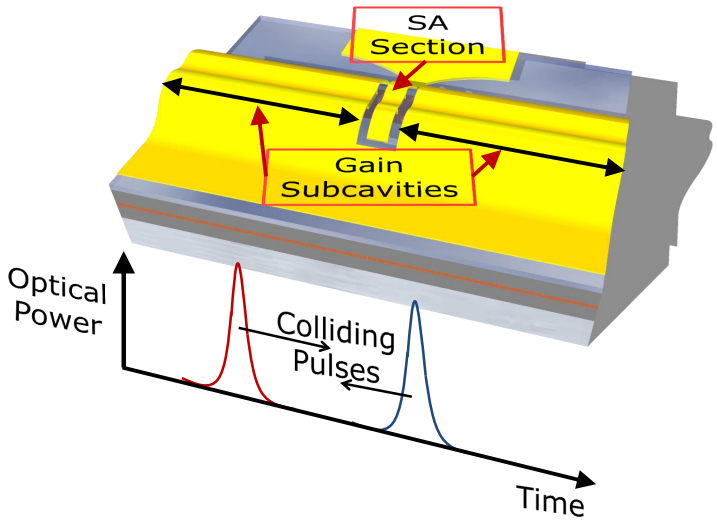

Figure 1.3: Schematic depicting the CPML mechanism in a monolithic cavity geometry: the two pulses colliding in the SA placed in the centre of the cavity leads to the device operating at twice the fundamental repetition rate.

In order to achieve effective CPML, a number of conditions must be satisfied, the first being that the pulses must overlap within the absorber, their difference in arrival time between them must be small compared to the SA optical length. Furthermore, as with ML at the fundamental frequency, the physical length of the SA must be shorter than the optical pulses. Considering the situation with a single SA and two sub-cavities, the SA optimum location is at the centre of the cavity, so that coupling between colliding pulses is maximised. Given the device configuration, the fundamental repetition rate for CPML is two times the round trip frequency of the whole cavity when using a single SA. Devices with multiple absorbers have been demonstrated to lock successfully at the corresponding harmonics of the fundamental frequency [29]. The occurrence of CPML is due to the fact that the total energy of the system is minimised when the counter-propagating

pulses synchronously propagate in the SA, thus minimising the losses of that section. Monolithic CPML are compact light sources which have proven thermally and mechanically very stable, and have provided pulses with a range of repetition rates from tens of GHz to 350 GHz, both at 800 nm [30] and at 1550 nm [31].

The pulse formation mechanism in CPML devices has been widely studied, and it differs depending on the type and geometry of mode-locked laser considered. In dye lasers, where CPML was first observed, the considered geometry was a bidirectional ring with the two pulses establishing a standing wave and bleaching a grating into the medium when colliding in the SA [32]. This interpretation was also applied when Zhang and Carroll introduced a pulse shaping model for MQW laser diodes [33]: the interaction of the counter-propagating pulses was thought to lead to a carrier-density grating in the SA, resulting in the forward and backward travelling waves being coupled. Such a model predicted the generation of transform-limited optical pulses, in disagreement with the experimental results which showed highly chirped pulses from MQW laser diodes [34]. Later Bischoff et al. suggested the pulse formation to be determined by the interplay between the gain and absorber dynamics [35]. According to this analysis, the pulse broadens in the gain section and is compressed in the absorber, until attaining equilibrium once in steady-state regime. This implies that for MQW materials CPML does not fall purely under the slow SA case, because both slow and fast gain/absorber dynamics are needed. A slow absorber is required for the system to self-start, while a fast one is important for sustaining ML in steady-state. This is especially true when aiming for very high repetition rates, because the round trip of a short cavity might be shorter than typical absorption recovery times, and sub-picosecond phenomena like dynamic carrier heating and spectral hole burning become instrumental for successful pulse formation.

With regards to the pulse quality, results from MQW CPML laser diodes have usually shown almost linearly down-chirped pulses [35], as a result of opposite carrier density induced index changes in the gain and absorber section. Because of the opposite carrier dynamics, the chirp that the pulse experiences in the gain section is partially counterbalanced by the SA. However, increasing the absorber length is not beneficial, as it causes an increase in the amplification needed for effective ML and results in the pulse being more chirped. Effective chirp control has been achieved through hybrid ML, which has been shown to produce downchirped to upchirped pulses by varying the modulation frequency when applied to a monolithic CPML configuration [36].

Devices employing colliding-pulse techniques to increase the repetition rate have been fabricated on the same material platform used in this work, and the experimental results are consistent with the pulse

shaping mechanism illustrated. The lowest time-bandwidth product reported, 0.5, is higher than the transform limited value of 0.31 for $sech^2$ pulses, which is the characteristic pulse-shape usually obtained from monolithic MQW mode-locked laser diodes [37]. The repetition rate achieved ranges from 20 GHz, demonstrated for relatively long devices with a single SA [38], to 160 GHz, observed for a quasi-40 GHz cavity that includes three symmetrically placed SAs [39]. In high-harmonic ML devices, CPML lasers have a generally poor ML performance over CCML devices, whereas their strength is in their superior tolerance to cleaving inaccuracies. These aspects will be explained in the next section, which analyses CCML.

1.3.2 *Compound Cavity Mode Locking*

The first demonstration of harmonic ML in semiconductor PMLLs was based on an intra-cavity DBR section, introduced to create a sub-cavity and induce locking at higher harmonics [40]. For low pumping currents the lasers showed ML at the fundamental repetition frequency of the entire cavity, whereas at higher currents the devices switched to a regime where a train of shorter pulses at the round-trip frequency of the sub-cavity was generated.

The operation principle is based on the DBR section introducing a coupled-cavity inside the main resonator, that works as a frequency filter, enhancing only those frequencies which coincide with the mode spacing of the coupled-cavity. By choosing the length of the DBR section so that there is an integer ratio between the two segments, one can design the repetition rate at which harmonic ML will take place. Furthermore, ML at multiples of the DBR fundamental mode spacing is possible for higher carrier injection because a higher number of modes will be above the lasing threshold. Using this technique, successful ML at 400 GHz, 800 GHz and 1.54 THz in a MQW material structure emitting at 1550 nm was demonstrated by using a DBR section with 400 GHz mode spacing, under different biasing conditions of the gain section [41, 42]. Avrutin et al. proposed an Intra-Cavity Reflector (ICR)-basedCCML, implemented by etching a groove inside the main resonator cavity to form an additional Fabry-Pérot sub-cavity [43] as an alternative to the DBR section. They also derived an expression for cavity losses and showed how the cavity can mode-lock at the M^{th} harmonic with the reflector relative position being either at $1/M$ of the cavity length, or in a more general case, dividing the cavity into two segments L_1 and L_2 satisfying $L_2 = L_1 * (M_2/M_1)$, with M_1 and M_2 integer numbers with no common factors, chosen so that $M = M_1 + M_2$. In both cases the losses have a minimum for the resonator oscillating at the M^{th} harmonic.

The fact that the cavity losses have a minimum for the system oscillating at a certain harmonic is beneficial to the modal selectivity. A

CCML laser favours a fixed set of modes, therefore it is less affected by *supermode* noise. Here lies one of the advantages of the CCML construction over the CPML one, because in the latter the higher harmonic selection mechanism is essentially due to the non-linear interaction between the colliding pulses, which selects an interval between resonator modes but does not exactly select the ones excited. This makes the CPML mechanism intrinsically more affected by supermode noise [44]. Furthermore, in CCML laser diodes the modal selectivity can be improved by using more than one ICR. Different reflectors can be positioned at different fractions of the cavity length, each of them sharpening the spectral selectivity of the other and eventually achieving ML at the M^{th} harmonic.

The first experimental characterisation of CCML laser diodes with ICRs employed devices lasing at $\lambda = 860$ nm, which were shown to mode-lock up to a repetition rate of 2.1 THz [45]. On 1.55 µm material platforms the maximum achieved repetition rate so far is 160 GHz, achieved by using two sub-cavity ICRs [46]. The use of multiple ICRs improves the modal selectivity but adds complexity to the devices as well, making fabrication less tolerant. CCML is indeed very dependent on accurate sub-cavity length ratios, especially when ML is required at higher order harmonics. The accuracy of a conventional wafer scriber (few µm) is typically not enough and a successful fabrication might demand additional wet-etch facilitated or computer-controlled cleaving processes. The great degree of complexity both in designing and fabricating this kind of mode-locked lasers proves to be the greatest disadvantage of the CCML technique. One possibly simpler method which can be used to achieve harmonic ML in semiconductor PMLLs is the so-called discrete mode-locking, addressed in the next paragraph.

1.3.3 *Discrete Mode Locking*

The FP geometry is undoubtedly the most simple laser geometry. It is very convenient to fabricate, but it is also unsuitable for many applications, because the mode selectivity is provided only by the gain curve and many longitudinal modes happen to be above lasing threshold. In Discrete Mode Laser Diodes (DMLDs), the standard FP geometry is modified so that one can tailor the modes oscillating in the resonator, in order to achieve single-mode or multi-wavelength operation [47]. DMLDs were firstly introduced to achieve single mode emission with a very narrow linewidth in a FP cavity structure [48, 49]. This was achieved by introducing small refractive index changes by etching a given number of shallow grooves distributed along the resonator cavity. The grooves modify the FP cavity losses, enhancing one mode and suppressing the others, since introducing light scattering regions distributed along the laser ridge waveguide alters the threshold gain value of the single modes and only those with reduced gain threshold

will lase. The use of this technique has shown very narrow linewidth emission with very high Side-Mode Suppression Ratio (SMSR). Selecting the right set of modes will results in ML at higher harmonics of the fundamental. The shallow etched grooves as a whole can be viewed as a distributed reflector which adds a perturbation on the FP modes pattern. Normally for the process to be effective several tens of etched grooves are required (which might be impractical). This mechanism actually provides a precise tailoring of the emission spectrum, allowing also to design multi-wavelength FP lasers [50]. The number and spacing of the oscillating longitudinal modes can be pre-determined by design, and this of course makes them suitable candidates for ML at very high repetition rates.

Passive Mode-Locking (PML) in DMLDs has been demonstrated, both with a pulsed output at 100 GHz repetition rate [51], or with a sinusoidal output at 160 GHz [52]. Their timing jitter performance has also been compared with standard semiconductor PMLLs, and DMLDs show comparable or better timing jitter performance, probably due to the spectral filtering mechanism in the cavity [53]. PML in DMLDs could however be hindered by wavelength bistability, since the standard design for harmonic ML in DMLDs favours lasing of just two modes, whose spacing defines the repetition rate. The wavelength instabilities arising when selecting just two modes could be avoided by designing devices supporting a higher number of modes, even though such solution would require more grooves more densely placed, eventually making the fabrication cumbersome. Furthermore, etching too many features inside the cavity would cause an increase in the scattering losses seen by the lasing modes, limiting the maximum achievable output power.

In conclusion, none of the ultra-high repetition rate techniques described so far has prevailed over the others. One current research trend in the field is the combination of two or more of the previously illustrated approaches, for example by superimposing a CPML geometry with multiple SAs on top of a DMLD. A highly desirable feature for monolithic mode-locked lasers is the tunability of the repetition rate, since tunability in monolithic devices was one of the main goals of this work, together with investigating possibilities to increase the PMLLs emitted power, which is object of the next section.

1.4 INJECTION LOCKING

The techniques in the previous paragraph were reported for completeness; however, the quasi-THz repetition rate signals obtained in this work exploited the interaction between three separate laser oscillators, with two CW signals coupled into a mode-locked cavity. This paragraph therefore discusses the dynamics of semiconductor lasers when perturbed by an external signal.

The behaviour of an harmonic oscillator subjected to injection from an external one varies depending on the strength of the injected signal and on the difference between the oscillating frequencies. One case of particular interest is when the conditions are such that phase synchronisation is achieved between the two oscillators, in what is normally referred to as injection locking. Locking phenomena between oscillators were first observed by Huygens in pendulum clocks three centuries ago [54], and much later (1946) by Adler in Radio-Frequency (RF) electric circuits [55]. Soon after the appearance of laser oscillators, injection locking phenomena between two lasers through light injection were also demonstrated [56]. Phase synchronisation is not the only possible outcome when light is injected into an optical cavity, there is a wide range of effects taking place, which will be discussed in this paragraph. The discussion here focusses on the theoretical analysis of the injection locking phenomenon based on what reported in [57]; the experimental observations of injection locking reported so far are the object of the introductory part of Chapter 3.
The dynamic behaviour of a "slave" single-mode semiconductor laser when subjected to external injection from a "master" source is a function of the relative frequency detuning $\Delta\omega$ and of the injection level K, i.e. the relative power of the injected signal with respect to the power output of the unperturbed slave device. The way the slave device responds to the injected light varies across different regions of the parameter space K-$\Delta\omega$, identifying different zones of operation for the slave, and specifically:

1. *Stable Locking Zones*, where the two lasers are locked in phase.
2. *Beating Zones*, where the slave laser is amplitude modulated at the detuning frequency but no phase synchronisation is present.
3. *Self Pulsation Zones*, where the field of the slave laser oscillates at the relaxation frequency.
4. *Chaotic Zones*, where the oscillation of the slave laser becomes chaotic and displays multiperiodicity regimes and period doubling.
5. *Coherence Collapse Zones*, with the slave laser displaying a broadening in its optical spectrum due to strong phase fluctuations.

The listed phenomena can be modelled analytically. The equations describing a semiconductor laser with external optical feedback were first derived in [58], with the optical feedback provided by an external mirror. That set of equations can be modified to represent injection from a master semiconductor laser into a slave device, obtaining the following:

$$\frac{dE_l}{dt} = \frac{1}{2}[G_n(N_l - N_0) - 1/\tau_p]E_l + \frac{K}{\tau_{in}} E_{inj}\, cos\phi \tag{1.4}$$

$$\frac{d\phi}{dt} = \frac{1}{2}\alpha[G_n(N_l - N_0) - 1/\tau_p]E_l - \frac{K}{\tau_{in}} \frac{E_{inj}}{E_l}\, sin\phi - \Delta\omega \tag{1.5}$$

$$\frac{dN_l}{dt} = R_p - \frac{N_l}{\tau_S} - G_n(N_l - N_0)E_l^2 \tag{1.6}$$

Equation 1.4 includes the amplitude and phase of the slave laser electric field, E_l and ϕ respectively, as well as its population inversion N_l, differential gain G_n, carrier density at transparency N_0 and photon lifetime τ_p. The injection term in equation 1.4 contains, besides the injection strength parameter K, also the amplitude of the master laser electric field E_{inj} and the round-trip time of the cavity τ_{in}. Other important quantities present in equation 1.5 and 1.6 include the linewidth enhancement factor α, the pump parameter R_p (defining how efficiently carriers are excited within the active region) and the recombination time τ_S. The system represented by this set of equations is single-mode and quasi-monocromatic, so it cannot include complex phenomena such as four-wave mixing or wavelength bi-stability; however, it does include all phenomena listed previously. For weak injection ($K < 0.01$) it is possible to find the locked stationary solutions of the system analytically, and to define the injection locking region boundaries, identified by the following equation:

$$\Delta\omega = \begin{cases} \frac{K}{\tau_{in}} & \text{if } \Delta\omega > 0 \\ -\frac{K}{\tau_{in}}\sqrt{1+\alpha^2} & \text{if } \Delta\omega < 0 \end{cases} \tag{1.7}$$

This equation describes two lines in the parameter space K-$\Delta\omega$ which delimit the region where the master and the slave laser are locked. the boundaries of the locked region are depicted in blue in Figure 1.4. The different slope of the two curves is due to the presence of the linewidth enhancement factor α in the second part of the equation, and this explains why injection locking of a semiconductor laser is more likely to happen if the master laser is negatively detuned with respect to the slave. The points outside the boundaries defined by the two curves are those for which only a beating takes place between the master and the slave laser. This is typical of regions in the parameter space either with excessive detuning and/or too weak injection. Within the locking region the stability boundary of the system can be found, defined by the hyperbole depicted in red in Figure 1.4. Moving the analysis from weak to moderate injection ($0.01 < K < 0.1$) the slave laser goes through the following regimes: first it displays an oscillatory behaviour close to the relaxation frequency of the system, eventually presenting period doubling for increasing K, a situation called "*self-pulsation*"; further increase in the injection strength drives the laser into the so-called "*chaotic*" regime, which precedes

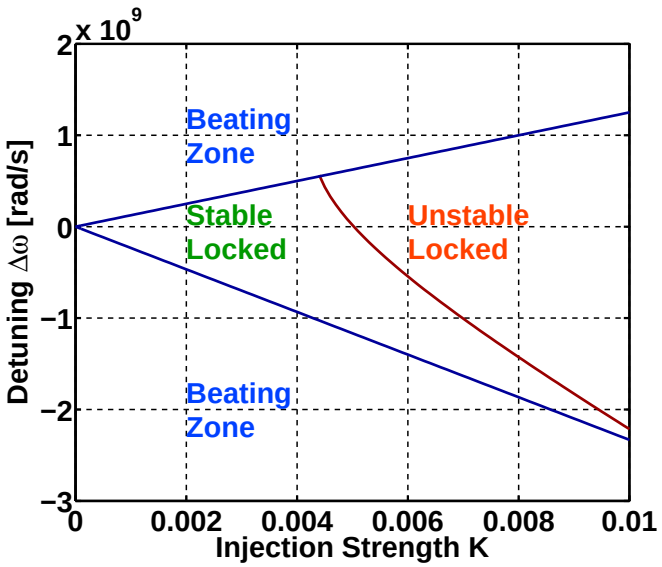

Figure 1.4: Injection locking diagram for a semiconductor laser under weak injection, for a single-mode semiconductor laser at 1.55 µm with linewidth enhancement factor $\alpha = 1.575$ and round-trip time of the cavity $\tau_{in} = 8$ ps.

the "*coherence collapse*" regime, the one dominating the weak to moderate injection locking diagram. In the coherence collapse regime, the phase of the slave laser experiences temporal fluctuations leading to a broadening of the optical spectrum. For strong injection ($K > 0.1$) the system goes through the described regimes in reverse, eventually reverting to a stable locked situation. The final locking zone is the one on the right side of the curve described by the following equation:

$$\Delta\omega = m(K - K_0) \tag{1.8}$$

with

$$m = \tau_{in}\frac{5\sqrt{1+\alpha^2}}{4T_R}\left(1 + \frac{2\sqrt{2}}{5}T_R\omega_R\right) \tag{1.9}$$

$$K_0 = \tau_{in}\frac{\sqrt{1+\alpha^2}}{\alpha}\left(-\frac{25}{8(T_R\omega_R)^2} + \frac{5\sqrt{2}}{2T_R\omega_R} + 2\right) \tag{1.10}$$

This final locking region, which for zero detuning $\Delta\omega$ happens for injection strength $K \geq K_0$, is of interest to obtain stable locking over a wider frequency range. Despite the possibility of attainable stable locking also for weak injection ($K < 0.01$), in that case any fluctuation in the system parameters (e.g. small temperature changes leading to wavelength drifts in the laser emission) causes unlocking between master and slave. Stronger injection and accomplishment of the final locking is of interest to obtain stable locking over a wider $\Delta\omega$ range, making it more robust against system fluctuations.

The analysis presented so far regarded a single-mode semiconductor laser. The dynamics of PMLLs subjected to external injection

have been studied analytically in [59], with the injected signal being a coherent pulse train. The adopted mathematical approach started from the mode-locked solutions of a free-running laser, imposing the injected pulses as perturbations and then finding the steady-state solutions of the injection-locked scheme. The model predicted the possibility of coherent injection locking, with a timing jitter and amplitude noise reduction for the slave pulse train within the locking range. The study mainly focussed on pulsed injection, but also predicted phase locking between a CW input and a PMLL. A more recent model [60] analysed the dynamics of PMLLs subjected to optical feedback from external cavities, and predicted harmonic ML when the length of the external cavity is an integer multiple of the lasing cavity length, with the pulse formation mechanism being the same behind CCML.
As for the experimental findings, both pulsed and CW injection locking of PMLLs were experimentally demonstrated in [61] and [62], respectively. The experimental results reported so far regarding phase synchronisation of PMLLs with external injection will be object of the introduction of Chapter 3.

1.5 HIGH POWER IN PASSIVELY MODE-LOCKED SEMICONDUCTOR LASERS

The discussion of the different ways to obtain mode-locking at harmonics of the fundamental frequency has highlighted how different semiconductor laser geometries can lead to pulses with repetition rates between 40 GHz and 1.4 THz. However, the output power is usually limited to an average power of a few milliwatts per facet, because of a wide number of phenomena taking place, for example gain saturation and excessive bleaching of the SA. This section discusses the reasons that limit the output power of semiconductor PMLL, and describes the approaches that have been developed to overcome this limitation.

1.5.1 *Thermal Effects in Semiconductor Saturable Absorbers*

The laser material traditionally used at the University of Glasgow for the fabrication of devices emitting at 1.55 µm [63] is a commercially available MQW AlGaInAs/InP wafer structure with a gain region containing five 6 nm-thick compressively strained Quantum-Wells (QWs), separated by six 10 nm-thick tensile strained barriers. The QWs are surrounded by 60 nm-thick GRaded INdex Separate Confinement Heterostructure (GRINSCH), and the core layer is embedded between an upper p-type doped InP layer and the n-type doped InP substrate. A diagram representing the epi-structure, dubbed Five Quantum-Well (5QW) material, is presented in Figure 1.5. The ML performance of

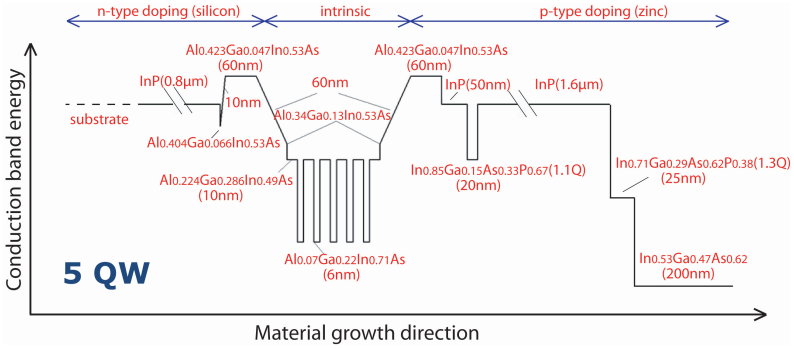

Figure 1.5: Epitaxial structure of the 5QW material.

this material structure has been extensively characterised, and Stolarz et al. have highlighted the limits preventing an optimal ML performance [7]. The analysis also pointed out the detrimental effects that the thermal phenomena taking place in the SA section have on the devices mode-locked operation. The relative bandgap detuning between gain section and SA has been shown to be a key factor in monolithic PMLLs for the stability of the mode-locked operation. Considering the case of absorbing and gain sections sharing the same material platform, there are several phenomena inducing a change in their relative detuning. As previously discussed, in order to achieve stable ML the SA must recover faster than the gain, and this is ensured by applying a reverse voltage to the SA section, thus reducing absorption recovery times to few ps. However, the application of a reverse bias also induces a red shift in the bandgap energy because of the Quantum Confined Stark Effect (QCSE). Moreover, the photocurrent flowing through the absorber induces a temperature increase through Joule heating, and this causes thermal bandgap renormalisation, whose final effect is again a red shift in the bandgap energy of the SA. With regards to the gain region, this also experiences a thermal red shift of its wavelength emission peak for increasing currents. Under the assumption that the heat flow from the gain to the SA section can be neglected [7], the thermal bandgap drift in each section is determined solely by its own Joule heating, and is given by the following formula:

$$\partial_t \omega_g = -\gamma_{th} \left(\omega_g - \omega_g^0 - R_{th} P_{dis} \right) \tag{1.11}$$

where ω_g and ω_g^0 are, respectively, the bandgap for a given current and that for zero current, γ_{th} is the thermal relaxation rate, and R_{th} is the bandgap shift per unit of dissipated power P_{dis}. Equation 1.11 can be applied to both sections of the PMLL, however the power dissipated is proportional to the induced photocurrent in the SA and to the amplifier current in the forward biased section. This means that the bandgap of the gain section when increasing the current can be predicted, while the fact that the photocurrent in the SA depends on the absorption and therefore on the absorber bandgap position prevents

an estimation of the SA bandgap. Due to the different carrier density between the two sections and the subsequent different temperature increase, the thermal bandgap detuning experienced by the amplifier and SA section greatly differs, and this causes the relative position of the SA band-edge of the SA with respect to the gain peak to shift from strong blue detuning to strong red detuning as the current in the amplifying section is increased. As a result, the range of currents and voltages providing stable ML is limited. The numerical analysis carried out in [64], based on a monolithic PMLL with fundamental repetition rate of 40 GHz and a 2 % absorber, derives pulses duration below 1.5 ps only for detuning of a few THz and currents between 2 and 4 times the threshold current density J_{th}. The analysis also highlights how the region of stable ML quickly vanishes for a red bandgap detuning of the SA.
The thermal phenomena causing a red shift in the SA bandgap and the subsequent limited region of parameter space for which stable ML take place could benefit from a blue detuning of the absorbing section; for this reason, the performance of PMLLs with blue-detuned SAs was experimentally characterised in this work, and will be discussed in Chapter 5.

1.5.2 *Optimising the epitaxial structure for mode-locking*

The maximum achievable pulse energy is related to the gain saturation energy E_{sat}, which is given by[65]:

$$E_{sat} = \frac{h\nu A}{\Gamma(G_n)} \tag{1.12}$$

with $h\nu$ being the photon energy, A the optical cross-sectional area, Γ the optical confinement factor and G_n the differential gain. This formula shows that higher gain saturation can be achieved either by maximising the mode size or reducing the mode optical confinement and differential gain. Another important aspect to be considered is the coupling efficiency between the semiconductor laser and the coupling optics, which plays an important role for the maximum extracted output power. With all these different aspects in mind, the Optoelectronics Group at the University of Glasgow has developed an improved MQW material platform optimised for ML operation. In the optimised epitaxial structure the number of QWs was reduced to three, in order to decrease the optical confinement factor and differential gain. Furthermore, a passive layer, dubbed Far-Field Reduction Layer (FRL), has been introduced in the n-type doped lower cladding, bringing beneficial effects both in terms of output power and coupling efficiency. The FRL pulls the mode towards the n-type doped cladding, expanding the modal spot size. The higher cross-sectional area A translates in higher gain saturation energy E_{sat} and reduction of the far field

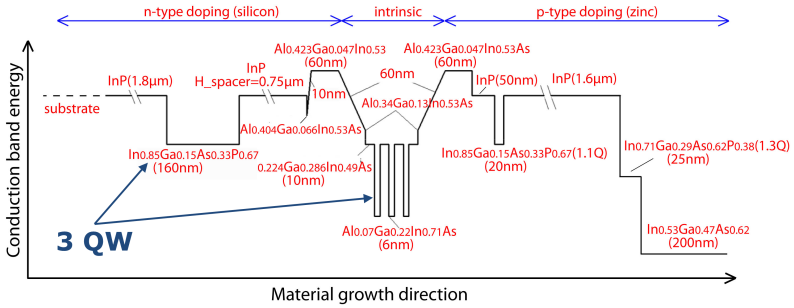

Figure 1.6: 3QW material structure, highlighting the differences with the 5QW case.

beam profile. This could also have been achieved by decreasing the thickness of the GRINSCH layer, although such solution would have increased the modal overlap with the highly lossy p-type doped region, and subsequently the internal losses. On the contrary the presence of the FRL decreases the internal losses, since it pulls the mode towards the n-type doped cladding, which has much smaller absorption coefficient than the p-type doped layer, with $k_p = 22$ cm^{-1} and $k_n = 1$ cm^{-1} the respective values [66].
The optimised layer structure, referred to as Three Quantum-Well (3QW) material, is depicted in Figure 1.6 which also points out the layers differing from the 5QW structure. The ML performance of the optimised epi-design has been compared to that of the original structure in Piotr Stolarz's thesis [6]. The examined mode-locked devices made use of the split-contact ML technique and simply consisted of a FP cavity PMLLs with a single intra-cavity SA. A schematic diagram of the cavity geometry is presented in Figure 1.7. The cavity length

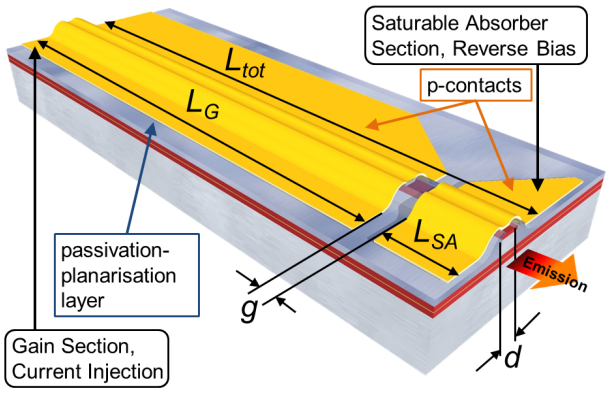

Figure 1.7: Schematic of the cavity geometry used for ML assessment both for the 5QW and 3QW materials.

was defined by chip cleaving and resulted to be 1136 µm and 1256 µm respectively for the 5QW and 3QW case, giving fundamental repetition rates of 38.3 GHz and 35.1 GHz. In the two cases waveguide

widths of 2.5 µm and 2 µm were chosen, which provide a trade-off between single mode-operation and modal losses. The SA was placed next to one of the facets, and electrical isolation from the gain section contact was achieved through a 10 µm wide gap. PML was obtained by forward biasing the gain section and reverse biasing the absorber. Several absorber section lengths were tested for both material platforms. The experimental setup used is shown in Figure 1.8.

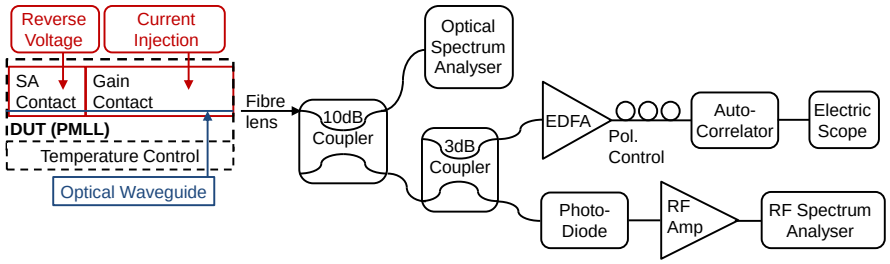

Figure 1.8: Experimental setup used for characterisation of Passively Mode-Locked Lasers (PMLLs). The signal emitted from the Device Under Test (DUT) is distributed to several pieces of equipment to allow simultaneous monitoring of optical spectrum, autocorrelation trace and RF signal.

Devices were kept at a temperature of 20°C throughout the whole experiments. The light emitted from the gain section side was collected using an anti-reflection coated lensed fibre[2]. The setup used allowed monitoring of Intensity Auto-Correlation (IAC), Optical Spectrum Analyser (OSA) and RF Spectrum Analyser traces simultaneously, for a complete ML assessment. The following discussion mainly focusses on the devices output power, and [6] is referred to for a complete analysis of phase noise, pulse width, stability and chirp of the generated optical pulses.

In both 5QW and 3QW lasers, the obtained output average power is strongly dependent on the reverse bias applied to the SA. The 5QW devices were strongly influenced by Self-Pulsation (SP) for low currents, and optimum ML performance was achieved for higher currents and strong SA reverse bias, an unsuitable bias point since the excessive photocurrent induced in the SA normally brings to an early failure of the device. The typical average power emitted by the 5QW lasers is between 2 and 6 mW depending on the SA bias.

The 3QW devices instead show an increasing average power under mode-locked operation for increasing L_{SA}, for all devices tested (SAs lengths between 1 % and 6 %). The longer the absorber, the higher the optical intensity required for saturation, with the ML region shifting towards higher gain pumping, corresponding to higher optical power. The average optical power emitted by the longest SA device was 10 mW, showing a definite improvement with respect to the 5QW

2 *OZ optics* TSMJ-3A-1550-9/125-0.25-7-5-26-2-AR

material. The advantages of the 3QW devices over the 5QW ones become even more obvious if one compares the peak power of the pulses, since 3QW devices provide pulses which are roughly two times shorter.

The presented data confirm that a change in number of QWs from five to three and a reduction of the modal overlap with the top cladding improves the ML performance and increases the emitted power, by increasing the gain saturation level. Furthermore, as showed in [11, 67], the coupling efficiency to a standard single mode fibre is nearly doubled thanks to the low far-field divergence deriving from the modal expansion. In case of a given material with only post-growth processing as an option, a careful adjustment of the cavity design or the introduction of amplifying elements within the cavity can greatly improve performance, as the next paragraph will illustrate.

1.5.3 *Anti Colliding Pulse Mode-Locking*

The analysis of techniques for harmonic ML in semiconductor PMLLs, previously discussed, has shown that one of the disadvantages of the CPML approach is the extreme sensitivity to any mismatch in the position of the SA. The Self Colliding Pulse Mode-Locking (SCPML) technique, where the SA is placed in close proximity to a high-reflectivity facet, has been proposed to tackle the problem, since the pulse nonlinearly interacts with itself inside the absorber thanks to the high amount of feedback [65]. [68] presented a comparison between standard CPML and SCPML, showing how the pulsewidth, chirp, stability and output power performance did not differ between the two configurations. It instead showed that ML performance could be improved by placing the SA next to an anti-reflection coated facet. Despite this being counter-intuitive, the low reflectivity of the facet reduces the interaction between the forward and the back-propagating pulse, yielding a nonuniform intensity profile inside the cavity. The SA undergoes enhanced modulation while the gain region experiences less saturation, in a configuration dubbed Anti Colliding Pulse Mode-Locking (ACPML) [69]. Combining a larger SA modulation with a less-saturated gain enlarges the ML region and produces narrower pulses with increased output power. The CPML, SCPML and ACPML approaches are compared in Figure 1.9, which displays the numerical results as obtained in [69]. The top row of the figure displays the output intensities as a function of the normalised current density, and it can be seen how the ACPML approach is the one with the least fluctuations. The bottom row instead depicts the period of the produced pulse train, which again stays the most stable across the widest range of current densities for the ACPML case. In order to understand the dynamics of the three methods compared, it is useful to base the de-

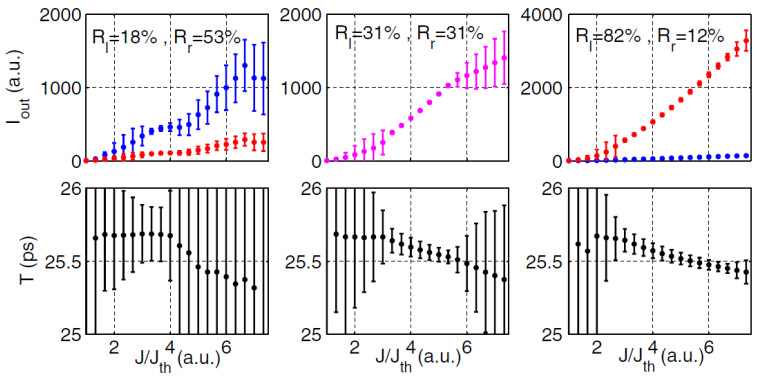

Figure 1.9: Comparison of output intensities (top row) and period of the pulse train (bottom row) as a function of the current density normalised to the threshold value for (from left to right) SCPML,CPML and ACPML. Plot taken from [69].

scription on the electric field. This develops a spatially dependent profile which differs for each configuration and induces an inhomogeneity in the inversion population. The gain is maximised where the total field is smaller, because there is less saturation. The three cases in [69] have been compared keeping the product between the reflectivities of left and right facet constant, so that the devices would have the same threshold. From Figure 1.9 three regimes are evident for all configurations: close to threshold there is a self pulsation regime, followed by a region of stable ML, which persists for increasing current until it eventually disappears or degrades for heavy carrier injection. It clearly appears that the ACPML configuration displays the largest region of stable ML.

An effective implementation of ACPML requires high reflectivity on the gain section side of the device and low reflectivity on the SA side. To achieve low back-reflection from the output cleaved facets, there are two common methods: applying an Anti-Reflection (AR) coating or tilting of the ouput waveguides with respect to the cleaving plane. The first requires depositing a film on the SA facet. Several kinds of AR coatings are available (single-layer, multi-layer, or graded-index), and they normally imply a trade-off between anti-reflection performance and wavelength range [70, 71]. The main disadvantage of AR coatings is the complexity added to the fabrication flow, whereas tilting the output waveguides proves much easier and straightforward, not requiring additional processing steps. Tilting the output waveguides can strongly reduce the backward coupling due to back-reflection, as shown in [72]. The tilt needs to be carefully adjusted for a trade-off between low back-reflection and efficient light collection, and a 10° tilt has been used for devices fabricated at the University of Glasgow. Output coupling can be improved even further by up-tapering the output waveguide. This effectively acts as an integrated spot-size

converter, expanding the mode and reducing the modal mismatch with the lensed fibre. Care has to be taken when designing these structures so that the mode expands adiabatically. The tilting and up-tapering of the output waveguides optimise the modal spot for an efficient coupling with the available lensed fibre, thus improving the alignment tolerance, reducing the back reflected optical power, and proving therefore an ideal candidate for low back-reflection on the SA side. Furthermore, the tapered section of the waveguide expands the optical mode and leads to increased SA saturation energy, shifting the ML region towards higher pumping. However, a higher SA saturation energy worsens pulse shaping performance and leads to an increased pulsewidth, therefore careful design is needed to achieve a good trade-off between high emitted power and optimal temporal pulse shape.
In conclusion, ACPML technique is a promising candidate for improving the performance of CPML semiconductor lasers, as the means to fabricate laser diodes with an asymmetric reflectivity profile would be readily available. Unfortunately the lack of experimental data regarding this configuration prevents its full assessment, especially regarding the output power performance, of interest in this work. Many other approaches to increase the output power in semiconductor lasers have been proposed, with the next paragraph providing a broad overview of the main ones.

1.5.4 *Tapered waveguides*

Many of the methods proposed to increase the output power in semiconductor PMLLs rely on flared waveguides. Widening the waveguides causes the optical mode to expand: the higher cross-sectional area increases gain saturation energy and therefore the maximum achievable energy for the propagating optical pulse. Increased output power under mode-locked operation has been demonstrated for external cavity hybrid ML configurations with monolithically integrated flared gain and SA sections [73]. One issue when using tapered output waveguides can be a multimodal output due to the large width at the facet. A solution to this is to shape the gain region in an inverse bow-tie fashion [74]: in this configuration the optical waveguide is flared towards the centre of the device, but narrow at the optical facets. This allows attaining the high output powers characteristic of tapered structures while maintaining a single-mode optical output. This approach has been shown to increase the achieved output power under mode-locked operation, but so far only for external cavity configurations [75], and not for devices with SA and gain section monolithically integrated on a single chip. For that kind of devices the output power can be increased by combining a narrow ridge SA with a tapered gain region. The flared section has an increased ef-

fective modal cross-sectional area, A/Γ, translating into higher gain saturation energy and pulses with greater peak power. On the other hand, the narrow ridge SA section acts as a mode filter and suppresses the higher order modes. Peak powers as high as 3.6 W have been reported from tapered quantum-dot monolithic PMLLs, with a pulse duration of 3.2 ps [76]. Another approach, which has actually been monolithically implemented, relies on the combination of a Master Oscillator (MO) with a Power Amplifier (PA), in the so-called Master Oscillator Power Amplifier (MOPA) configuration. For these systems, the relatively small output power of the MO is injected into the Semiconductor Optical Amplifier (SOA), where amplification and widening of the optical mode occurs. Typically the flared region is tapered at an angle which matches the divergence of the MO beam. For stable operation in monolithically integrated MOPA systems, the back reflection from the SOA side must be small, so the SOA facet must either be AR coated or have a tilted output waveguide. Given the very small reflectivity of one facet, the opposite one must provide High-Reflectivity (HR), either implementing a DBR grating or through use of an intra-cavity reflector. Mode-locked operation in MOPAs has been reported for the first time by Mar et al. in [77], with 4.1 ps pulses with peak powers in excess of 5 Watts reported for an external cavity configuration including a semiconductor PMLL and SOA. As for monolithic devices, high output power PMLLs based on a DBR laser with an integrated SOA has been reported in [78, 79], achieving 4.3 ps pulses at 40 GHz repetition rate with a peak power of 1.2 Watts. The main disadvantages of the MOPA approach are the added fabrication complexity and the instabilities for high power emission, due to back reflection; if a DBR is used for HR, the cavity length might be an issue as well.

1.5.5 *Broad Area Lasers*

Besides flaring the waveguide in given sections of the device, the simplest approach to increase the gain saturation energy is to have a very broad waveguide through the entire cavity length, as it is for Broad Area Lasers (BALs), based on a laterally wide gain region. This kind of devices can reach output powers of several Watts, but with very poor spatial and temporal coherence because of the nonlinear interaction between the intense optical field and the semiconductor gain medium. Nonlinear phenomena cause emission to be dominated by static and dynamic filamentation [80] and fast pulsations, generally ascribed to an incomplete lateral and longitudinal self-mode locking which are inherent to BALs [81]. Stabilisation and single-mode emission has been demonstrated through weak optical feedback, provided by placing the Semiconductor Laser (SL) in an external cavity configuration [82]. Including a SA within the cavity

optical path has brought the first demonstration of an hybrid mode-locked BAL, emitting 1.6 ps pulses with average power of 1 mW [83]. The stabilisation mechanism is the enhancement of the weak longitudinal self-mode locking through optical feedback. This is also supported by the fact that a single picosecond pulse injected in the BAL cavity has been shown to support longitudinal ML, although only for a few nanoseconds [84]. Eventually the longitudinal ML is reduced due to lateral self-mode locking arising, which makes the emission dominated by a mixture of longitudinal and lateral ML. BALs can sustain stable ML of the lateral modes through optical injection at subharmonic frequencies, as demonstrated in [85]. Despite the very high achievable output powers, the generally poor ML operation when compared to other devices and the complicated dynamics make BALs unlikely candidates for high-power semiconductor PMLLs; the simpler fabrication method they require though makes them good candidates for testing the lasing characteristics of a particular material design.

1.5.6 *Multi Laser Arrays*

Arrayed lasers are based on evanescent coupling between adjacent waveguides. Coherent beam combination of semiconductor lasers at high power levels has been one of the challenges presented by Multi Laser Arrays (MLAs) [86]. Ideally as many lasers as possible should be coherently combined so that the power and the spatial and spectral brightness are scaled with the number of elements in the array. Continuous wave single-mode operation of MLAs has been demonstrated through the Resonant Optical Waveguide (ROW) [87] and the Slab-Coupled Optical Waveguide Laser (SCOWL) [88, 89] techniques, which will not be described here, limiting the analysis to the reported experimental results. The first observation of ML in a monolithic MLA design has been reported in [90], achieving 5 ps pulses at 40 GHz repetition rate in a single QW material structure where the SA had been formed through ion implantation at one of the facets. Mode-locked operation has been reported also for ROW semiconductor laser arrays, both for active and passive configuration, attaining 5.6 ps pulses with peak power of over 3 Watts. No results are reported for ROW devices at 1.55 µm. As explained in [91], the lack of high output power reports in semiconductor PMLLs at this wavelength is due to a shorter upper-state lifetime of the carriers with respect to devices operating at 1.0 µm, due to increased Auger recombination. SCOWL devices allow increased pulse energy because of the generated large optical mode that implies low confinement factor and waveguide losses, and stable pulse train has been reported through PML at 1.55 µm with 10 ps pulses at a repetition rate of 4 GHz [92]. Such a low repetition rate is one of the negative aspects of SCOWL-based mode-locked lasers: they require cm-long cavities because of the very low confine-

ment factor. The shortest optical pulse reported so far in passively mode-locked semiconductor SCOWLs was 5.8 ps wide, with an average power slightly above 50 mW [93]. It is worth mentioning that the material platform adopted in this work is not well suited for SCOWLs, since this kind of devices requires etching through the MQW core layer, exposing it to air. This leads to an increased nonradiative recombination at the exposed sidewall because of etch defects and surface states: QWs passivation techniques must be implemented not to compromise device performance [94], making the fabrication more cumbersome and inefficient.

1.6 SATURABLE ABSORBER BANDGAP DETUNING TECHNIQUES

As previously discussed, the onset of the SA thermal effects leading to the disappearance of stable ML could be shifted to higher gain pumping by applying a blue bandgap detuning to the SA section of a PMLL. This was one of the main achievements of this work and it will be discussed further in Chapter 5. This paragraph will instead focus on the various techniques which could have been used to achieve a blue detuning of the absorber, also motivating why Quantum-Well Intermixing (QWI) was the approach of choice.

The range of available approaches to induce a bandgap shift on the SA is quite broad, thanks to the research interest that the combination of many optical functions on a single optical chip has raised over the years. Photonic integration has been limited by the fact that materials optimised for emission at a given wavelength exhibit losses greater than 20 dB/cm if used for passively propagating the emitted light. Many techniques to overcome this issue have been proposed and developed over the past years, with Table 1.1 showing the most promising so far. Some of these techniques are particularly suitable for applying a bandgap detuning to the SA section of a PMLL, and specifically the Offset Quantum-Wells (OQW), QWI, Selective Area Growth (SAG) and Butt-joint Regrowth (BR) technique. For this reason they will be discussed in more detail in the following sub-paragraphs.

1.6.1 *Offset Quantum Wells*

In the OQW approach [95], the material contains a passive waveguide and a MQW active layer structure grown on top of it. The optical mode propagates in the passive waveguide and is partially overlapping the active layer, which provides the gain. Completely passive regions are defined simply by etching the MQW active region and then regrowing the upper cladding. The advantages of this approach are its simplicity and versatility, leading to high robustness and yield; moreover, the OQW technique is intrinsically polarisation independent. The main

Techniques	POLarisation-based Integration Scheme	Asymmetric Twin Waveguides	Offset Quantum Wells	Quantum Well Intermixing	Selective area Growth	Butt-joint Regrowth	Bonding of III-V on SOI
Pros	Material properties unchanged	Polarisation independent	Polarisation independent	Multiple bandgaps	Multiple bandgaps	Most versatile	No sophisticated growth
	Planar	Versatile, flexible	Robust, high yield	Simplicity, low cost	High yield	Single components optimised	Freedom of design
	Simple growth process	System level design	Simple process	Planar and scalable		Low coupling losses	
				No reflection or refractive index change at interface			
Cons	High losses	High losses	Very long devices	Spatial resolution	Spatial resolution	Highest complexity	Alignment tolerance
	No multiple bandgaps	No multiple bandgaps	No multiple bandgaps	Extra losses	Complexity	Yield	Wafer bonding issues
	Reflections at interface	Non planar	Non planar		Non planar		complexity
		Residual reflection at interface	Poor mode confinement				

Table 1.1: Photonic integration techniques.

downside of this approach is that the QWs do not overlap with the peak of the optical mode due to their offset position, translating into the mode confinement being generally poor and requiring very long active devices. Furthermore, after etching of the QWs and regrowth of the cladding the sample becomes non-planar, which makes the fabrication more cumbersome. It is also worth mentioning that by construction this technique only allows two bandgap values on a single chip, whereas for some applications multiple bandgaps are of interest, for example the combination of active devices, strongly blue-detuned areas for low-loss passive interconnects and partially blue-detuned zones for phase shifters.

1.6.2 *Selective Area Growth*

Between the integration approaches involving an etching step followed by material regrowth, the SAG technique [96] is the only one which has proved capable of providing a number of different bandgaps across a chip in a single growth step. The starting material has a MQW core layer embedded between an upper and lower cladding. The material is etched down until complete removal of the MQW region, then patterned with a dielectric mask prior to the material regrowth step. Growth will take place only in areas where the dielectric is not present, and the thickness and composition of the grown layer will depend on the size of the gaps between the dielectric features. After the first regrowth step, the dielectric mask is removed before the upper cladding is regrown on top. This technique is nonplanar as the OQW one, but it does allow multiple bandgaps on a single chip simply by lithographical definition of different gaps between the dielectric mask features. In fact SAG was the technique which allowed the first demonstration of PMLLs with bandgap detuned absorbers [97], which will be further discussed in Chapter 5.

1.6.3 *Butt-joint Regrowth*

This integration technique is the one offering the highest degree of versatility, at the cost of fabrication complexity. The BR approach [98] is based on the selective removal of the MQW core layer, to be replaced with a material having the desired energy bandgap. Each component to be integrated can have a unique epitaxial structure, therefore the BR allows multiple bandgaps and separate optimisation of the various devices on chip. Once the core layer has been regrown for all desired structures on the sample, an additional regrowth step is required to restore the upper cladding in those regions. This technique is definitely the most versatile and the one providing the best performing integrated devices because it allows single components optimisation. It is worth mentioning, however, that due to the number and complex-

ity of the required growth and fabrication steps it can be affected by yield issues. The BR approach allowed the realisation of a monolithically integrated PMLL with different absorber and gain structure [99], whose ML performance will be discussed in the introductory part of Chapter 5.

1.6.4 *Quantum Well Intermixing*

Quantum-Well Intermixing (QWI), first described in [12], is the technique used in this work for implementing a blue-detuning in the SA section of monolithic PMLLs. The reasons lie in it being a fully post-growth technique, combining effectiveness, simplicity and low-cost. This paragraph explains the QWI intermixing phenomenon, highlighting the mechanisms involved and the technique performance.
QWI is the interdiffusion of atoms between wells and barriers that takes place in a MQW system when it is subject to very high temperatures. From the point of view of the energy band diagram, this corresponds to the wells and barriers not having distinct energy levels any more, translating into an increase in the material bandgap. The final bandgap of a completely intermixed MQW material will be a weighted average between the energy levels and the thicknesses of wells and barriers prior to atomic interdiffusion. The QWI mechanism is illustrated in Figure 1.10.

Normally, the temperature at which spontaneous purely thermal QWI takes place lies in the range between 600 and 800 °C, dependent on the particular MQW material system considered. Thermal QWI is obviously not area-selective, but several techniques have been devised to enhance interdiffusion in certain areas of the chip while suppressing it in others. An effective area-selective QWI process allows the implementation of a great range of applications, such as the integration of active and passive devices, allowing multiple functionalities on a single chip, or the improvement of monolithic lasers performance, for example through non-absorbing mirrors.

As previously stated, the biggest advantages of QWI are its simplicity and low cost, with no epitaxial regrowth or complicated chip processing being required, and only few additional steps needed with respect to the standard fabrication flow. Furthermore, through the Selective Intermixing in Selected Areas (SISA) technique [100–102] multiple energy bandgaps on a single chip can be attained, paving the way for integrated chips with many different functionalities, such as phase-shifters, passive interconnects and lasers, all requiring different bandgaps.

The most common mechanism to make QWI area-selective relies on the introduction of point defects in designated zones of the chip through lithography and lift-off. The material is then capped with a protective layer, meant to protect the material in the areas where a ma-

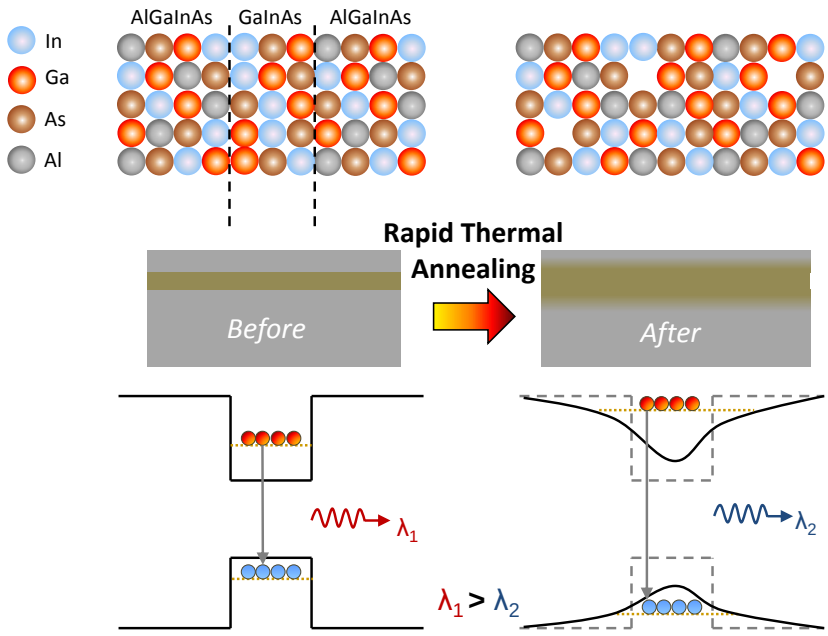

Figure 1.10: QWI mechanism, with the top diagram displaying the position of the atoms with respect to wells and barriers prior to (left) and after (right) RTA. The bottom diagrams show the bandgap of the as grown material (left) and the increased bandgap obtained following the QWI operation (right).

terial bandgap-shift is not required. During a subsequent thermal annealing step, the created defects drive the disordering process only in the designated areas, whereas the material structure stays unaltered elsewhere. In order for QWI to have spatial selectivity, care must be taken in choosing the annealing temperature to avoid interdiffusion of atoms between wells and barriers across the whole sample.

The effectiveness of different QWI techniques is strongly dependent on the material platform and the differences mainly lie in the way point defects are created in the MQW material. One mechanism which proves successful for specific materials might be totally ineffective for others.

One way to create point defects is the introduction of atoms not belonging to the material system to enhance interdiffusion between wells and barriers, as it is the case for Impurity Induced Disordering (IID) [103]. The external atomic species are brought within the material by means of sputtering or ion implantation. Another technique is the Impurity Free Vacancy Disordering (IFVD) which instead relies on the out-diffusion of atoms from the material to a dielectric cap [104]. The IFVD has shown good results for gallium arsenide (GaAs) based MQW material platforms, given the high out-diffusion rate of gallium atoms in dielectric caps (especially silica) provides a high number of point defects to drive the QWI process. The QWI in

use at the University of Glasgow, which will be dubbed "*classic-QWI*" recipe in the rest of this thesis, is based on IID, as copper atoms are included in the system to drive the QWs interdiffusion at low annealing temperature. The *classic-QWI* recipe will be further discussed in Chapter 2.

1.7 CHAPTER SUMMARY AND THESIS CONTENTS

This chapter has outlined the main techniques of interest for generation of narrow optical pulses with ultra-high repetition rate and high peak power, laying the foundations of this thesis work. This first chapter described the background to the research project, laying the foundations of this thesis work. The motivations behind this research work were highlighted, then some important concepts were briefly recalled, starting with a description of the ML mechanism and later focussing on the ML dynamics in monolithic semiconductor lasers. A quick overview of the most well-known techniques for generation of ultra-high repetition rate signals in monolithic devices was next, followed by a theoretical analysis of injection locking phenomena in semiconductor lasers. The discussion then focussed on the causes limiting of the output power in monolithic PMLLs, particularly thermal effects in SA sections of PMLLs, since they were addressed in this work. Also previously proposed methods for increasing the emitted power in semiconductor lasers were described. The final paragraph completed the picture of the scientific background before this work and listed several techniques available to induce a blue-detuning on the bandgap of a SA, with particular attention to the QWI technique since it was used in this work.

The next chapters are organised as follows:

- Chapter 2 will provide an overview of the devices fabrication, carried out at a multidisciplinary facility within the University of Glasgow; particular attention will be given to the QWI technique characterisation and performance.
- Chapter 3 will describe the technique developed to generate ultra-high repetition frequency signals through external injection of continuous wave optical lines, discussing the obtained experimental results.
- Chapter 4 will illustrate the possible approaches for monolithic integration of the external injection locking method discussed in the previous chapter. It will also discuss how two coupled ring cavities can be used to generate signals up to THz frequencies, and present preliminary experimental results.
- Chapter 5 will show how the application of the QWI technique to the SA sections of PMLLs can improve output power perform-

ance, demonstrating it by experimental comparison between standard devices and intermixed ones in terms of ML operation.

- Finally Chapter 6 concludes the thesis, summarising the attained results, re-stating the novelty aspects of this work and suggesting future research developments.

2 DEVICES FABRICATION

The devices characterised in this work were fabricated at the James Watt Nanofabrication Centre (JWNC)[1], one of the most advanced academic cleanroom environments in the United Kingdom, part of the EPSRC National Centres for III-V Technologies[2]. Its cleanroom space offers state-of-the-art facilities such as an ultra-high resolution Electron Beam Lithography (EBL) tool, dry etching equipment, metal evaporators and advanced metrology tools.
The following sections will describe the whole fabrication process, starting from a global overview, and later focussing on the single fabrication flows for the different kinds of devices fabricated in this project. Particular attention will be paid to the QWI technique and its future developments.

2.1 OVERVIEW OF THE PROCESS FLOW

The fabrication of semiconductor lasers at the University of Glasgow has been developed and optimised by several members of the Optoelectronics group over many years, achieving a standardised fabrication process flow. Depending on the QWI technique being applied on the samples, different fabrication steps are required, with additional ones needed for the intermixed case. In this work the non intermixed devices will be referred to as "standard" or "as grown". It will be made clear when intermixing is included in the devices fabrication, specifying the parameters of the process for each case.
A standard QWI technique has been used at the University of Glasgow since many years, and despite proving effective on a variety of material platforms, it still shows some inconsistency issues. One of the objectives of this project has been a re-evaluation of the QWI technique, in order to improve performance and achieve more consistent results. The technique developed has been dubbed "*Post-etch-QWI*", and although needing further optimisation it shows promising preliminary results in comparison with the traditional one, referred to as "*Classic-QWI*". The fabrication flow presents slight but key changes between standard non-intermixed devices and those requiring the QWI technique instead, and further differentiation is present between the *Classic* and *Post-Etch* methods. An overview of the fabrication flow for the various kinds of devices fabricated in this work is presented in Figure 2.1.

1 www.jwnc.gla.ac.uk
2 www.epsrciii-vcentre.com/Home.aspx

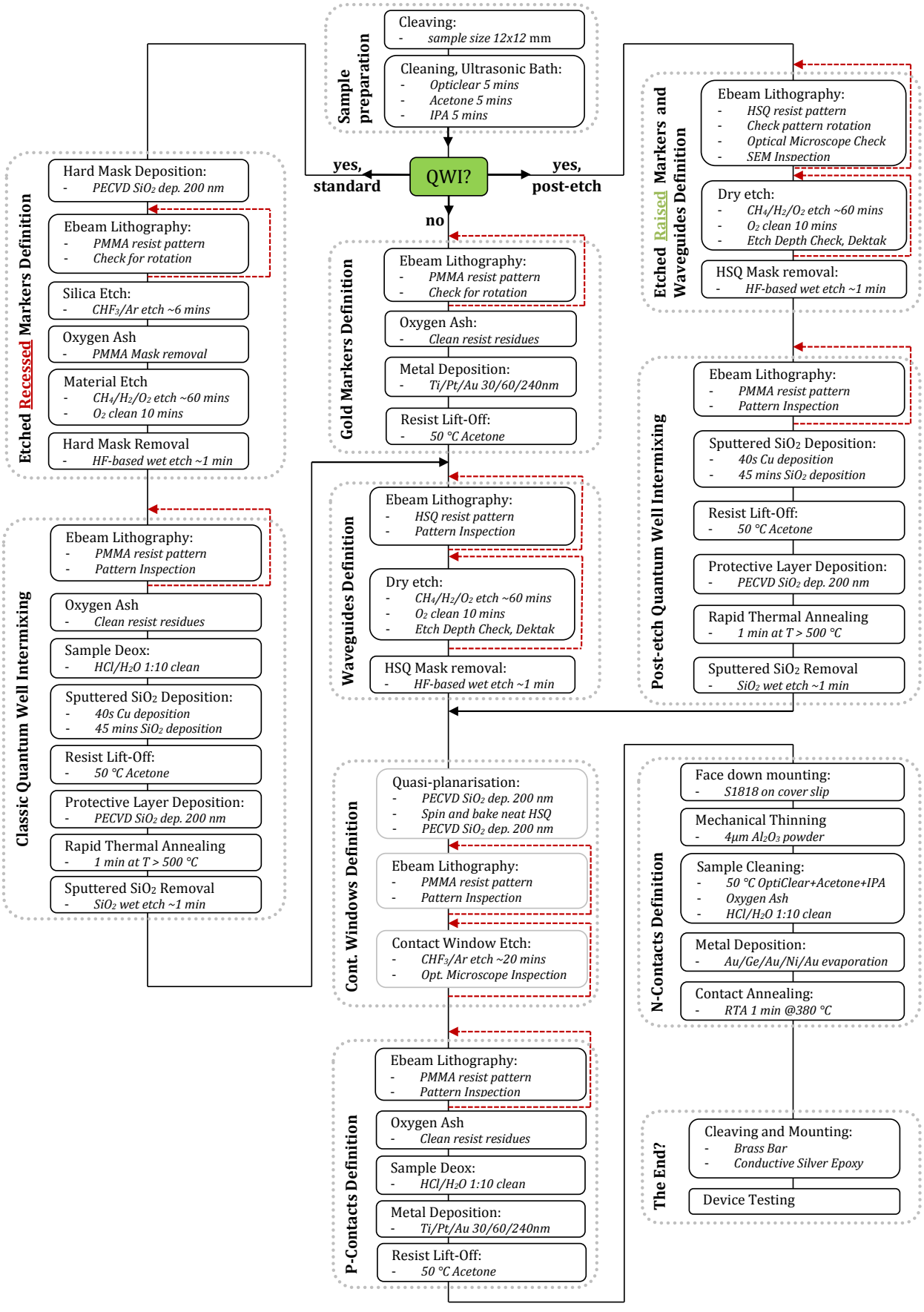

Figure 2.1: Overview of the fabrication flow for the different devices fabricated in the project.

The red dotted arrows highlight critical steps that might have to be repeated, most notably those involving lithography and dry-etch processes. Despite the differences in fabrication flow shown in the diagram for the three kinds of devices, there is a cluster of common fundamental steps which are: the definition of global alignment markers necessary for multiple lithography steps; the implementation of the optical guiding layer; and finally the steps providing the laser with electrical biasing, like passivation, contact area preparation and device metallisation. All these steps form the core of any monolithic semiconductor laser fabrication, and the next section will describe them in more detail. Latter sections will instead focus on the two QWI techniques introduced, highlighting additional steps and differences with respect to the standard process flow.

2.2 STANDARD FABRICATION FLOW

This section will describe the standardised fabrication flow adopted at the University of Glasgow for fabricating non-intermixed semiconductor lasers. Not being an original work of the author, only a quick description will be provided, with a more detailed account to be found in [105–107].

2.2.1 *Electron Beam Lithography*

The very first step of the fabrication process is the design of the lithography mask, which contains all the different patterns to be transferred onto the material through the EBL tool. The layout-editing tool in use at the University of Glasgow is Tanner EDA L-Edit™, which allows design of multi-layer masks in a cell-structured environment, useful to build arrays of devices.

A careful mask design can compensate for some technological limits encountered in fabrication, e.g. in the realisation of directional couplers, suffering from the underetch caused by the etch lag effect [108], as Figure 2.2 illustrates. The etch lag is the phenomenon by which the etch rate becomes dependent on the size of the gaps between the mask features, thus chip areas with high pattern density or very narrow features will have a lower concentration of reactive etchants than open areas, slowing down the etch and making it dependent on the area ratio between mask and open areas. The devices for which this phenomenon is most critical are etched side-walls gratings and evanescent couplers, needing a very precise control of the etch depth for proper operation.

The lithography steps required for fabrication were carried out using a high resolution EBL tool available in the JWNC. Differently from photolithography tools common for the Complementary Metal Oxide Semiconductor (CMOS) industry, which write the whole pattern

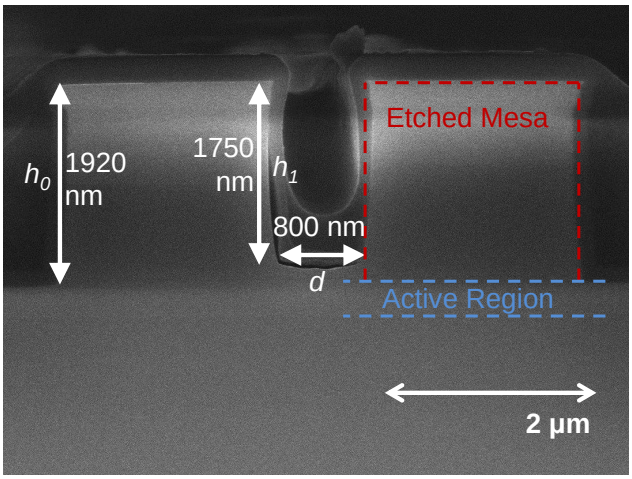

Figure 2.2: SEM image of the cross section of a directional coupler (two waveguides separated by a gap d) obtained by dry etching of an indium-phosphide based MQW material; the achieved etched depth h_1 in narrow gaps d is lower than the one obtained in open areas h_0 because of the RIE lag phenomenon.

on the material during a single exposition, EBL writes shapes sequentially following a user-defined pattern. Because of this it does not have a high throughput and therefore it is not the preferred choice for commercial uses, but it allows high levels of resolution and pattern flexibility, proving ideal for device research and prototyping. The EBL tool at the JWNC is a state of the art Vistec VB6-UHR-EWF 100 keV machine, with minimum spot size of 4 nm and step resolution of 0.5 nm, on a writeable field size of 1.3 mm^2. The electron beam is steered by computer-controlled electro-magnets and focussed on the sample surface, where it exposes an electron sensitive substance (*e-beam resist*) allowing transfer of the pattern onto the chip.
Resist is applied onto the sample by spin-coating, to obtain a uniform layer thickness. Depending on the way the incoming electrons modify the resist molecular structure, one can distinguish between negative and positive "*tone*" resist, with two typical examples being Hydrogen SilsesQuioxane (HSQ) and Poly Methyl Meth-Acrylate (PMMA), respectively.
The difference in the exposure mechanism between the two is depicted in Figure 2.3, with the negative tone case having the energy of the incident electrons cross-linking the atoms of the resist. After exposure (Figure 2.3a), a chemical bath in a specific reactant will remove the resist in unexposed areas and reveal the designed shapes (Figure 2.3c), an operation known as resist *development*, in analogy with photographic techniques. A positive tone resist will instead have its atomic bonds weakened by oncoming electrons, thus exposed areas will dissolve in the developing solution (Figure 2.3b), as is the case for PMMA, a polymer which has increased solubility in Methyl Iso-Butyl Ketone (MIBK) after being hit by highly energetic electrons.

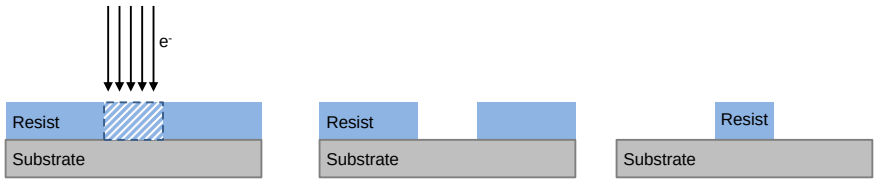

(a) Electron beam exposure.

(b) Post development *positive tone* resist profile.

(c) Post development *negative tone* resist profile.

Figure 2.3: Illustration of the different exposure mechanisms involved for *positive* and *negative* tone resist.

Care needs to be taken to ensure the shapes transferred onto the resist bear an exact correspondence in size and aspect ratio to the designed ones, just as with other lithographic techniques. Because of back-scattering phenomena, some electrons pass through the resist layer more than one time, increasing the exposure; furthermore, areas where pattern is dense will be affected by the neighbouring scattered electrons more than isolated areas. This phenomenon is known as *Proximity effect* and it needs to be properly accounted for, especially for submicron-sized features. Appropriate algorithms for *Proximity Correction* must be implemented, allowing a partial compensation of such effect through modification of the amount of incident electrons (the *dose*) according to the pattern density. Most proximity correction algorithms are based on *fracturing* a given pattern into a number of different shapes with different dose values applied. Starting from a given *base dose*, an appropriate fracturing software will define for every single object in the design a *relative dose*, that is a multiplier applied to the base value depending on the shape size and on its proximity to other features on the pattern. Calculation of the correct relative dose has to take into account how electrons interact with the material, therefore it will differ between distinct substrates. The fracturing of the pattern prior to EBL is normally devolved upon a software tool, with the University of Glasgow relying on GenISys Beamer™. The proximity correction algorithm of GenISys Beamer™ needs the user to input the distribution of the incident electron energies versus the lateral distance from the incidence point at a given depth in the resist layer. The chosen depth will depend on the step following the pattern definition. In the case of a metallisation and lift-off process, it will be the upper edges of the resist layer that will define the deposited area, therefore a proper proximity correction must take into account the electron distribution at the *surface* of the resist. On the contrary, when an etch mask is needed it is the geometry at surface of the substrate that determines the size of the etched features, thus it is backscattering at the *bottom* of the resist layer that must be taken into account

instead. Different post-patterning processes will require different electron distributions, meaning different proximity correction fracturing algorithms in each case. All distributions though will present a similar shape because of the scattering mechanisms pointed out earlier, with the electron energies displaying a narrow peak centred on the incidence point representing the *forward scattered* electrons, i.e. those exposing the resist layer only once. A much broader contribution comes from the *back scattered* electrons, which collide inelastically within the material and bounce back one or many times, causing an increase in resist exposure. The incident electrons energy distribution vs. the radial distance from the incidence point, calculated at the bottom of an HSQ 600 nm thick resist layer on top of an indium phosphide substrate is shown in Figure 2.4. The trace, obtained through Montecarlo simulations, shows how the contribution of the back-scattered electrons becomes negligible more than 30 µm away from the incidence point, which can be considered the back-scattering range for the adopted material platform. This means that pixels further away can be considered unexposed, therefore the fracturing tool will ignore any shape beyond this range when calculating the dose multiplier.
Once the pattern is fractured into different shapes with a different dose assigned to each one, it is ready to be submitted to the EBL tool. The proximity correction and fracturing operation are preliminary for every lithography step and need to be implemented before any actual laboratory processing of the sample. The cleanroom steps involved in the sample preparation for EBL will be discussed in the next section.

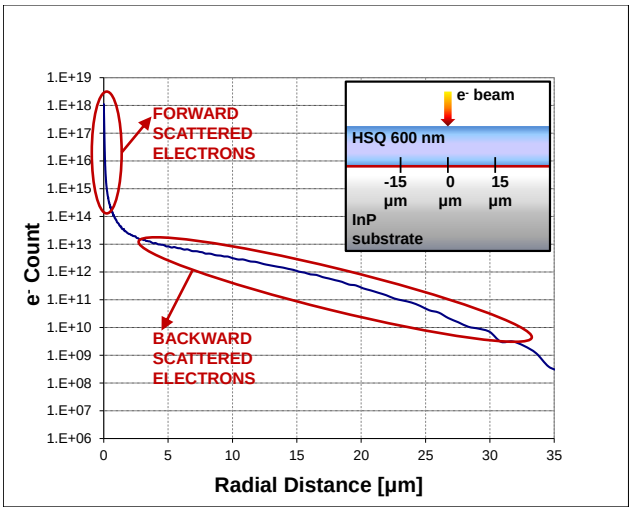

Figure 2.4: Electron distribution vs. radial distance from the beam incidence point. The red line in the inset highlights the interface at which the distribution was simulated, i.e. on the surface of an indium phosphide substrate covered with 600 nm of HSQ resist.

2.2.2 *Preliminary steps*

The material described in Chapter 1 is supplied in 2 inches wafers, while the typical size of samples fabricated at the University of Glasgow is 11x12 mm. All the fabrication processes have been optimised for this sample size because it maximises fabrication yield, providing an optimal trade-off between number of devices on chip and potential material waste arising in case of problems during fabrication. It is desirable to fully exploit the area on the sample, also given that the unit cost per 2-inch wafer amounts to more than £1000. A typical mode-locked laser with a FP cavity geometry occupies an area of 0.12 mm^2 (size 100 µm x 1.2 mm), so a great number of devices with several SAs lengths can be implemented. Starting from the 2 inches wafer, the first fabrication step is dividing it into quarters (Figure 2.5a), and then dividing each quarter in smaller samples by scribing the wafer along its crystallographic axis using a diamond tip; a small pressure applied parallel to the scribe will then be enough for the sample to cleave along that direction. Figure 2.5b shows a typical cleaving pattern, allowing to maximise the area used for chip fabrication but at the same time leaving small pieces of material useful for dose and etch tests.

Once a small 11x12 mm piece is cleaved and ready to be used, the first step taking place in the cleanroom environment is the cleaning of the sample, in order to remove all organic and inorganic contaminants accumulated during previous handling. The sample is immersed in a series of solvents for a fixed time, respectively *Opticlear*™, *Acetone* (CH_3COCH_3) and *Iso-Propyl Alcohol (IPA)* (C_3H_8O); an ultrasonic bath is used to enhance the cleaning action of the solvents, for a more effective removal of dirt residues. After completion of the cleaning cycle, the sample is dried using a nitrogen blow gun. IPA is used for

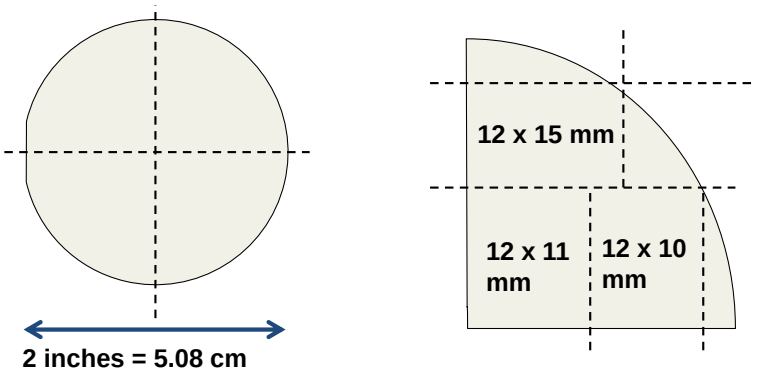

(a) (b)

Figure 2.5: Cleaving pattern for the whole wafer (2.5a) and typical division of a quarter wafer (2.5b) maximising material use.

the final rinse because it does not leave drying streaks on the sample. The following step consists in placing the sample within a chamber filled with oxygen plasma, which acts as a mechanical etch for any contaminants not removed by the solvents bath.
After this standard cleaning process the sample is ready for the first EBL step, that consists of the definition of global alignment markers, necessary for fabrication processes with multiple lithographic steps. The standard markers in use at the University of Glasgow for fabrication of semiconductor lasers are metallic, made either of nickel-chrome (NiCr) or titanium-platinum-gold (TiPtAu). The global alignment process is automatic and it is the operation by which the EBL tool aligns the pattern with the ones previously written. The wafer is loaded manually by the operator and might be rotated up to 0.2 degrees, which translates into an initial 30 µm positioning error over 10 mm. After aligning to the global markers though, the EBL tool is able to locate any point on the sample within 1 µm. Given the importance of markers for a correct alignment between the different layers in the design, firstly they must be large enough in order to be quickly found in spite of the inevitable loading rotation error; secondly well-separated from each other and from other features on the sample to allow unique identification; finally, they must provide enough contrast in terms of electron scattering with respect to the semiconductive substrate. Typically a square-shaped metal marker few hundreds nanometres thick and 40 µm side, at least 100 µm away from any other feature on the sample satisfies all those requirements. It is good practice to check the markers condition prior to each lithography step, because any deviation from their nominal shape might result in the next lithographic patterns being misaligned.
The markers are fabricated using the lift-off technique (Figure 2.6), a method very commonly used in micro and nanofabrication to attain an area-selective metallisation of the sample. This process starts by spin-coating the sample with a double layer of PMMA. The spun layers differ in terms of molecular weight and resist concentration in

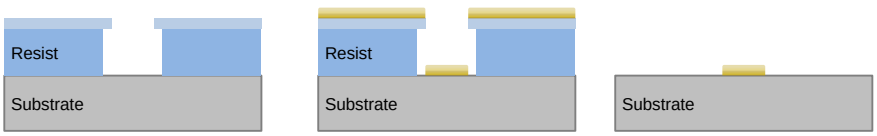

(a) double layer PMMA resist after exposure and development.

(b) metallisation with NiCr or TiPtAu film.

(c) lift off of unwanted metal through resist removal in hot acetone.

Figure 2.6: Illustration of the different steps involved in the lift-off process.

solution, with a less diluted and lower molecular weight one spun first giving a thickness of 1.2 µm; the second layer will have a higher solvent content and molecular weight, attaining 110 nm of thickness. The differences in molecular weight between the two layers translate into different sensitivities to incident electrons, providing the resist with an undercut profile after exposure and development as shown in Figure 2.6a. The following step in the marker definition process is the metallisation of the entire sample (Figure 2.6b). Metal evaporation is a very anisotropical deposition technique (as opposed to sputter-coating), so the shelf-like profile prevents metal coating of the resist side-walls. PMMA can then be used as sacrificial layer and removed through hot acetone bath at 50 °C, leaving the deposited metal only in the patterned areas, as shown in Figure 2.6c.
The cleanroom steps described so far were only preliminary and meant to prepare the sample for subsequent steps, which are the most important in terms of device operation and performance. The first process after defining the markers is the realisation of the optical guiding geometries through lithography and dry etch.

2.2.3 *Waveguides definition*

The definition of the physical structures to generate and guide the optical signals is without a doubt the most crucial process in the fabrication flow. Any imperfection would affect the performance of the final devices, and in a worst case scenario could jeopardise device operation.
Implementing the optical guiding geometries on the material is a two-step process, which starts from defining a lithographic mask on the sample and is followed by the transfer of the pattern onto the underlying substrate through dry-etching techniques, which achieve material removal based on a combination of chemical and physical processes which will be detailed further ahead. Given the highly reactive compounds used for dry-etching the used mask must withstand the process with minimum erosion, and last at least for the required material etch time. One way to classify resists is by their resistance to dry-etch, and PMMA does not perform well in that area, suffering mask erosion badly when exposed to a reactive plasma. A harder material is therefore required to be used as a mask, with good resistance to dry etch. A well established technique relies on Plasma Enhanced Chemical Vapour Deposition (PECVD) of silica to create a hard mask; the pattern would be then transferred onto the hard mask through use of a positive tone resist and subsequent silica etch. One drawback of this double-step method is its enhancement of the mask roughness, directly translating in waveguide side-wall roughness after etching. In order to minimise roughness-related waveguide losses and scattering, an alternative single-step technique relying on HSQ resist has

been used for the devices fabricated in this work. At first HSQ was introduced as passivation layer of interest to integrated electronics circuits, for its compatibility with spin-coating techniques (and for this reason it is also referred to as spin-on-dielectric or spin-on-glass)[109]. Its use as negative EBL resist has also been reported[110], showing several advantages over other negative tone resists, the first being that once developed it becomes chemically equivalent to amorphous silica. It can therefore be used as a dry-etch hard mask, with better resolution and lower roughness because of direct patterning. Its main disadvantage is the limited shelf-life when compared to other EBL resists, especially PMMA which displays excellent stability over time. Since the sensitivity of the HSQ resist to incident electrons will vary with the age of the resist dilution, an EBL test to establish the correct *dose* of electrons (measured in μC/cm) is advisable, especially if very fine features like gratings and narrow gap directional couplers are to be written. The use of HSQ as EBL resist at the University of Glasgow has been extensively investigated by Gábor Mezősi[107], resulting in a reliable and stable process for use in photonic device fabrication. After the markers definition the sample underwent another round of standard cleaning, then it was spin-coated with HSQ resist. Before being loaded in the electron beam machine the sample undergoes a pre-exposure bake on hotplate to cause evaporation of the solvents.
After EBL, the HSQ pattern is developed using Tetra-Methyl-Ammonium Hydroxide (TMAH), which allows effective removal of the resist where it has not been cross-linked by oncoming electrons. The development operation is timed and the TMAH solution is at a constant and controlled temperature; this allows the avoidance of under- or overdevelopment (respectively the presence of unexposed resist residues and the removal of exposed features) and guarantees consistent and repeatable results across different runs of fabrication. The mask written through EBL is accurately inspected after development, with this analysis carried out through use of the sole optical microscope or assisted by a SEM inspection depending on the size of the defined features. Figure 2.7 shows a scanning electron micrograph of a sidewall grating defined onto HSQ resist. When using the SEM to inspect the mask, care should be taken when setting the scanning electron beam energy to avoid overexposure and deformation of the examined shapes. If possible it is preferable to insert a test pattern with replicas of the most critical shapes requiring SEM analysis, and limit the inspection to that area.
Characterisation of the defined pattern is finally complete once mask thickness data are collected by means of surface contact profilometry. This is a measurement technique where a stylus is dragged across a surface typically with a force of 7 mg, allowing to measure the height of the encountered steps without damage to the structures. The vertical resolution is 5 , while the lateral resolution is limited by the tip

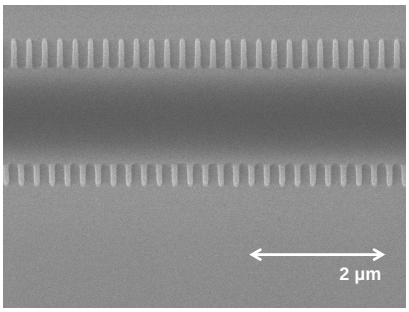

Figure 2.7: SEM image of a grating structure defined in HSQ resist.

size, with a standard value being 12.5 μm. A typical mask height for the HSQ waveguides mask is in the range 500 to 650 nm, with the actual thickness varying depending on the age of the resist dilution.
The combined data from optical microscope, SEM and profilometer allow a complete assessment of the quality of the defined mask; if there is a very good transfer of the designed shapes to the defined pattern and if the resist is thick enough to withstand erosion due to dry-etching, fabrication can move to the subsequent step, which will transfer the defined structures onto the material.
Dry-etch techniques are employed instead of wet etch ones because of their repeatability, strong anisotropy and reduced undercut, allowing the definition of structures as small as 100 nm and below. Reactive Ion Etching (RIE) is one of the techniques belonging to the bigger family of dry-etching techniques. Typically, a RIE machine consists of a pressure controlled chamber containing two parallel electrodes, with the lower one holding the substrate to be etched. The reactive species are injected in the chamber via a gas inlet; the plasma is generated using an RF signal, typically at 13.56 MHz, capacitively coupled to the lower electrode, whilst the upper one is grounded. The reactants are therefore transported to the sample surface, where they are absorbed. The gases involved in the reaction have different roles in the etching process: some ionised gases chemically react on the sample surface, dislodging some atoms from the material through ion bombardment in a very vertical way, delivering a very anisotropic etch profile; other atoms are inert in the etching reaction and their only role is to remove the by-product compounds from the surface, in order to avoid building up of residue that could mask the etching. Different gas flows, chamber pressures, temperatures or RF power will change the characteristics of the etching, making it more or less isotropic.
RIE of indium phosphide (InP) based materials is a mature research field, given such platforms are of interest for optical communications in the third window of optical communications (1550 nm). Several gas combinations have been proved to produce good sidewall verticality, etch rate and mask selectivity, with the most common ones based on *Chlorine* (Cl_2) and *Methane-Hydrogen* (CH_4/H_2) [111–115].

Chlorine-based chemistries require high substrate temperatures (> 150°C) to promote desorption of the non-volatile etch products ($InCl_x$); moreover, their very fast etch rate increases the RIE lag, proving problematic when etching very narrow features.
For these reasons, the standard etching process for the MQW structure used in this work is based on a methane-hydrogen chemistry. This process can take place at room temperature and provides good verticality and negligible side-wall roughness [116]. The etch rate is much slower than chlorine-based etching, just few tens of nm/min, but this is beneficial in terms of RIE lag. The major drawback of this chemistry is the formation of hydrocarbon polymers on inert surfaces, reducing the etch rate, increasing the surface roughness and affecting the etch anisotropy. The build up of residue on the side-walls can be mitigated by introduction of oxygen, which helps polymer removal and improves the verticality of the etch [117, 118]. Furthermore, the addition of oxygen increases the etch selectivity for the considered MQW material platform when removing the upper InP cladding. When the etch reaches the first confinement heterostructure at the very top of the QWs region, the aluminium content in that layer causes it to readily oxidise due to the oxygen-rich atmosphere. A thin layer of Aluminium oxide is thus formed (Alumina, Al_2O_3), bringing the etch rate down to 1 nm/min and therefore increasing the selectivity to a value of 30 : 1. The RIE lag is therefore strongly mitigated, hard to reach features like the bottom of narrow gaps can be etched down to the same depth as open areas thanks to the use of a MQW material platform including an Aluminium-quaternary core layer. The oxidation of this layer allows for a slight over-etch (normally 20% of the time required to rich the oxidising layer) providing a uniform etch depth across the whole sample, independently from the size of single features or inter-feature gaps. One way to guarantee very good repeatability between etch runs is to rely on interferometric techniques, which give real-time information on the layer currently being etched. Once the etch-stop layer is reached, the trace sets on an almost constant level, indicating the material is being etched very slowly. The interferometer has been used for all samples fabricated in this project, and Figure 2.8 shows a typical experimental trace with the signal first displaying growing oscillations and then dropping beyond a given etch time.
After etching the material, the quality of the waveguides in terms of side-wall roughness and verticality is assessed through SEM inspection, while the profilometer is used to check the target etch depth of 1920 nm has been attained. An SEM image of an etched grating structure is shown in Figure 2.9. If the post-etch inspection is satisfactory, the mask can be removed through wet etching in a dilution of water to Hydrofluoric Acid (HF).
After completion of the dry etching step and removal of the HSQ mask,

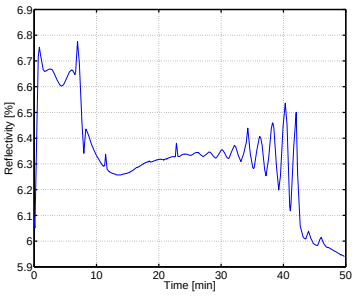

Figure 2.8: Interferometric signal obtained while etching the 5QW material.

the sample is cleaned in acetone and IPA (without the use of an ultrasonic bath to preserve the fragile etched features), in preparation for the following step, the passivation and quasi-planarisation of the fabricated structures.

2.2.4 *Passivation and Contact Area Preparation*

It is vital to provide electrical isolation between the open areas and the surface of the guiding structures for semiconductor lasers to operate properly. Current has to flow between the p-doped and n-doped cladding, with carriers being injected from the top of the waveguides only where active optical guiding geometries are present. Isolation has to be provided also for the most upper layer of the material, e.g. between the gain section and the SA of a PMLL or between an active device and a passive interconnect.
The deposition of several hundreds nanometres of dielectric is a largely diffused electrical isolation technique, with the most common choice in microfabrication falling either on silica or silicon nitride. The latter has a higher static dielectric permittivity value of 7.5, whereas silica has a value of 3.9. Both dielectrics can be deposited through several techniques, such as PECVD and Low Pressure Chemical Vapour Deposition (LPCVD); both deposition methods normally operate at high temperatures ($> 300°C$) but in case of particular substrates intolerant to high temperatures Inductively-Coupled Plasma (ICP) tech-

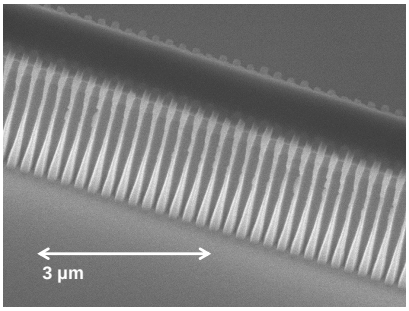

Figure 2.9: SEM image of an etched grating, substrate tilted by 45°.

niques can be used, allowing films deposited at room temperature. For the semiconductor lasers fabricated in this project PECVD silica was used as electrical isolation, being fully-compatible with the quasi-planarisation technique which was adopted to guarantee metal contacts with good uniformity. The necessity for quasi-planarisation will become obvious shortly.

The standard deposition techniques used to metallise contact areas are sputtering or evaporation. The latter is a very vertical deposition and proves problematic in terms of contact pads uniformity across material "steps", i.e. waveguides and trenches, because the vertical side-walls of the structure end up not being coated. On the contrary sputtering deposition is not very directional, especially when the "rocking" technique is applied to make sure the deposited layer is uniform, with this method consisting of multiple deposition runs with different tilts applied to the sample. Despite producing an improved contact pads uniformity across non-planar geometries, it comes at the price of lift-off issues because the resist side-walls are continuously coated as well. It is therefore advisable to make the sample more planar after the waveguide definition in order to allow the use of metal evaporation techniques. The starting morphology of the surface following dry etch is uneven, and if only PECVD silica is used for electric isolation planarity will not improve, being PECVD a very isotropical technique. The passivation layer can be levelled through the quasi-planarisation technique, consisting in the application of a layer of spin-of-dielectric. For this purpose HSQ is used, since as previously stated it can very conveniently be used both as EBL resist and as passivating spin-on-dielectric. For this purpose HSQ resist is spin-coated on the sample following a silica deposition of 200 nm; resist curing is then attained through one hour oven bake at 180°C. The relatively high baking temperature causes the resist layer to cross-link, making it in fact equivalent to a layer of amorphous silica. Because of the large thickness of the spun layer and the oven bake curing, cracks appear on the dielectric surface, thus another layer of PECVD silica with 100 nm thickness is needed to smooth the surface prior to the next step. Figure 2.10 shows the cross section of a completed device where the effectiveness of the quasi-planarisation process can be observed, especially in terms of the deposited metal planarity.

The next fabrication step consists in carrying out a pre-annealing of the sample. The reason for this lies in the fact that deposition of silica in a PECVD reactor is achieved through chemical reduction of silane (SiH_4), and a hydrogen residue is always present in PECVD silicon-containing dielectrics, sometimes as high as 8 %. The hydrogen incorporated in the silica layers can be detrimental because it could reach the passivation film surface during the annealing of the contacts, causing bubbling of the upper metallisation and hindering the whole fabrication process. For this reason the sample underwent

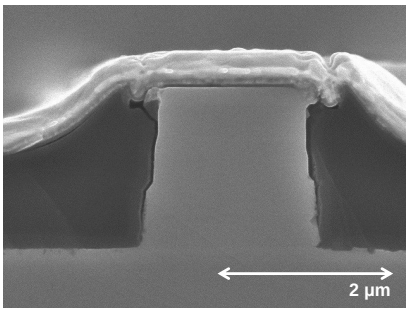

Figure 2.10: SEM image of the cross section of a completed FP laser.

RTA at 380°C for one minute (the same temperature used for annealing of the contacts) before continuing the fabrication.
The selective patterning and etching of the isolation layer where carrier injection (or depletion) occurs came next, and it was carried out through spinning and EBL of a double-layer of PMMA resist on top of the isolation silica. This lithographic step is similar to the definition of global alignment markers, with the only exception of the proximity correction algorithm applied. Whilst for lift-off processes the considered electron energy distribution for proximity correction must be the one at the *surface* of the resist, for contact windows etching it is the distribution at the *bottom* of the resist that needs to be taken into account. Once the PMMA is exposed and developed, dry-etching of the silica isolation layer takes place, by a fluorine based gas mixture (CHF_3/Ar). This etch recipe gives a good etch rate of silica (30 nm/min) and excellent selectivity with respect to the underlying material cap layer, allowing a slight over-etch to ensure the upper surface of the waveguides is cleared of any dielectric residue.
The quality of the silica etch is then assessed through an accurate optical microscope inspection. All dielectric must be removed where needed, or otherwise the electric performance of the lasers will be affected, especially their series resistance. The effectiveness of the etch is checked by inspecting the widest waveguides on the chip, normally the output tapers, where complete etching of the isolation layer ensures a successful etch everywhere given the quasi-planarisation spin-coated HSQ will be thicker on top of wider structures. Once the optical microscope inspection of the sample is judged satisfactory, the PMMA mask can be removed through oxygen plasma ash; the oxygen ions will also mechanically strip the sample surface from any residues, preparing it for the next and final steps.

2.2.5 *Metallisation and Final Steps*

As already pointed out, sputtering deposition lacks in directionality, being based on an ionised gas (typically argon) mechanically dislodging atoms from the metal target, atoms which then fly ballist-

ically onto the sample following random walks.
In a evaporation chamber instead, a high energy electron beam is magnetically focused on a crucible containing the desired metal; the high energy delivered by the incoming electrons produces metal evaporation. The evaporated metal atoms then travel to the sample, following almost vertical patterns thanks to the high vacuum in the chamber (10^{-7} mbar). Once on the sample the metal atoms experience a direct transition from vapour to solid phase. Thanks to the implementation of the quasi-planarisation technique metal evaporation can be used, minimising lift-off related issues. The absence of a quasi-planarised layer would cause a thinner or absent metallisation on the sides of the waveguides, which would prevent current being delivered from the big contact pads to the p-type layer or would fuse for high carrier injection.
One last lithographic step is necessary for definition of the contact pads shapes, prior to metallisation and lift-off. Again a double layer of PMMA is used, and the pattern is written using EBL. After resist exposure and development the sample undergoes a slight oxygen ash to cleanse possible resist residues from the developed areas, but a reduced power and time is used with respect to the previous cleaning process given the fast etch rate of PMMA in oxygen plasmas. Immediately before metal evaporation a de-oxidising chemical bath in diluted hydrochloric acid is used to remove any native oxides and provide a lower device resistance and a better contacts adhesion on the material top layer. The p-contact metallisation consists in a triple layer of titanium (Ti), platinum (Pt) and gold (Au). Titanium is used to promote adhesion of the contact pads to the isolation layers, because thanks to its reactivity it quickly oxidises, adhering well to the underlying silica. The presence of titanium is penalising in terms of conductivity though, therefore a 30 nm layer is deposited as a compromise. The subsequent 60 nm of platinum serve mainly as a diffusion barrier between the surrounding layers. Finally 240 nm of gold are deposited to enhance the sheet conductivity and prevent the contacts oxidation, allowing reliable testing of the devices. Following metal evaporation, definition of the contact pads is completed by lift-off using a hot acetone bath.
The next process is the mechanical thinning of the substrate, to attain a better thermal conductivity for the lasers and an easier device cleaving. The sample is mounted face down on a glass carrier using a layer of photo-resist as adhesive; it is then manually thinned to a thickness of 200 µm, starting from 360 µm. Thinning of the substrate is achieved through abrasion through a mixture of water and 4 µm sized alumina particles.
After the thinning process, the sample is cleaned in hot Opticlear™, hot acetone and hot IPA, to allow removal of all contaminants accumulated during the thinning, which had to be carried out outside

the cleanroom environment. The hot acetone bath also allows release of the chip from the glass mount, dissolving the photoresist. Prior to the final n-contact metallisation the sample is mounted face down on a glass carrier again (to allow metallisation across the entire area), and the bottom surface is de-scummed through oxygen ash and de-oxidised in the hydrochloric acid solution, as for the p-type contacts case. A metal layered structure composed of Au/Ge/Au/Ni/Au (14/14/14/11/240 nm) is deposited, using again the evaporation technique. A final RTA step at 380 °C for one minute is carried out to alloy the different metal layers and to make the gold atoms diffuse in the n-type region, for an enhanced electrical preformance of the lasers.
The very last operation of the fabrication process consists of separating the different devices and mounting them onto a suitable support for characterisation. The sample is therefore cleaved in different bars, and since all devices fabricated in this work are edge-emitting, the cleaving operation must provide a facet with optical quality, to collect the light emitted from the output tapered waveguides using lensed optical fibres; the same technique described earlier to divide the material wafer into small pieces is used.
Finally, each bar is mounted on brass sub-mounts using a double-component conductive epoxy glue. The sub-mount serves as the common ground contact for the lasers, for heat dissipation and mechanical support, and makes the devices ready for testing.
This section illustrated the fabrication flow in its entirety for devices not exploiting the QWI technique. The intermixing method used in this work and its possible developments for future chips will be described in the next section.

2.3 QUANTUM WELL INTERMIXING, "CLASSIC" RECIPE

As previously stated, the material under investigation in this work is an aluminium-quaternary based MQW system. Both the 3QW epitaxial structure and the commercially available 5QW design have been used in this work: the first for fabricating semiconductor PMLLs, given its superior ML performance (as stated in section 1.5.2), and the latter for fabrication of SRLs exploiting the Vernier effect, which will be described in Chapter 3. Devices based on curved geometries cannot be fabricated on the 3QW platform because the reduced optical confinement factor Γ causes an increase in the bending losses.
The *Classic-QWI* technique has been extensively applied to the 5QW material structure by McMaster for implementation of passive interconnects and phase shifters within an integrated platform [106]. McMaster optimised for the 5QW material the technique that had been in use at the University of Glasgow over many years, based on the early work by Marsh and then further developed by Kowalski et al. [119].

As for the 3QW material platform, the *Classic-QWI* process has been exploited in this work to analyse changes in ML operation induced by an absorber bandgap shift in PMLLs.

The classic recipe is based on a number of steps, the first being the definition of global alignment markers just as it happens for the standard fabrication flow case. As shown in Figure 2.1, the classic-QWI recipe requires the use of etched *recessed* markers, being the high temperature annealing step incompatible with metallic ones. Definition of this kind of markers requires a number of processes similar to those implemented for the contact windows in the standard fabrication flow, first of all the deposition of a 200 nm PECVD silica film. The sample is then spin-coated with a double-layer of PMMA, and the markers pattern is transferred onto the resist through EBL. The underlying silica is then etched in unmasked areas using a CHF_3/Ar chemistry, as for the contact windows. Differently from that case, after PMMA removal the patterned silica is kept as hard mask for a subsequent dry etch step, which will remove the material upper cladding and reach down to the first aluminium-containing layer. The chemistry is the same one used for the waveguides definition. Since the etch depth is limited to ∼2 µm because of the etch stop layer and the electron contrast provided by the material step is much lower than the metal-semiconductor case, a 40 µm square geometry would not be identifiable by the EBL tool and would cause the global alignment process to fail. For this reason when recessed markers are needed a square with 10 µm side is used, providing a good trade-off between ease of patterning and contrast for the electron beam. Once the markers geometries are etched onto the material, the silica used as dry-etch hard mask is not needed any more and can be removed with diluted HF. It is worth mentioning that direct EBL writing of HSQ resist could have been an alternative to PECVD silica patterning and etching, however the latter option has been preferred since it allows optimisation of cleanroom resources, and the slightly increased roughness of the markers inner side-walls is not a hindrance to the global alignment operation.

Once the recessed markers have been written and the QWI mask defined, sputtering of the sample takes place, first with deposition of a thin copper film (∼2 nm) to enhance the atoms interdiffusion; this first layer is followed by 45 minutes of silica sputtering deposition (amounting to ∼200 nm). Sputtering has been preferred over PECVD deposition because it makes the process more effective, by increasing the amount of generated point defects. Furthermore, the use of a multi-target sputterer allows the double layer to be deposited in a single run, while keeping the sample always under vacuum. After lift-off of the masking resist, the sample is coated with a protective layer amounting to 200 nm of PECVD silica, since this second film has been found to suppress spontaneous interdiffusion where the sputtered

layer has been lifted off [119]. The subsequent step consisted in the RTA of the sample for one minute at a high temperature, with the chosen set point depending on the required energy bandgap shift. During the high temperature annealing step the sample is capped by a semi-insulating GaAs piece, to prevent phosphorus desorption from the material without introducing atoms not belonging to the MQW system. Previous work by McMaster [106] has shown that the attained bandgap blue shift varies from 30 nm at 650 °C to 110 nm at 675 °C. These values are to be taken as an indication, since this technique does not excel in controlling the amount of obtained QWI, mainly due to the variability in the thickness of the copper layer. After RTA both the sputtered and the PECVD silica are removed through wet etch in diluted HF, and the following fabrication steps are the same as the standard fabrication flow, starting from the waveguides definition.

The classic-QWI process shows a spatial resolution worst than 60 µm, and this is due to the effect of high temperature on implanted impurities. Copper atoms have a very high diffusivity, and while moving down to the quantum well region it also diffuses laterally, limiting the process spatial resolution and imposing a minimum distance between as grown and bandgap-shifted features. Unfortunately the introduction of this metal ion is necessary, being very effective in driving QWI at relatively low annealing temperatures, and given that indium phosphide based materials rapidly degrade for very high temperatures. A very precise control of the amount of sputtered copper would be beneficial, few atomic layers would be enough for an effective disordering of the quantum wells. Decreasing the thickness of the sputtered copper has been actively sought, but for thicknesses of around one nanometre the sputtered layer starts to show non-uniformity, with some areas of the sample left uncoated.

Another detrimental consequence of QWI using the classic recipe is the performance degradation shown by active devices, even when these are far away from intermixed areas. This is due to gain degradation in the material, more precisely the MQW material used in this work starts to deteriorate at relatively low temperatures (650 °C), mainly because of atomic desorption from the upper cladding layer and because of the upper cladding p-dopant (Zinc) diffusing towards the undoped QWs, affecting lasing operation. This is unfortunately a distinctive feature of the considered material platform, since QWI has been reported for other quantum well systems without any noticeable gain degradation on the intermixed devices, even at much higher annealing temperature (generally above 700°C, and up to 850°C for GaAs based systems) [101].

The main issues affecting the classic QWI technique regard thus the spatial resolution and the control of the amount of copper, as well as the gain degradation in the MQW material. The next section will describe the work undertaken to tackle both problems and the attained

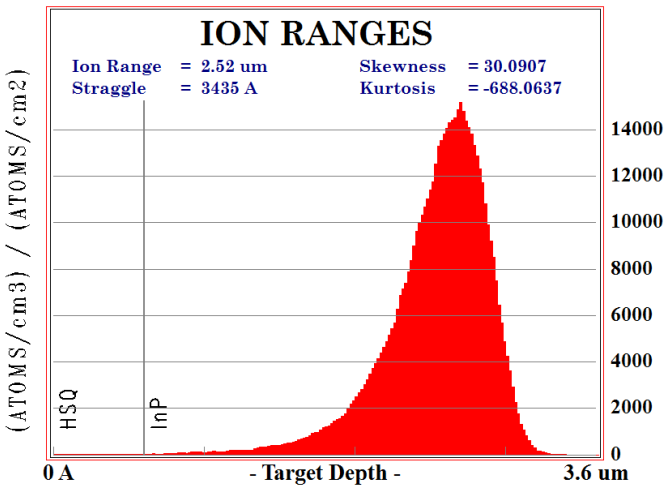

Figure 2.11: Ion ranges distribution for the case of 4.25 MeV Phosphorus ions implantation into an Indium Phosphide substrate with a 600 nm HSQ mask, as shown by SRIM.

results. When developing possible new QWI recipes, care has been taken in order to standardise the proposed processes so that they could guarantee consistent and reliable results over repeated fabrication runs.

2.4 QUANTUM WELL INTERMIXING, POST-ETCH RECIPE

Several ways have been explored to improve the spatial resolution of the standard QWI recipe, and address the collateral gain deterioration. One way to achieve beneficial results on both fronts would be to deliver the QWI-driving impurities in direct proximity of the waveguide core. This approach would have several advantages: first of all, the impurities introduced in the material would not have to diffuse through the upper cladding but a much shorter distance, reducing the intermixing temperature; hence their lateral diffusion would decrease as well, improving the spatial resolution with respect to the classic-QWI technique; moreover, RTA at lower temperatures would be beneficial in preserving the quality of the crystal, and also the gain characteristics would be less altered.

The most obvious way to bring atomic species not belonging to the material system in direct vicinity of the quantum wells would be to rely on ion implantation. The advantage of this approach would be the possibility of implanting virtually any element, independently of its diffusivity in the material under consideration. Simulations were carried out using the SRIM software[3], able to calculate for any atomic species the implantation energy required to reach a given depth in-

3 http://www.srim.org/

side the specified substrate. The ion range distribution obtained by the software for the case of 4.25 MeV Phosphorus implantation into an indium phosphide substrate is displayed in Figure 2.11, with such energy value providing a stopping range of 1.92 µm into the substrate, corresponding to the start of the MQW region. A number of different implanted ions and energies were simulated, with the results always showing at least several MeV necessary to reach the MQW region, thus damaging the crystal and hindering the gain. A partial recovery would be possible through a post-implantation RTA process, which would "heal" the crystal. These potential issues together with the unavailability of an ion implanter within the University of Glasgow, requiring the samples processing to be outsourced (and hence increasing the processing time and costs), resulted in the ion implantation option being discarded.

An alternative way to bring the impurities in close proximity of the quantum wells would be to move the QWI step after the definition of the waveguides. As previously stated, the optically guiding structures are defined by dry etch to a depth of 1920 nm, where the first aluminium-containing layer is encountered, acting as a stop etch layer. Deposition of the atomic species driving the QWI process next to the waveguides could exploit lateral diffusion of the introduced impurities and intermix the quantum wells also in the waveguide core. Figure 2.12 illustrates the difference between the Classic-QWI process and a post-etch QWI one in terms of impurity diffusion dynamics. For a successful exploitation of the lateral diffusion mechanism, the spatial resolution should be small enough to achieve a good selectivity between intermixed and active areas, but also large enough to intermix the core of standard single-mode waveguides. These have a width which is typically 2 or 2.5 µm for the 5QW and 3QW material respectively, thus a QWI post-etch process should have a spatial resolution worst than a few µm. This approach could be unsuitable for devices exploiting interaction of multiple modes, for example to attain passive Multiple Mode Interference (MMI) couplers, or for adiabatic output tapers.

The implementation of the QWI step after defining the waveguides together with the need for non-metallic markers because of the high annealing temperatures could turn to be an advantage, and actually reduce the total number of EBL steps with respect to the classic-QWI recipe. From a global alignment operation point of view, square pillars in the centre of an etched area would be equivalent to recessed markers, as they would provide the same contrast for the incoming electrons. The "raised" markers pattern could be combined with the waveguides one, and they could be written together by EBL, sharing a lithography and dry etch step and ensuring good alignment. This approach could also be used for the fabrication of non-intermixed devices, skipping the first lithography, metallisation and lift-off step;

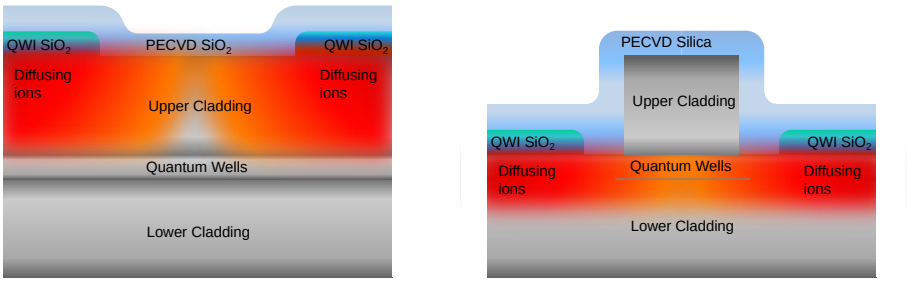

(a) Schematic of the impurity diffusion mechanism for the *Classic*-QWI process.

(b) Schematic of the impurity diffusion mechanism for the *Post-Etch*-QWI process.

Figure 2.12: Comparison between impurity diffusion mechanism during the RTA step for the Classic-QWI case (2.12a) and the post-etch-QWI case (2.12b).

the only downside would be that a repetition of the first EBL step in case of excessive pattern rotation would be more costly in terms of EBL time wasted, especially considering that the waveguide pattern is the one needing the longest EBL time, being written with the highest resolution.

The most straightforward way to intermix the sample after the dry etch step would be a direct transfer of the classic-QWI technique. Unfortunately moving the QWI step after the waveguide definition without any change in the parameters can prove problematic: the initial layer of copper, although only ∼2 nm thick and a necessary presence to create point defects in close proximity of the QWs, would represent a major impairment to the modal propagation being de facto a metal sheet placed next to the waveguide core. The sputtered copper would then need to be removed prior to passivation if the classic recipe is to be applied to etched devices. This issue only arises when application of the classic-QWI recipe is sought for the etched material; normally the presence of a sputtered copper sheet ∼2 µm above the waveguide core does not affect the mode propagation. Furthermore, in order to avoid a high copper content degrading the heavily doped cap-layer, for the classic-QWI recipe the intermixing windows are lithographically defined at a given distance from the waveguides, exploiting the lack of spatial resolution to preserve the material characteristics. This means that the areas where the QWI pattern is defined are removed by the subsequent dry etch together with the upper cladding. In order to allow application of the classic recipe to etched devices, several approaches were tested for removal of the residual copper layer from the areas next to the waveguides core.
Unfortunately the diluted HF, used to remove the HSQ mask and the sputtered silica, does not affect copper and the most common cop-

per wet etchant, nitric acid, also attacks indium phosphide proving unsuitable. A number of chemicals such as hydrochloric acid and potassium hydroxide were tested for copper removal from the top of the aluminium-containing core layer, but they proved either ineffective in removing the sputtered layer or they were attacking the material as well, as comparative Photo-Luminescence (PL) measurements (not shown) before and after copper removal showed.
In order to overcome this limitation a different kind of recipe has been developed, based on embedding the necessary copper impurities within the silica cap used for QWI. This ensures the copper incorporated in the dielectric film is removed by the dielectric etchant when stripping off the deposited silica. Furthermore, it allows bringing the amount of copper down to the lower limit required for intermixing. One of the reasons the classic-QWI process displays imperfect performance is most likely related to the amount of introduced impurities, well in excess of the minimum required quantity for an effective interdiffusion. Sputtering copper and silica in two subsequent steps does not allow bringing the metal layer down to a thickness lower than $\sim$2 nm because of the deposited film becoming non-homogeneous. Inclusion of copper within the silica layer provides a way to overcome this issue. A good control of the amount of copper included in the silica layer translates into a good control over the QWI process.
Several methods to embed copper atoms in silica layers have been reported. One of them relies on the dilution of cupric naphtenate within an HSQ solution [120]. The copper-doped HSQ can then be used as an EBL resist to define the intermixing areas. Another alternative is the impregnation of silicon dioxide with appropriate amounts of copper nitride in aqueous solution [121]. This technique can be applied to a sputtering target, allowing deposition of a copper-doped silica layer. The implementation of such methods requires chemicals not readily available at the JWNC, so preference has been given to a simpler but effective method, that consists in combining the sputtering deposition of silica and copper in a single run, simply through application of a small piece of copper on the sputtering target. The sputtering parameters used are those of the silica deposition alone; given the configuration of the available sputterer, with the target used as cathode at the bottom of the chamber and the sample clamped on the anode at the top, the copper has been simply placed on the silica target without any glue or adhesive. Prior to sputtering deposition, the copper undergoes an acid cleaning step in diluted hydrochloric acid for de-oxidisation, in the same way the contacts area is prepared before metal evaporation. A number of 5QW samples have been prepared by etching them down to the top of the core layer, and several copper pieces of varying dimensions have also been prepared, since the amount of copper required is an unknown variable. The pieces of

5QW material have been sputtered with silica containing different copper percentages, and subsequently cleaved in 2x2 mm squares, each one to undergo RTA at a different temperature. Care has been taken to place the copper always in the centre of the sputtering target, to guarantee plasma disuniformities do not compromise data evaluation. For the same reason, samples have always been mounted in the centre of the holder. The PL signal of each 2 mm square has been measured using the setup in Figure 2.13 prior to the annealing process, to provide reference data on PL intensity and wavelength. The PL setup consists of a continuous wave Nd:YAG laser with a wavelength of 1064 nm. Light from the laser is coupled to a multimode optical fibre through a 20X objective; the fibre is then connected to one of the outputs of a Y-coupler, whose single end is used to deliver the light onto the sample surface. The sample is kept at 77 °K by immersion in liquid nitrogen, to minimise non-radiative recombination and record a clearer PL spectrum. The light from the sample is collected from the second output of the Y-coupler, which inputs to an *Agilent 86146B* OSA for monitoring. The material is designed to emit in the centre of the C-band, at 1550 nm, but the lattice shrinkage due to the low temperature causes the observed PL peak to be ∼1420 nm. This is the typical wavelength observed before the QWI step, independent of the PL measurement taking place before or after the waveguide definition step.

After measuring the PL signal for all samples to be annealed, to account for PL disuniformities due to epitaxial growth and evaluate shifts more precisely, RTA is carried out for one minute at various temperatures, ranging from 550°C to 625°C. After completion of the

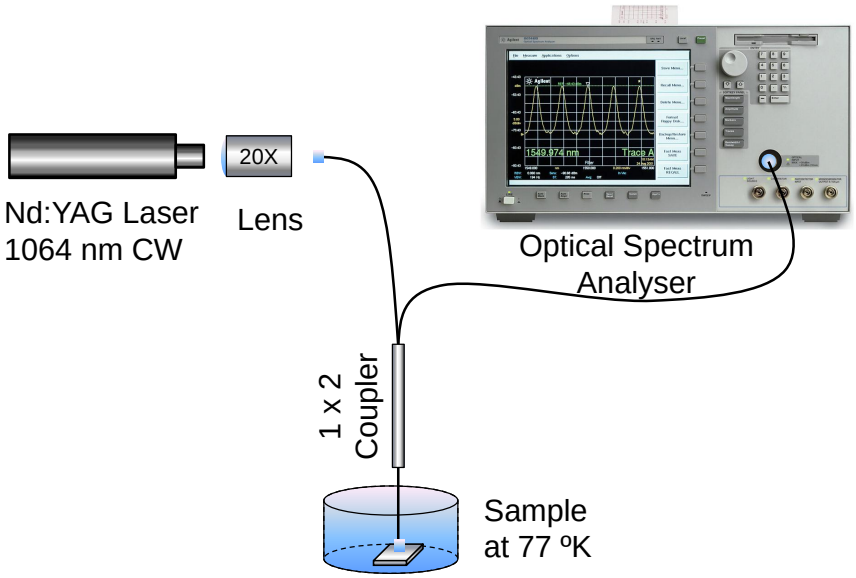

Figure 2.13: Schematic of the experimental setup used to measure the Photo-Luminescence of the MQW samples at criogenic temperature.

annealing step, the PL of every sample is re-measured and compared with the corresponding pre-annealing trace to check if any blue shift in the material bandgap has occurred, or if the PL signal intensity displays a significant drop. The samples under test differ for the amount of copper incorporated within the silica film; the copper pieces of various sizes that have been placed in the centre of the sputtering target occupy a given percentage of the target total area, with values of 0.3 %, 0.15 % and 0.075 %. The results obtained in terms of energy bandgap shift and intensity drop for the PL signal are shown in Figure 2.14.

As Figure 2.14a shows, the maximum obtained bandgap shift spans from 240 nm, obtained for a copper content in the sputtered silica of 0.3 % when annealed for a minute at 625 °C, to a shift of just 10 nm for the same RTA temperature, when no copper is included in the deposited film. Figure 2.14b also shows that the highest bandgap shift attained corresponds to a large drop in intensity for the PL signal. This decrease in intensity is less severe when the copper content in the deposited film is reduced. The dynamics causing the weakening of the PL signal are very complex, and numerous phenomena are thought to contribute, firstly a component of material damage is certainly due to the introduced copper atoms; furthermore, the point defects created in the quantum well region will drive the interdiffusion process but also act as non-radiative recombination centres; finally, the compositional profile of the core layer will change, with the wells becoming more shallow and less able to trap carriers, which then recombine in a non-radiative way. This last phenomenon is not directly related to the introduction in the material system of external atomic species, but it is rather an intrinsic characteristic of intermixed quantum wells. The limited amount of point defects introduced through pure silica sputtering and the spontaneous thermal interdiffusion of atoms between wells and barriers explains the 6 dB drop in PL intensity still observed at 625 °C even without the presence of copper.

A multiple cycles annealing approach has been proposed as a way to recover the damage brought to the crystal during the sputtering and annealing steps, consisting in the samples undergoing many cycles of RTA at lower temperatures after the main one [122]. This allows the introduced impurities to diffuse out of the QWs region, and at the same time it has a "healing" effect on the crystal structure, allowing it to recover the previous damage. One aspect needing careful consideration is the choice of the annealing parameters and their difference between the first and the following RTAs, since the initial one needs to drive interdiffusion of atoms between wells and barriers, while the successive ones need to be carefully chosen and tuned to restore the quality of the crystal while avoiding at the same time any further bandgap shift.

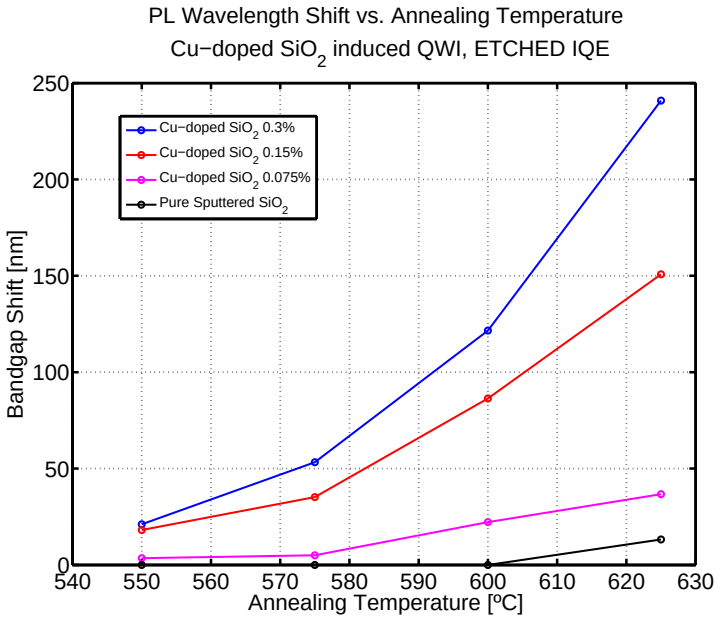

(a)

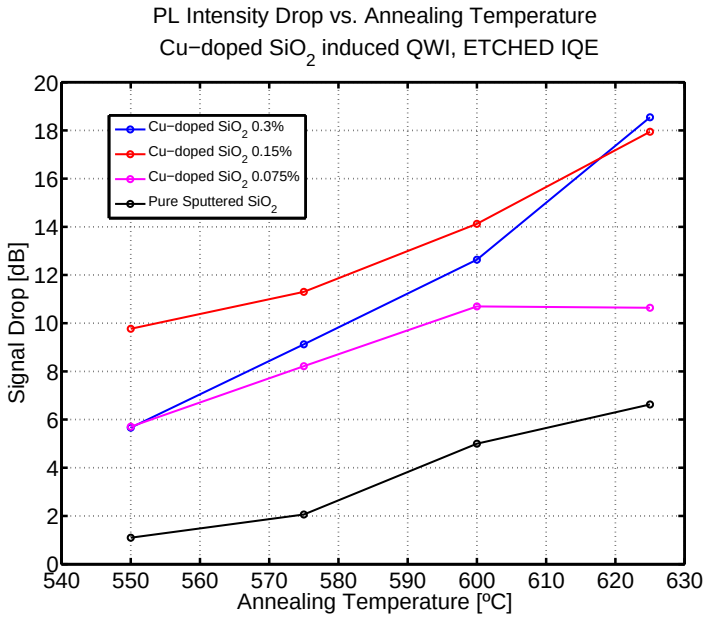

(b)

Figure 2.14: Measured energy bandgap shift (a) and intensity drop (b) for the Photo-Luminescence after sputtering and annealing with several temperatures and copper content.

The multiple cycle annealing approach has been tested on the set of samples whose results have been previously shown: they have undergone another cycle of RTA of one minute duration, at a temperature 50°C lower the the first annealing. PL spectra have been acquired after every successive annealing. Results have showed an average 3 dB recovery in intensity for the PL signal, suggesting this could be a promising improvement to the current technique. However, annealing the samples multiple times has also caused an additional bandgap shift varying between 20 and 50 nm, dependent on the copper content and the temperature of the first annealing. This happens because once the intermixing threshold has been overcome the atoms are more likely to interdiffuse, and additional QWI will take place also for temperatures initially showing no shift. This is an undesirable feature because it adds a variable to the proposed QWI recipe, making it less controllable. Because of the time constraints associated with the project, the multiple cycles annealing approach was not investigated further. Following the encouraging results from the preliminary PL tests after a single RTA step, characterisation of the new technique carried on by assessing the process spatial resolution.

2.4.1 *Post-Etch QWI: spatial resolution and Lift-Off*

The assessment of the spatial resolution posed some hurdles in the fabrication process. These had to be overcome before moving on to the implementation of the final devices. The main difficulty regarded the definition of the QWI areas after the waveguide definition step. For the classic-QWI recipe, sputtering deposition takes place at the start of the fabrication flow, when the sample is planar, therefore a double-layer of PMMA gives enough undercut for an effective lift-off process and a good definition of the QWI pattern, despite the lack of anisotropy of the silica sputtering deposition. With the QWI step taking place after defining the waveguides, the surface of the sample is not planar any more and a double layer of PMMA is not enough to guarantee an effective lift-off of the sputtered film, since the resist amounts to a total thickness of just 1.3 µm in open areas and is thinner next to the waveguides. A lift-off preliminary test was carried out by defining a QWI pattern on a bi-layer of PMMA, followed by copper-doped silica sputtering deposition and hot acetone bath. Figure 2.15a shows the bi-layer test results, where it can be seen how the lift-off process worked only partially, and how the edges of the silica-deposited area present film shards and a rough outline.

The development of a different lift-off technique was therefore needed before moving on to the actual spatial resolution test samples. In an effective lift-off process it is essential to avoid the so-called resist "*flow*", which is the softening of the resist edges occurring when a developed resist pattern is exposed to temperatures greater than its

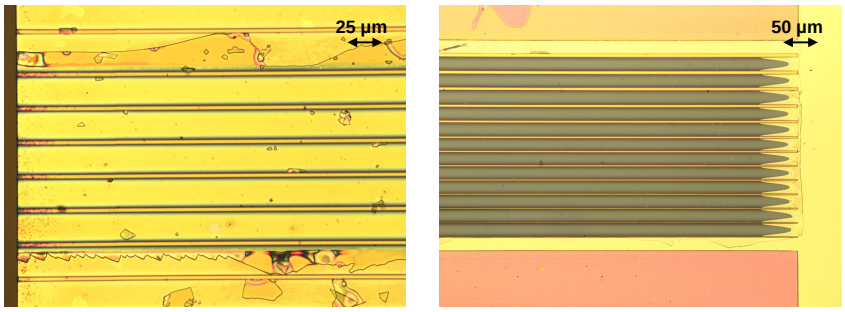

(a) (b)

Figure 2.15: Comparison of the QWI sputtered silica pattern obtained after lift-off for a bi-layer of PMMA used as a mask (left) and for a quadruple layer (right).

glass transition temperature, typically in the range $110 - 130°C$ for PMMA. The rounded edges would not show any undercut and make the lift-off process ineffective. The sputtering deposition might cause resist softening because of the increase in substrate temperature, due to the deposited species source radiation, the condensing heat of the growing film and the kinetic energy of the ions. There are mainly two possible workarounds to resist softening: the first one is to focus on heat transfer and removal dynamics to remove as much heat as possible from the sample while it is being deposited; another possibility is to change the lift-off resist for a more thermally stable one. The two EBL positive resists directly available at the JWNC are PMMA and ZEP™, and none of them has a very good thermal stability [123]. Since the EBL optimisation of a new resist would have required a very long time and its necessity was not ascertained, before embarking in the optimisation of a completely new fabrication process further preliminary tests were run, to understand if the lift-off issues were effectively caused by resist flow or simply by an insufficient PMMA thickness.

All structures fabricated are etched to a thickness of 1.92 µm; the HSQ mask (having a typical thickness of ∼600 nm) used during the waveguide definition step is kept on the sample also during the QWI step to prevent copper atoms from penetrating into the heavily-doped top layer, where they would hinder the electric performance. The difference in height between the protruding features and the etched area is therefore ∼2.5 µm. Given the isotropy of the sputtering mechanism and the fact that the thickness of the deposited sputtered silica is ∼200 nm, a quadruple layer of PMMA was used, consisting of a triple layer with lower molecular weight (having a total thickness of ∼3.7 µm) surmounted by a higher molecular weight film (∼100 nm thick). Several EBL tests were carried out in order to optimise the electron dose and to correct for proximity effects; once found the right set of parameters for a good transfer of the designed pattern, the ef-

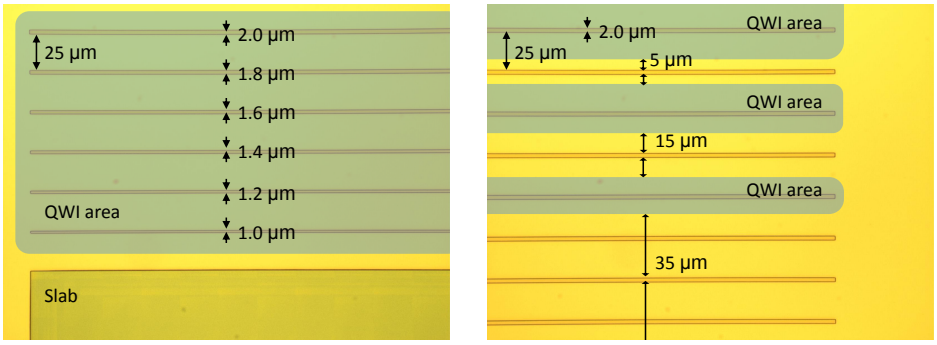

(a) QWI evaluation pattern for *low* spatial resolution values assessment.

(b) QWI evaluation pattern for *high* spatial resolution values assessment.

Figure 2.16: Schematic of the two different patterns designed for determining the spatial resolution of the post-etch QWI process.

fectiveness of the multi-layer resist for the sputtered silica lift-off was assessed. Figure 2.15b shows the lift-off results after sputtering deposition of copper-doped silica for a quadruple PMMA layer, and it can be seen how there are no silica shards or rough edges in the sputtered film, proving the effectiveness of the optimised recipe.
The following step was designing a pattern to assess the new QWI process spatial resolution, which was an unknown variable that could range between few microns and several hundreds in a worst-case scenario. Since the implemented design had to provide useful information over a wide range of possible resolution values, the mask included two types of pattern, one to allow a fine assessment in case the spatial resolution fell below few microns and another for a more coarse assessment. Both designs are shown in Figure 2.16, with the first consisting of an array of waveguides with widths varying from 1 µm to 5 µm, completely covered in copper-doped sputtered silica, as Figure 2.16a shows. In case the created point defects have very limited lateral diffusion, the narrowest waveguide will show a higher degree of intermixing with respect to the widest, with the spatial resolution easily inferred from simple transmission measurements. Adjacent waveguides were spaced by 25 µm to suppress mutual coupling of the propagating modes. The second type of pattern consisted of an array of 25 µm-spaced waveguides whose width was fixed to 2 µm, with the copper-doped sputtered silica deposited next to them at varying distances from 0 µm to 100 µm, as shown in Figure 2.16b. Several bars containing both designs were included into a spatial resolution test sample. Each bar contained at least two repetitions of each design, to guarantee robustness against fabrication issues and provide data regarding process consistency. The sample underwent a first EBL step for markers and waveguides definition followed by dry-etch of the upper cladding in the unmasked areas. Subsequently a quadruple layer of PMMA resist was used to implement the QWI

mask and, after exposure and development, a 200 nm copper-doped sputtered silica film was deposited. The percentage of copper to be included in the sputtered silica film was chosen to be 0.6 % for a number of reasons, the first being a difference in the obtained bandgap shift between small 2x2 mm test pieces for PL tests and the final samples, whose size is typically 11x12 mm, firstly highlighted in [105]. The attained shift changed from 120 nm for the small pieces to only 35 nm for the final samples annealed with the same recipe. The dynamics of this phenomenon are not clear, especially because the temperature during the RTA process is tightly controlled by a closed loop, with the thermocouple being in close proximity with the sample. In fact, the sample is placed on a 6-inches silicon wafer which acts as a carrier, and a K-type thermocouple is right underneath the sample area. One of the hypotheses is that the decrease in bandgap shifts is caused by larger samples having greater thermal mass inhibiting impurity diffusion, even though no scientific evidence was found in support of this theory. Since the PL tests showed that a 0.3 % copper content could provide a great dynamical intermixing range (shift between 0 and 240 nm) across the interval 550 °C-650 °C on small 2 mm pieces, the copper content was increased to 0.6 % with the aim of providing the same QWI performance on a 11x12 mm sample as well.

After the etching, QWI layer sputtering and PECVD deposition of a further 200 nm of silica as protective layer from the high annealing temperature, the sample was cleaved in various bars, each to undergo annealing for one minute at a different temperature, ranging from 600 °C to 650 °C, for a more complete evaluation of the new QWI process.

The cross section of the sample was inspected with the SEM after the annealing step and a change in the facet was observed, as Figure 2.17 shows. A certain degree of roughness appeared, probably due to material desorption arising on the sample edges since all layers are exposed to the high temperature. For this reason the sample was cleaved

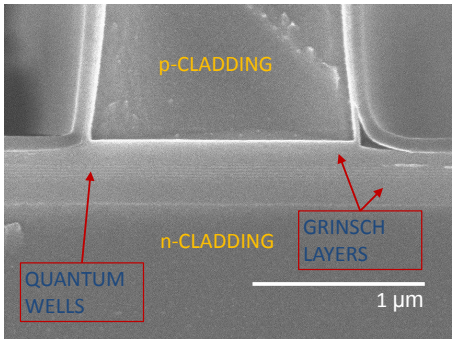

Figure 2.17: SEM image of the material facet after RTA at 600 °C for 1 minute; the different layers present in the epi-structure, made more visible by the material desorption due to the high temperature, are pointed out.

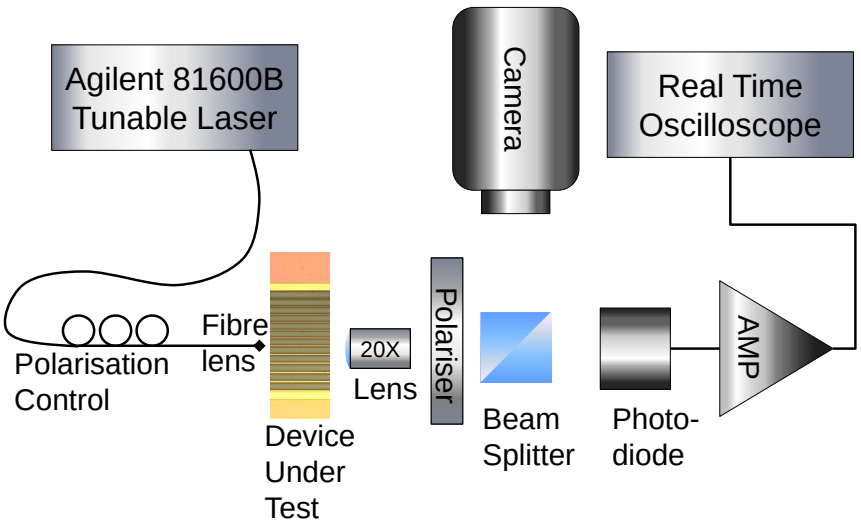

Figure 2.18: Setup for measuring the material bandedge for several passive waveguides.

further on both sides to preserve the quality of the facets and avoid additional losses. The finished bars had a length of 1.3 mm and were tested using the setup in Figure 2.18.

The setup consisted of a laser (*Agilent 81600B*) whose emission is tunable between 1510 and 1640 nm. The light from the source is coupled to the sample through a polarisation maintaining tapered lensed fibre. The polarisation of the output from the fibre tip is controlled to maximise coupling to the waveguides Transverse Electric (TE) mode. Polarisation control is important since both the 3QW and 5QW material have compressively strained QWs, causing a smaller energy bandgap of the TE mode and therefore a higher gain experienced by the TE-polarised light. After propagation through the waveguides, at the opposite facet light is collected through a 20X magnification objective lens, then a polariser is used to minimise any residual Transverse Magnetic (TM) component, and finally the signal is divided into two perpendicular paths by means of a beam splitter cube. On the normal path the mode is monitored for alignment purposes through an infrared camera, whereas the direct path light is collected by a photodiode whose output is monitored on a real time oscilloscope following signal amplification through a transimpedance stage. By synchronising the laser wavelength sweep with the oscilloscope acquisition the obtained trace will be representative of the material bandedge. The normalised trace from the as grown 3QW material is shown in Figure 2.19a. In order to assess the obtained bandgap shift between different waveguides, the bandedge was calculated from the measured trace, as the wavelength value for which the normalised trace attains a 3 dB value. The modulation appearing for non-absorbed photon energies is a filtering effect due to the

sample acting as a FP cavity, with the oscillation period coincident with the cavity FSR. In order to allow a clearer assessment of the bandedge, the experimental data is low-pass filtered in post-processing to remove the fringes, as shown in Figure 2.19b.

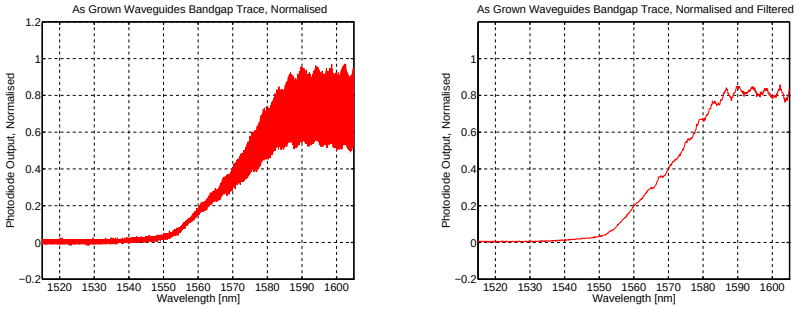

(a) (b)

Figure 2.19: Typical wavelength scan results obtained from the as grown 3QW material, comparison between normalised data before low-pass filtering (left) and after (right).

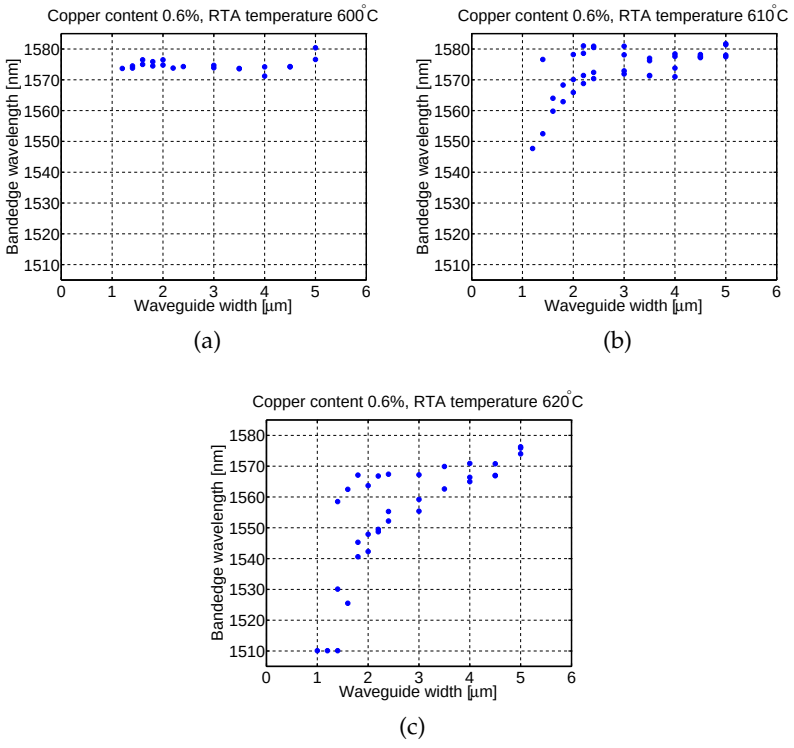

(a) (b)

(c)

Figure 2.20: Energy bandgap measurements for waveguides of increasing width subject to the post-etch QWI technique, annealed for one minute at different temperatures, respectively at 600°C (Figure 2.20a), 610°C (Figure 2.20b) and 620°C (Figure 2.20c).

The bandedge was measured for a number of designs, for the case of completely intermixed waveguides of varying width and also for

2 µm waveguides with increasing distance from open intermixed areas. Figure 2.20 shows the obtained results for the first case, for three bars annealed at 600°C, 610°C and 620°C. It can be seen that a temperature of 600°C did not cause any shift in the QWs bandgap, while there is a gradual increase in the amount of intermixing attained for higher temperatures, especially for narrow waveguides. For all the temperatures shown the widest waveguides measured, having a width of 5 µm, showed little or no QWI, suggesting a very limited lateral diffusion in the material. This is unsuitable for creating passive interconnects, especially in the output sections of the devices which are normally 10 µm wide, since it can be seen that waveguides larger than three microns do not show any change in the material bandedge. In addition, the results show a set of waveguides displaying little or no QWI also after annealing at 610°C and 620°C; the lack of bandgap shift in these sets of waveguides suggests problems with the spatial uniformity of the new process, since the spatial resolution check mask was designed so that repetitions of the same pattern would be equally distributed across the surface of the sample. The strongest hypotheses to explain the spatial uniformity issues are either a variation in the copper content across the sample within the sputtered silica layer, or this layer having a bad adhesion to the material surface. One of the issues with the post-etch-QWI technique could then be the spatial inconsistency in the obtained bandgap shift. Furthermore, post-etch-QWI showed poor performance in terms of propagation losses, with the signal from intermixed waveguides on average 6 dB weaker above bandedge than for the as grown material. The reasons for this gain degradation are not clear, since the post-etch technique and the lower annealing temperature should have provided a lesser deterioration of the gain. It is possible though that the thickness of the protective layer during the annealing step is insufficient, and that the absence of the p-cladding in the post-etch QWI case makes the QWs more vulnerable to the high annealing temperature. All these characteristics make the proposed technique unsuitable for the implementation of an active-passive integration platform, with long intermixed optical paths being too penalising in terms of loss for the mode propagation.

However, as it will be described in Chapter 5, a limited energy bandgap shift could prove beneficial for semiconductor PMLLs performance. The limited lateral diffusion shown would ensure QWI of the SA region without side effects on the gain section, separated from the SA by a 10 µm gap. The waveguides having a width of 2 µm and 2.5 µm show a bandedge shift of ∼10 nm after one minute annealing at 610°C, proving ideal for the sought purposes. Furthermore, the fact that in an intermixed absorber the energy levels are shallower and that the QW is "less-defined" (see Figure 1.10) is likely to affect the lifetime of the photogenerated carriers in the SA. The mechanisms

that contribute to the photogenerated carriers lifetime for a QW in an electric field are tunnelling, thermionic emission and recombination [124]. The recombination rate is usually negligible compared to the other two phenomena, while the thermionic carrier escape rate should greatly increase in shallower and "less-defined" QWs, leading to a reduced SA recovery time. Measurements of intermixed absorbers recovery times have not been reported in the literature so far, but the previous considerations are supported by photocurrent measurements carried out on intermixed electro-absorption modulators [125]. The increased escape rate of the photo-generated carriers also leads to increased saturation intensity, as shown in [126].
In conclusion, the post-etch QWI technique has shown promising results in terms of spatial resolution and accurate control of the attainable shift, but it requires further development and investigation especially regarding the gain degradation dynamics and the spatial uniformity of the process. To test the post-etch QWI technique further, lasers with small intermixed sections were fabricated; the obtained results will be discussed in Chapter 5.

2.5 CONCLUSIONS

The main focus of this chapter were the fabrication techniques employed for the devices used in this project. The chapter opened with an overview of the standard fabrication process, in use at the University of Glasgow since many years for the realisation of monolithic lasers on III-V material. The discussion then proceeded to the QWI technique. The standard QWI process was explained, together with its limitations and inconsistencies, and the work carried out towards the introduction of a new technique, labelled post-etch QWI, was described. Particular attention was given to the fabrication challenges posed by the new process, and to the way they were overcome.
Following the description of the fabrication aspects, some preliminary experimental results for the post-etch QWI were presented. These showed that the new technique could not only match the bandgap shifts obtained with the classic-QWI method, but do it with annealing temperatures 50° C lower. The spatial resolution of the new technique was found to be only few µm, against few tens of µm normally obtained with the classic-QWI technique. Despite some aspects needing further investigation, such as the gain degradation dynamics and the spatial uniformity, the post-etch QWI technique looks promising as a replacement for the standard one. This chapter concluded the introductory part of the thesis, complementing Chapter 1 by discussing the fabrication of the devices and the preliminary experiments carried out to assess the newly introduced technique. The following

chapters will instead focus on the experimental work carried out on the finished devices.

Part II

THESIS RESULTS

This part of the thesis describes the experimental work carried out towards the generation of ultra-high frequency optical signals through external injection and towards the improvement of mode-locking performance in semiconductor lasers using the Quantum Well Intermixing technique.

3

ULTRA-HIGH REPETITION RATE OPTICAL SIGNALS

As already pointed out in Chapter 1, effective generation of ultra-high repetition rate optical signals from monolithic sources is being actively sought for a number of applications. This chapter will describe a method which has proved successful in generating optical signals with frequencies up to several hundreds of GHz, based on a master-slave interaction between two external continuous wave signals and a passively mode-locked FP cavity. The strengths and weaknesses of the proposed method will be shown, stressing the possible developments especially regarding viable monolithic integration schemes.

3.1 OPTICAL INJECTION IN MONOLITHIC SEMICONDUCTOR LASERS

The effects of light injection in laser cavities have attracted interest since the very early days of laser research, when Stover and Steier showed phase locking by direct injection from one "*master*" He-Ne laser into another identical "*slave*" one [56], which was shown to lock its emission to the wavelength of the master. As for semiconductor lasers, they are very easily perturbed from external optical signals. This is particularly true for edge-emitting devices, with their low facet reflectivity and short cavity resulting in an increased sensitivity to optical feedback and external signals. The discussion in Chapter 1 highlighted how the perturbation of a free-running semiconductor laser through optical injection might result in locked or unstable regimes, with the produced outcome depending on the strength of the injected signals K and on their detuning $\Delta\omega$ with respect to the semiconductor laser modes. In between the regions of parameter space K-$\Delta\omega$ where there is no phase locking taking place between the master and the slave laser, one that has been extensively studied is the so-called "*chaos*" region. This is because the chaotic regime can be exploited for applications in cryptography and secure communication systems, since the chaos of two lasers can be synchronised [127, 128]. The region of interest for this project though is when the master oscillator is used to synchronise the emission from a free-running slave laser without inducing chaos, i.e. stable injection locking. Its possible applications and the experimental results reported in the literature will be further detailed in the next paragraph, with particular attention to passively mode-locked semiconductor lasers.

3.1.1 *Injection Locking*

In the field of semiconductor lasers, phase locking through external optical injection is of interest for optical fibre communication systems, especially those based on coherent transmission formats. This is because injection locking can be effectively used to ensure single-mode operation of modulated sources [129], to reduce fluctuations in the lasing modes [130] or for synchronisation at the receiver side in coherent transmission systems [131]. Furthermore, injection locking from a highly stable master laser into a semiconductor laser can be used to stabilise laser operation with respect to the free-running case, producing a narrower spectral line and avoiding wavelength drifts [132].
For the particular case of semiconductor PMLLs, one of their well known flaws is the poor timing jitter affecting the pulse train; the comparison in [133] showed absolute timing jitter below 1 ps for external cavity mode-locked lasers, whereas the value for monolithic PMLLs was 12.2 ps. Another known drawback of free-running PMLLs is the lack of synchronisation to other components in high speed optical systems. This can be a major impairment especially in photonic systems based on coherent transmission formats, where it is important to recover the phase of the optical carrier. This drawback can be overcome by injection locking, which has been successfully employed to demonstrate the effectiveness of semiconductor PMLLs as sources for phase modulated optical communication systems, if an external cavity configuration is employed [134]. Stabilisation of the pulse train has been achieved also by means of optical injection from a pulsed master laser, in the so-called sub-harmonic injection mode-locking [135], where highly stable pulses generated from an external laser are used to stabilise ML operation of semiconductor passively mode-locked devices. The main advantage of this technique is the relaxed requirements for the master laser, since its pulse train can be at a much lower frequency than the slave device; slave stabilisation will occur as long as the repetition rate of the master is a sub-multiple of that of the injected device. This allows the use of an electronically driven actively mode-locked laser as master source, transferring the characteristics of its highly stable pulse train to the slave device.
Another technique proposed for stabilising emission from semiconductor PMLLs does not rely on external active devices but on induced optical feedback through an external mirror, approach which needs the delay introduced by the external cavity to be carefully tuned as it might result both in a reduction or in a drastic increase of the timing jitter [136]. In most reported cases semiconductor PMLLs stabilisation was attained through pulsed injection, either inducing an optical feedback through an external reflector or coupling light from an independent optical source inside the cavity [61, 137]. The effects of injecting a CW signal into a semiconductor PMLL are generally less

reported, with the few exceptions regarding quantum-dot lasers and optical frequency combs generation [138, 139]. In the first case, a CW signal has been used to stabilise the emitted pulses for high pumping levels [138], whereas in the second case optical injection of two coherent CW signals results in increased stability and tuning range [139]. Through amplitude modulation of a narrow linewidth CW optical source and optimisation of the modulator bias, two side-bands with the same phase are produced while the original carrier is suppressed, achieving coherence between the injected signals. The beating of the injected lines modulates the carrier density in the slave device, which allows tuning the repetition rate and reducing the timing jitter of the slave laser. The reported tuning of the repetition rate though was limited to ∼100 MHz. In this work a dual-injection locking mechanism has been employed as well, but instead of being based on two coherent CW signals whose spacing was limited to few hundreds of MHz, two independent widely tunable laser were used as external optical sources. It was observed that under certain conditions the slave devices showed emitted optical signals at a frequency corresponding to the wavelength spacing between the injected lines. The next paragraphs will describe the experiments carried out, with insight and discussion of the attained results.

3.2 ULTRA-HIGH REPETITION RATE GENERATION, EXPERIMENT

The external injection locking experimental setup is shown in Figure 3.1. Several devices were tested, all of them semiconductor PMLLs in a FP configuration coming from a sample fabricated at the JWNC on the 3QW material. The fact that all devices experienced the same fabrication flow ensures more consistent results when comparing their response to external injection. The sample did not undergo the QWI process, and the lasers under test differed only for the SA section length, taking up a different percentage of the total cavity length for each device with values varying from 1.8 % to 11.8 %. The total cavity length is 1240 µm for all devices, corresponding to a FSR of ∼ 36 GHz; isolation between the gain section and the SA contact is provided through a 10 µm gap. Current was injected in the gain section contact while the SA section was reverse biased, in the standard split-contact ML configuration. The maximum reverse voltage applied to the absorber was −4.5 V to minimise the risk of breakdown by excessive current absorption. The temperature of the sub-mount was controlled through a Thermo Electric Cooler (TEC), and kept to 20°C throughout all the experiments. The choice of these particular devices and geometry as subjects for external injection analysis was driven by their behaviour being well understood and extensively characterised [6], which made them ideal candidates for assessing the changes induced by external injection. Two tunable lasers (*Agilent 81600B* and

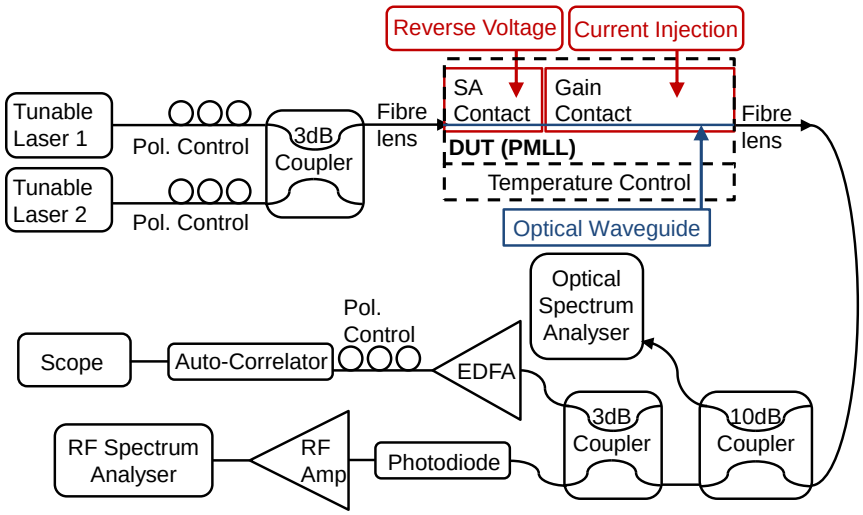

Figure 3.1: Setup for the external injection locking experiments, with injection of the CW lasers on the SA of the PMLL under test (DUT). The optical signal from the gain section side is used to simultaneously monitor the optical spectrum, autocorrelation and RF signal.

Anritsu MG9638A) were used as optical sources to couple CW light into the laser cavity, since both of them provided a narrow linewidth ($<$ 1 MHz) over a wide range of wavelengths (from 1510 nm to 1640 nm) and control of the emitted power, up to 2 mW and 5 mW respectively. The output polarisation from both tunable lasers was controlled in order for the injected light to be co-polarised with the quasi-TE mode, the one experiencing more gain because of the strain in the QWs. The CW lines were combined through a 3 dB polarisation maintaining fused fibre coupler[1], then coupled into the semiconductor laser by means of a tapered lensed fibre[2]. The external CW signals were injected in the monolithic device from the SA side, while light was collected for monitoring and analysis purposes from the gain section side. The same kind of lensed fibre was used for collecting the light from the devices, then a series of fused standard single-mode fibre couplers with different ratios split the collected signal between several pieces of equipment for monitoring. A 10 % fraction of the total power was coupled to an OSA to monitor the changes in the optical spectrum between different operating regimes and align the external injection with the device lasing modes. The remaining 90 % of the total power was equally distributed by a second fused fibre coupler between an auto-correlator (*Femtochrome FR-103XL*), used to assess if emission of a stable train of pulses was present, and a fast photodiode (*New Focus 1014, 45 GHz InGaAs photodetector*) whose out-

1 *OZ optics FUSED-22-1550-8/125-50/50-3A3A3A3S-1-1-PM*
2 *OZ optics TSMJ-3A-1550-9/125-0.25-7-5-26-2-AR*

put was monitored through an RF Spectrum Analyser (*Rohde&Schwarz FSV Signal and Spectrum Analyzer*). The bandwidth of the latter is limited to 40 GHz, therefore the RF signal was used for optimising ML of the free-standing device but unfortunately it could not be used to detect higher harmonics of the fundamental frequency.

The dynamics of the experiment unfolded as follows: first, the external light coupled into the device was co-polarised with the quasi-TE mode. This was achieved through monitoring of the CW line on the OSA after propagation through the sample, with the semiconductor laser left unpumped and acting as a highly lossy passive waveguide. The quasi-TE mode experiences more propagation losses than the quasi-TM, so minimisation of the signal level on the OSA through adjustment of the polarisation controls ensured the CW light coupled into the FP cavity was polarised along the quasi-TE direction. The subsequent step was optimising the free-running operation of the slave device, adjusting the current injection into the gain region and the reverse bias applied to the SA section for optimum ML operation, maximising the quality and stability of the pulse train produced. Figure 3.2 illustrates the ML performance of a semiconductor PMLL fabricated on the 3QW material platform, with both the IAC trace (3.2a) and the optical spectrum (3.2b). The traces displayed were obtained for a device whose absorber is 4.6 % of the total cavity length, reverse biased at -4 V, and for a current of 120 mA in the gain section, used since this set of parameters was shown to give the best ML performance for the considered material platform [6].

The external injection came next, first by coupling just one CW signal into the FP cavity. The wavelength of the external CW line was tuned until it was aligned with the lasing mode corresponding to the peak of the optical spectrum. The following dynamics were observed with injection of a single CW signal: for very low injection (injection strength $K < 0.01$, refer to Chapter 1 for the definition) the ML be-

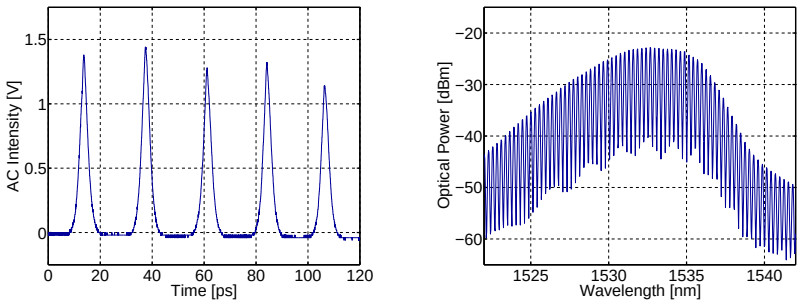

(a) Autocorrelation trace (b) Optical Spectrum

Figure 3.2: IAC trace and optical spectrum for a 3QW semiconductor PMLL whose SA is 4.6 % (57 µm) of the total cavity length (1240 µm) biased at -4.6 V, with a current of 120 mA in the gain section.

haviour of the laser did not display any measurable changes; for the weak to moderate injection regime ($0.01 < K < 0.1$) the optical spectrum became narrower indicating stabilisation and jitter reduction in the produced pulsed train; increasing the power further did not produce any further changes until a point where the ML laser collapsed into single mode emission at the same wavelength as the external source, with pulses disappearing from the IAC trace. This behaviour for a single injected light agrees with expectations and with what was previously reported [140].

A different behaviour was observed when both CW lines were combined in the FP cavity. When the injected signals mutual spacing was an integer multiple of the fundamental FSR of the ML device, and their wavelengths were aligned with two lasing modes, optical signals at a frequency corresponding to their mutual spacing were generated. Efficient discrete tuning of the repetition rate was then observed by wavelength tuning one of the two injected signals, up to several hundreds of GHz. Unless otherwise stated, in all the experiments carried out the wavelength of one of the external CW lines was chosen in order to couple with the maximum of the optical spectrum, while the second wavelength was tuned accordingly with the desired repetition rate, blue shifted with respect to the fixed one. This can be clearly seen from the OSA traces shown in Figure 3.3 and Figure 3.4, while the IAC traces display the optical signals generated at various harmonics of the fundamental mode spacing. By analysing the case without external injection in Figure 3.3 and comparing it with the pulses shown in Figure 3.2 it can be seen that the widths of the IAC pulses are different, respectively $\sim$4 ps and $\sim$6 ps for the two cases. If one applies the ML theory (equations 1.1-1.3) presented in Chapter 1 this suggests a lower number of modes participating to the ML operation for the case with wider pulses. From the OSA traces presented in Figure 3.3 and Figure 3.4 a decrease in the number of modes lasing for the injection locked cases can be observed, while the pulses displayed by the IAC trace become narrower. This at first seems to contradict the theory presented in Chapter 1; however, the presence of the external electric fields, their nonlinear interaction and their beating on the SA section adds a term oscillating at their difference frequency to the sum of the modes, which dominates under stable locking conditions, suppressing ML at the fundamental frequency. In order to gain a better understanding of the dynamics behind the presented injection locking phenomenon, the effects of changing various device parameters have been experimentally assessed, for example by moving the injection towards shorter or longer wavelengths; the results of such characterisation will be discussed in the next section.

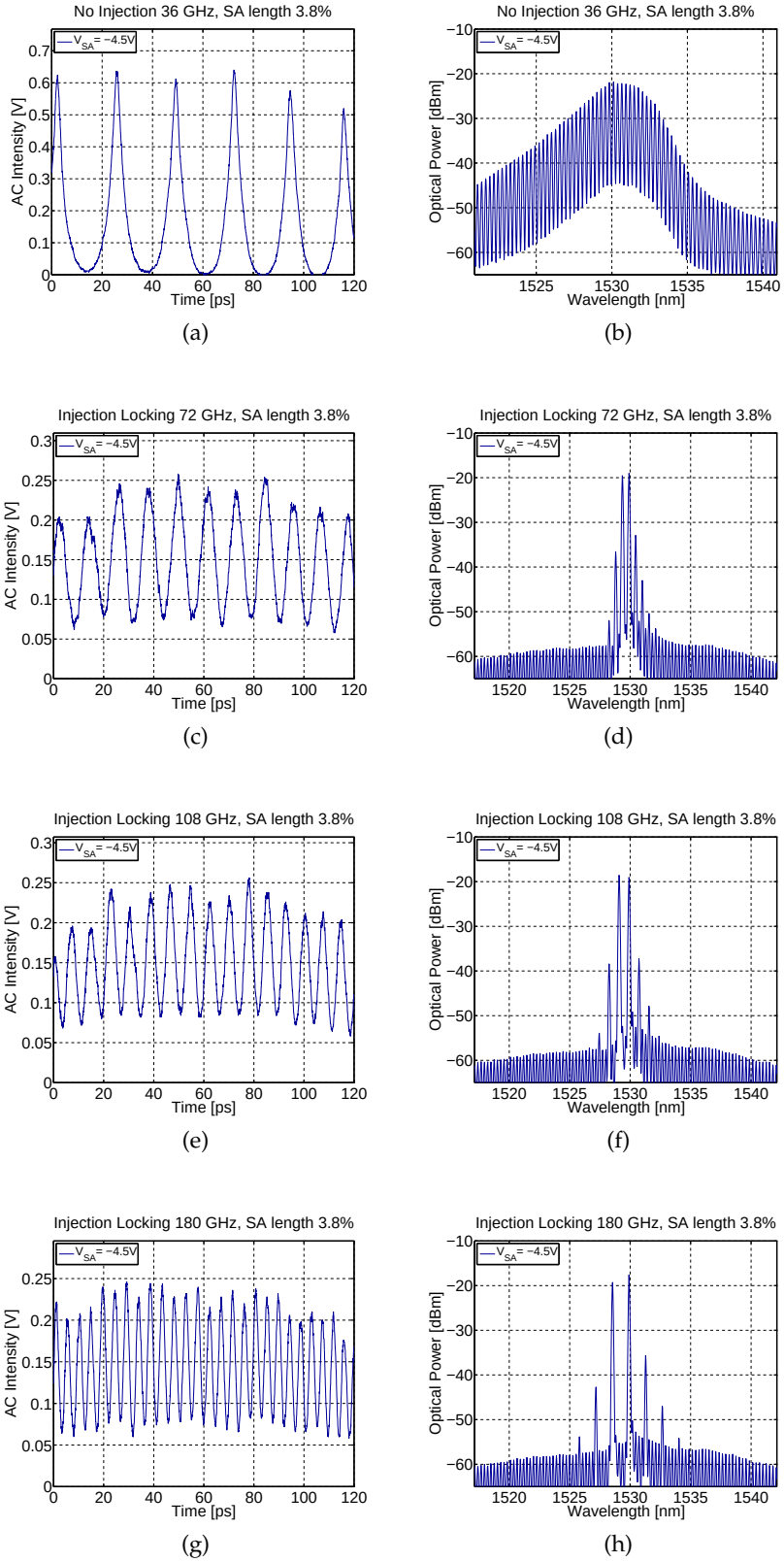

Figure 3.3: IAC and OSA traces from an injection-locked 3QW PMLL, showing discrete wide tunability of repetition rate for a series of injection signals separated over the range 36-180 GHz.

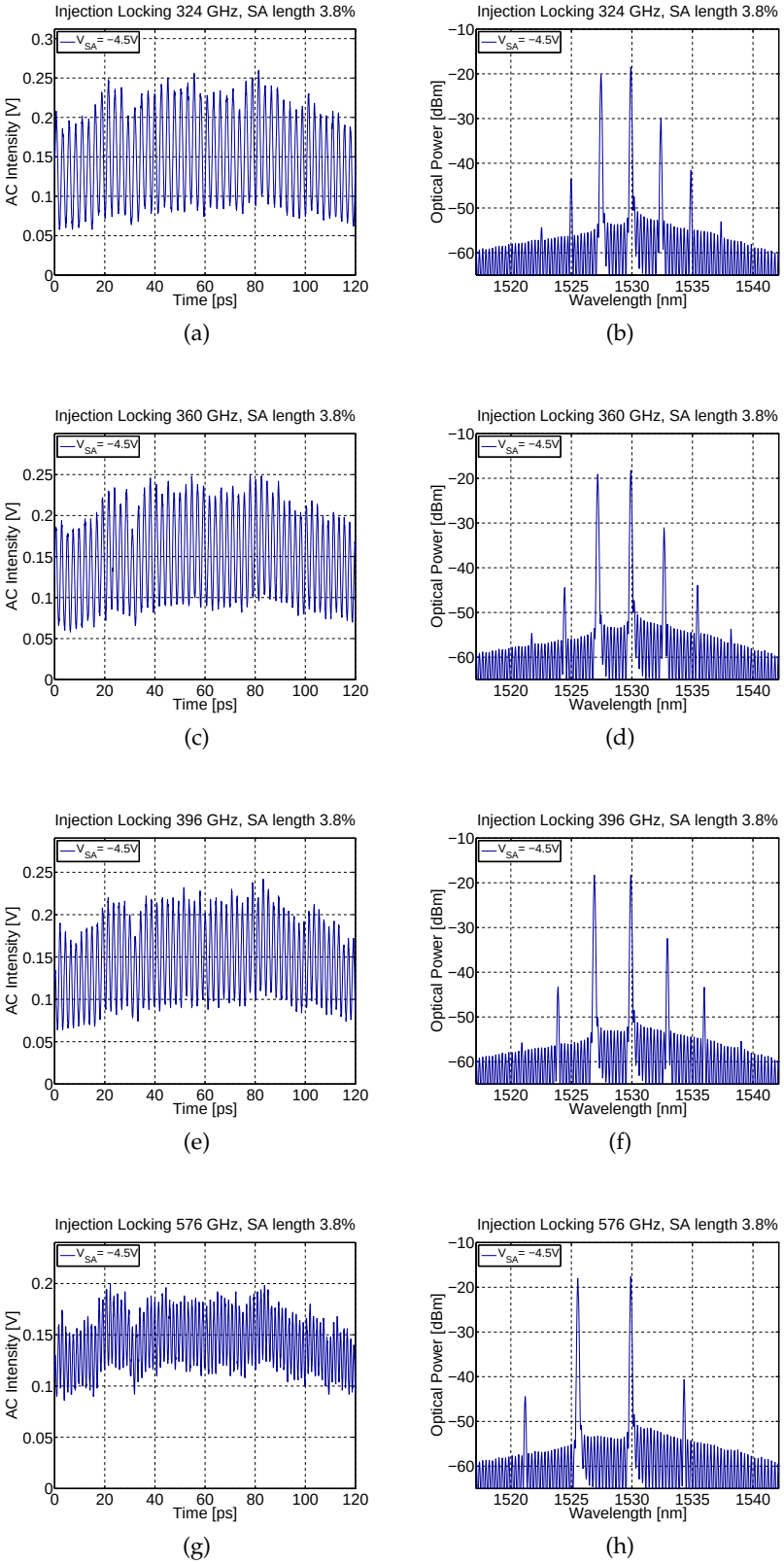

Figure 3.4: IAC and OSA traces from an injection-locked 3QW PMLL, showing discrete wide tunability of repetition rate for a series of injection signals separated over the range 324-576 GHz.

Before moving on to describing the assessment of the injection locking dynamics, it is worth analysing the phenomena responsible for the pulse generation. This is not the first time that high repetition rate optical pulses exploiting the beating of two CW signals have been reported. It is, though, the first time dual CW injection has been successfully exploited for frequencies above 160 GHz [141, 142]. Pitois et al. showed how an initial sinusoidal signal produced from the beating of two CW lines underwent temporal compression through Four-Wave Mixing (FWM) in a highly nonlinear fibre (nonlinear coefficient of 1.7 $W^{-1}Km^{-1}$), delivering high-quality sub-picosecond pulses. Fang et al. instead demonstrated high-repetition rate optical pulses through self-injection locking in a FP laser diode, attained by coupling the active device to an external Fibre Bragg Gratings (FBGs). These fibres were tuned to coincide with two longitudinal modes of the FP laser diode, allowing generation of high power and high repetition rate optical pulse trains. The two works cited above achieve pulses generation through FWM, and the harmonic ML shown in Figures 3.3 and 3.4 at a first glance might seem based on the same mechanism, with the FP mode-locked cavity acting as a nonlinear medium.
It must be pointed out though that in the cited works the maximum repetition rate reported was 160 GHz, and that those techniques do not allow wide tunability of the optical signals frequency. Given the wide tunability and stability of the signals obtained, it is thus a combination of multiple phenomena that stabilises the output allowing generation of ultra-high repetition rate optical signals. Besides FWM, the main contribution to the generation mechanism comes from hybrid ML [143]. Classic hybrid ML is a technique in which the SA of a PMLL is electronically modulated, forcing optical oscillations at the modulation frequency. In case of two injected CW lines, it is their beating that provides the modulation of the losses in the SA section, opening windows of net gain which lead to pulse formation at time intervals coinciding with the external line spacing. A diagram illus-

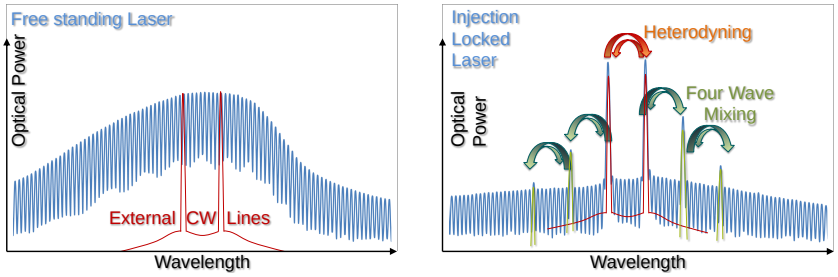

(a) Free-running PMLL optical spectrum (b) Injection-locked PMLL optical spectrum

Figure 3.5: Explanatory diagram depicting the optical spectra for (a) free-running and (b) injection locked 3QW semiconductor PMLLs, highlighting the effects participating to the locking mechanism.

trating the locking mechanism through the optical spectra is shown in Figure 3.5. Figure 3.5a shows a typical OSA trace from a 3QW passively mode-locked device, with the relative position of the injected wavelengths with respect to the spectrum. Figure 3.5b shows a schematic of CW external injection ML at the 9^{th} harmonic of the fundamental repetition rate, highlighting the FWM products and the beating between the injected signals.

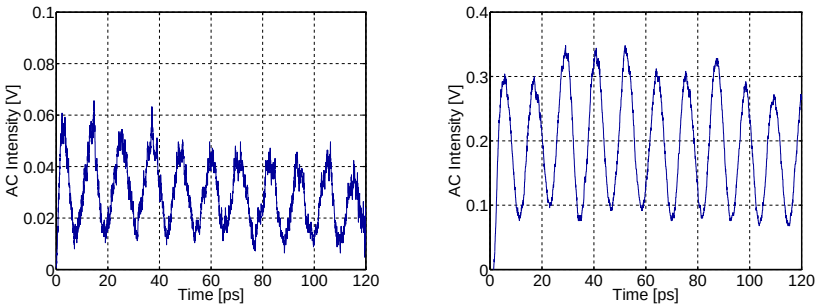

(a) Autocorrelation trace: injection from gain section side.

(b) Autocorrelation trace: injection from SA section side.

Figure 3.6: Comparison of IAC results between dual external injection applied on gain section side or on SA side.

Further evidence that heterodyning of the injected signals contributes to the harmonic ML mechanism was given by the observed dynamics when injection of the CW lasers takes place from the gain section side. Figure 3.6 compares the obtained IAC traces between external injection directly into the gain or the absorber region. Pulses were generated at harmonics of the fundamental also when the CW lasers were injected from the gain section side (Figure 3.6a) even though the improvement in the pulse quality when external injection was on the SA side is obvious (Figure 3.6b). The fact that a signal was obtained in both case suggests there is a contribution to signal generation from cavity enhanced FWM, but also that in order to stabilise and improve the quality of the signal, hybrid ML is needed. The SA acts as a photodiode, absorbing the external light and displaying a modulation in its carrier population that is consistent with the mutual spacing between the injected CW lines. The principle is the same as optical heterodyne detection, and it is more effective when the CW signals beat directly on the SA rather than after propagation through the entire device.

Several devices were extensively characterised to gain a better understanding of the dual external injection ML phenomenon. The dependency of the injection locking on a range of different parameters was analysed, with the goal of optimising signal generation for high repetition rates.

3.3 ULTRA-HIGH REPETITION RATE GENERATION, DYNAMICS

In order to characterise the ML performance of the injected devices, analysis was mainly based on the IAC signal. For frequencies above 40 GHz, the IAC and the OSA traces were the only two sets of data available, given that was the upper limit for the RF spectrum analyser detected frequency. The differences between dually-injected and unperturbed behaviour were analysed using the RF traces at the fundamental repetition rate, whereas the main parameter used to assess ML performance of the injected devices at frequencies multiple of the fundamental was the "*pedestal*" to peak ratio, calculated using the following expression:

$$R_{AC} = 100\frac{\overline{AC}_{min}}{\overline{AC}_{max}} \tag{3.1}$$

where $\overline{AC}_{min}$ and $\overline{AC}_{min}$ are the IAC voltage values obtained after averaging the relative minima and maxima of the IAC trace, respectively. The amount of pedestal displayed by the IAC trace is a good indicator of the quality and effectiveness of ML operation. The pedestal was therefore characterised for a wide range of passively mode-locked devices under several operational regimes. Devices with different SA section lengths were analysed, and their injection ML assessed for a variety of reverse voltages applied, determining the maximum achievable repetition rate in each case; the response to the level of externally injected power was also explored, as well as the maximum detuning between the injected CW lines and the modes of the PMLL before the disappearance of the pulses at harmonic frequencies. The injection locking behaviour was fully assessed, and its dependency upon absorbing length, applied reverse voltage, injected CW power and detuning will be discussed in the next paragraphs.

3.3.1 *Injection at the fundamental frequency*

The Full-Width at Half Maximum (FWHM) of the RF signal obtained from a mode-locked device is a good indicator of the ML quality, since it can be used to quantify the amount of jitter affecting the pulse train [144]. A jittery train of pulses will give rise to a broad RF signal (few MHz), whereas a stable and robust oscillation will provide much narrower RF lines. This is because in a semiconductor PMLL the leading edge of a pulse is attenuated more than the trailing edge, due to the saturable absorption characteristics of the SA section. This leads to intensity noise and gain fluctuations, which through the nonlinearity of the medium translate into a temporal shift of the pulse. The temporal interval between consecutive pulses will therefore experience fluctuations, which will be mirrored on the linewidth of the RF signal obtained by direct detection on a fast photodiode [145]. The use of

RF techniques is not the only viable way to analyse the timing jitter affecting PMLLs output pulses: approaches based on the analysis of optical cross-correlations have been shown to provide higher resolution [146], and they would especially suit the assessment of timing jitter for signals whose frequency is beyond the limit of standard RF analysers, as for the present work. The timing jitter assessment discussed here has been characterised only for operation at the fundamental repetition rate with and without external injection. However, the optical cross-correlations technique could be used as part of future work to complement the analysis, providing data for higher frequencies. The injection of two external signals acts as a frequency reference for the pulse travelling within the cavity, therefore an injected PMLL should exhibit a narrower RF signal than the one produced for free-running operation. Unperturbed and externally injected ML at the cavity fundamental frequency were compared, mainly focussing on the changes observed in the FWHM of the RF signal. For the experiments the setup of Figure 3.1 was used, with the RF data fitted with a Lorentzian function in post-processing and the FWHM extrapolated.

Figure 3.7 shows both the measured and fitted RF spectra and relative FWHM for the unperturbed case (Figure 3.7a) and for the dual CW injection at the fundamental frequency (Figure 3.7b). A shift in the frequency of the RF peak by almost 800 MHz can be observed, and this is due to the fact that the spacing between the two external CW lines could not be tuned to coincide exactly with the PMLL fundamental mode spacing. However, since the injection level was 0.012 with respect to the laser output power (weak to moderate injection regime), stable locking took place even with a 800 MHz detuning, meaning the point of parameter space K-$\Delta\omega$ considered still fell within the stable locking zone. Besides the central frequency pulling, the FWHM of the fitted Lorentzian line showed a reduction from 1.375 MHz to 1.266 MHz, an 8 % narrowing. Despite the small improvement, devices with several absorber lengths were characterised and they consistently showed a narrowing of the produced RF line when subject to dual CW external injection at the fundamental frequency. In fact Figure 3.8 shows the comparison between unperturbed and externally injected behaviour for the laser with the longest SA, which provided the widest RF line for free-running ML operation. It can be seen the extrapolated RF linewidth decreases from 35.25 MHz down to 24.88 MHz under external injection, corresponding to a 29 % reduction.

The linewidth reduction becomes more obvious for longer absorbing sections, because the output trains of pulses are more affected by timing jitter and profit more from the introduction of a fixed frequency reference within the cavity. The injection locking experiments at the fundamental frequency have proved there is a reduction of the timing jitter affecting the pulse. It is reasonable to assume that also at high repetition rates, where RF analysis was unavailable, the dual

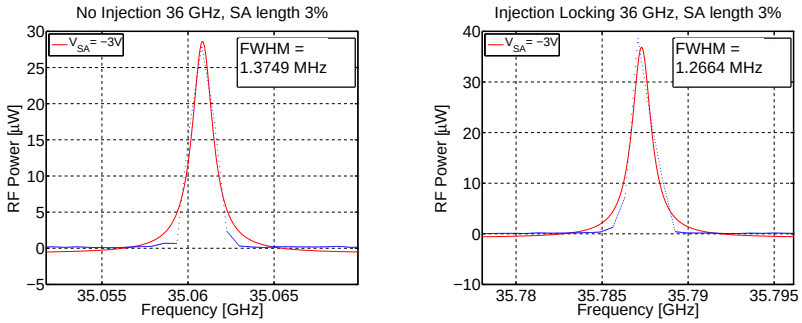

(a) RF trace: no external injection. (b) RF trace: injection locking at 36 GHz.

Figure 3.7: RF spectra comparison between free-running operation and dual CW injection at the fundamental repetition rate, for a device with SA length being 3 % (37 µm) of the total cavity length (1240 µm), reverse biased at −3 V.

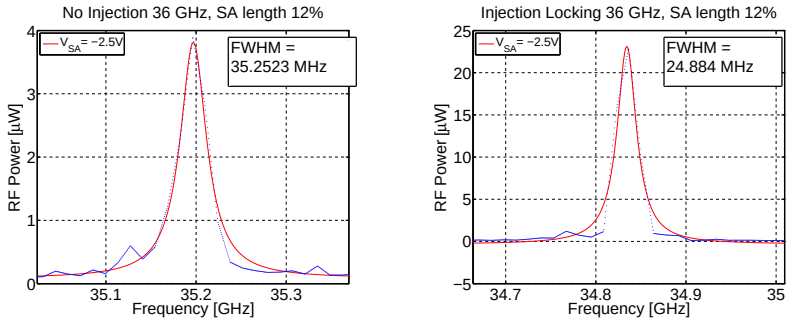

(a) RF trace: no external injection. (b) RF trace: injection locking at 36 GHz.

Figure 3.8: RF spectra comparison between free-running operation and dual CW injection at the fundamental repetition rate: SA 12 % (149 µm) of the total cavity length (1240 µm), reverse biased at −2.5 V.

CW injection ML gives rise to a stabilisation in the optical signal and a reduction of the timing jitter.

3.3.2 *Maximum repetition rate achieved*

The first and most important goal of the experiments was the generation of optical signals at ultra-high repetition rate, therefore the initial focus was mainly on maximising the wavelength spacing between the injected CW lines while still having oscillations displayed on the IAC trace. The system showed that when the external injection was aligned with two lasing modes of the cavity the IAC trace would display a signal at a frequency corresponding to the mutual spacing between the injected CW signals. Discrete tunability with a step equal to the FP cavity mode spacing was observed, and for the best case the achieved repetition rate varied between 2 and 26 times the fundamental frequency. Harmonic locking at 26 times the FP cavity mode

spacing corresponds to a frequency of 936 GHz, the highest reported for injection locked monolithic devices to the best of the author's knowledge. Figure 3.9 shows the IAC trace and the OSA output for the maximum repetition rate attained. The PMLL used had a SA section whose length was 1.8 % of the total cavity length (it was the device with the shortest SA between those tested) reverse biased at −3.5 V, while the gain section was pumped at $\sim 2I_{th}$ (70 mA) and the external lasers injection power was set to 250 µW for both.

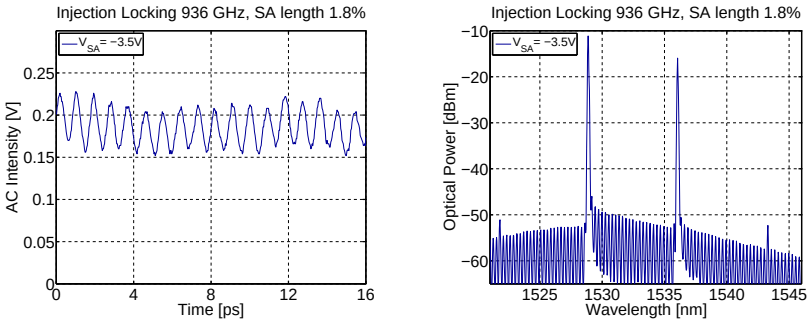

(a) Autocorrelation trace: injection locking at 936 GHz.

(b) OSA trace: injection locking at 936 GHz.

Figure 3.9: IAC and OSA traces for the maximum repetition rate attained through dual CW injection locking.

It can be seen how the traces display a ∼70 % pedestal, since with such a wide spacing between the injected CW lines the period of the generated signal is below the SA typical recovery time [147]. This is the main parameter in determining the maximum repetition rate at which injection locking can be achieved, since the losses in the absorber section must completely recover between consecutive pulses. The absorber recovery time cannot go below few ps, even with a strong reverse bias applied, therefore the maximum repetition rate is limited to 936 GHz. The general trend that was observed for all devices and all reverse biases is an almost pedestal-free train of pulses for all free-running devices or for injection locking at few times the fundamental cavity frequency, with the pedestal growing as the mutual spacing and the subsequent injection-locked repetition rate increased. Figure 3.10 depicts the evolution of the pedestal to peak ratio as a function of the frequency of the pulse train for the device with the longest SA section (11.8 % of the total cavity length) having a reverse bias of −2.5 V applied.

It can be seen how the device evolved from a pedestal-free situation in the absence of external perturbation to a regime where a pedestal was present and grew consistently until oscillations at higher frequencies eventually disappeared from the IAC trace and the device returned to the unperturbed behaviour. A ∼30 % pedestal was generally observed for each device at the highest frequency for which dual CW injection locking was still stable. Figure 3.10 also shows that for

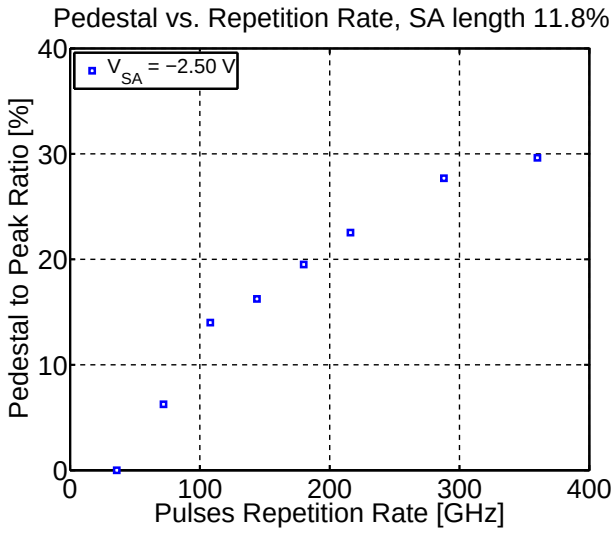

Figure 3.10: Evolution of the pedestal to peak ratio as a function of the injected laser repetition rate.

an 11.8 % SA the maximum attained frequency is ∼400 GHz, and not 936 GHz as it was the case for the 1.8 % SA. This is consistent with the losses being restored faster in a shorter absorber. The SA recovery time therefore poses a limit to the maximum repetition rate achievable, thus a device with the shortest possible absorber length must be used if priority is given to the attained repetition rate. As the next paragraph will show, however, longer SA sections are beneficial for other aspects.

3.3.3 *Dependence on SA characteristics*

The dependence of the injection locking performance upon the reverse bias applied to the SA section was assessed for all examined devices, comparing the pedestal to peak ratio in each case. The ML operation of the device was optimised prior to external injection, with the current in the gain section ranging from $\sim I_{th}$ to $\sim 3I_{th}$ and the SA voltages ranging from -0.5 V to -4.5 V depending on the examined device. As stated in Chapter 1, application of a reverse voltage shortens the SA recovery time, which otherwise would be too long to satisfy the fundamental ML condition and sustain stable pulses. Aiming at generation of ultra-high repetition rate optical signals whose periods could be as short as few picoseconds, a better performance was expected from the optically injected device under large SA reverse biases, allowing the losses in the absorber to follow the ultra-fast oscillation induced by the beating of the CW signals. This expectation was confirmed by the experiments, whose results are summarised in Figure 3.11; the two graphs compare the pedestal level between the 72 GHz and the 324 GHz case, both in terms of

dependence on applied reverse bias for the shortest absorber available (Figure 3.11a) and in terms of dependence on absorber length (Figure 3.11b).

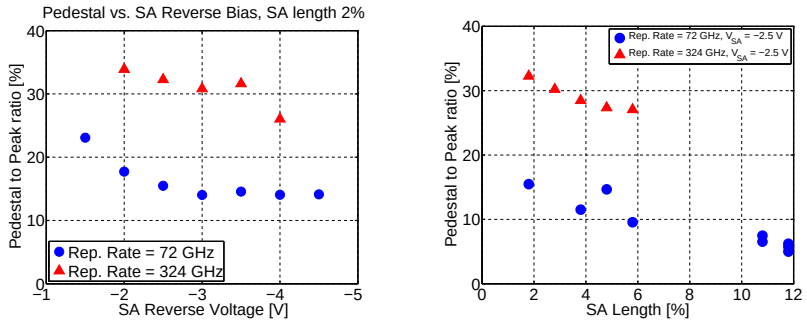

(a) L_{SA} = 2% V, pedestal comparison for injection locking at 72 GHz and 324 GHz.

(b) Pedestal comparison for injection locking at 72 GHz and 324 GHz for a fixed SA reverse voltage and variable absorbing length.

Figure 3.11: Evolution of the pedestal to peak ratio with respect to the SA voltage and length, comparison between two different repetition rates.

The two traces in Figure 3.11a show a reduction in the pedestal level when increasing the reverse bias for both cases of optical signal generation at 72 GHz and at 324 GHz, despite the different maximum and minimum levels of pedestal attained. This behaviour is consistent with expectations, since from previous experiments the shortest SA recovery times measured were few picoseconds [147], consistent with the period of a 324 GHz signal; the SA losses can be successfully modulated up to that frequency, with a fast decrease in the quality of the signal generation mechanism or this stopping altogether for higher harmonics of the cavity mode spacing. The upper repetition rate above which ML ceases is that point where the pulse spacing becomes shorter than the propagation time in the SA, therefore the next pulse occurs while the absorber is still being bleached by the previous one.

Regarding the pedestal evolution as a function of the SA length, it was observed that a longer SA section showed better injection locking performance for relatively low frequencies (2 or 3 times the fundamental repetition rate) but was unable to lock for frequencies above 10 times the fundamental mode spacing (360 GHz). Figure 3.12 compares the best IAC traces obtained from a PMLL locked at 72 GHz for the shortest (Figure 3.12a) and longest (Figure 3.12b) SA section examined. It could be seen how in one case the trace is almost pedestal free whereas a 25% pedestal is present for the shorter SA. On the other hand, the device for which the highest repetition rate was observed (at 936 GHz, previously shown in Figure 3.9) was the one having the shortest absorber (1.8%). The observed behaviour is coher-

ent with longer absorbers having a greater response to the beating of the external CW signals, maximising the heterodyning phenomenon and resulting in better quality ML. At the same time, as already said, the losses in such absorbers stop recovering for lower repetition rates. The presence of a trade-off between maximum achievable repetition rate and quality of the generated signals appears therefore quite obviously from the experiments that explored the injection locking dependence on the SA parameters; devices with short SAs display great tunability at the expenses of the pulse quality whereas long SAs allow pulses with better quality but limited frequency range.

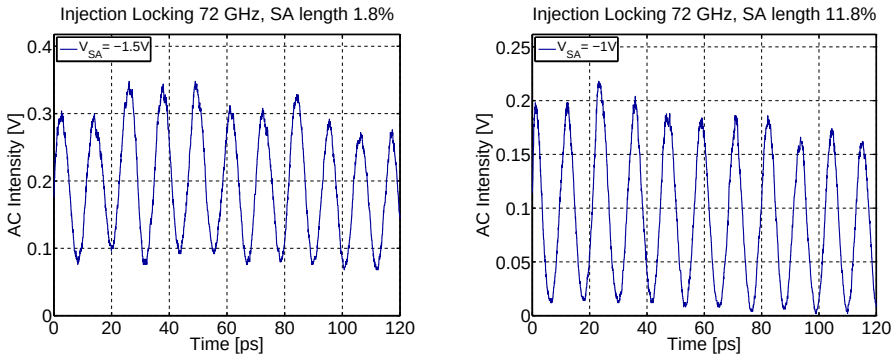

(a) IAC trace for injection locking at 72 GHz for the *shortest* SA length measured.

(b) IAC trace for injection locking at 72 GHz for the *longest* SA length measured.

Figure 3.12: Comparison of injection locking performance for different lengths of the SA section.

3.3.4 *Repetition Rate Detuning*

As previously stated, all devices proved discrete tunability over multiples of the cavity FSR, even though each one to a different extent. Besides the discrete tuning of the repetition rate, an interesting aspect to explore regards the injection locking sensitivity to detuning of the CW spacing, that is how much the injected CW could be detuned from a situation of perfect alignment with the laser modes before the high repetition rate signals disappeared. In order to do this, the injection locking operation was optimised, with the same injection strength used for the RF linewidth characterisation ($K = 0.012$), before detuning one of the injected wavelength to check over which interval the device was able to maintain injection locked operation. It was observed that tuning the wavelength of one of the CW lasers by one picometer (corresponding to a change in frequency of $\sim$125 MHz) caused a partial unlocking between the FP cavity modes and the externally injected optical lines. This happened for all cases where the spacing between the external CW line was greater than the fundamental repetition rate. The comparison between a good injection

locking situation and one in which one of the laser is detuned by one picometer is shown in Figure 3.13. The partially unlocked IAC trace displays a superposition of the free-running pulse train with a 36 GHz frequency, and the injection locked case with a signal oscillating at 180 GHz.

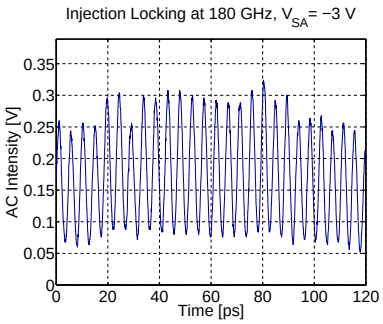

(a) IAC trace with external injection at 180 GHz, tuned.

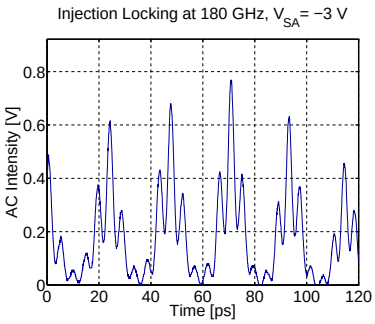

(b) IAC trace with external injection at 180 GHz, 1 pm detuning.

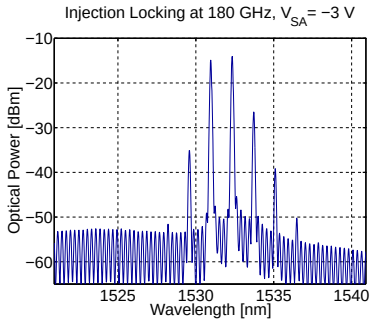

(c) OSA trace with external injection at 180 GHz, tuned.

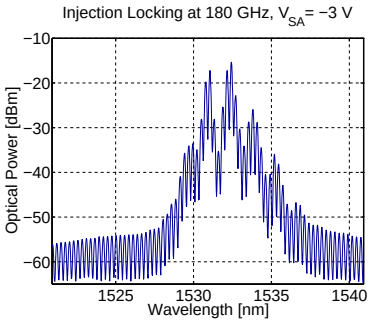

(d) OSA trace with external injection at 180 GHz, 1 pm detuning.

Figure 3.13: Comparison between tuned and detuned locking conditions.

The displayed results regard a PMLL whose SA section is 3.8 % of the total cavity length locked at $180GHz$ with -3 V applied to the absorbing section, but a similar behaviour was observed independently of the SA parameters or of the initial injection locked repetition rate; a partial unlocking was always observed when one of the externally injected lines was detuned by one picometer with respect to the optimised case. This might seem surprising if the results are compared with dual injection at the fundamental repetition rate, where the external signals would "*pull*" the emission by ∼800 MHz. However, in that case the external signals were spaced only 36 GHz, therefore they were not trying to lock the emission at a different repetition rate. When locking at higher frequencies the dynamics are different, and a better understanding can be gained considering that the typical optical linewidth of a FP cavity mode for the considered material platform is ∼10 MHz. When one of the CW lines is detuned by ∼125 MHz, it will try to "*pull*" the entire comb of cavity modes towards a

narrower spacing so that the injection locked situation is preserved. This mechanism will succeed only partially and only for the closest modes in the wavelength domain, therefore the resulting trace in the time domain will show a superposition of free-running and injection locked operation.

3.3.5 *Dependence on injection strength*

As already pointed out, the strength of the injection for the experimental results reported so far was $K = 0.012$, falling in the weak to moderate injection regime. This corresponded to the injecting lasers output power set to 250 µW. This value of laser power, corresponding approximately to ∼12 µW coupled into the PMLL cavity, proved to be sufficient for effective injection locking across a wide number of devices and SA voltage. The effect of a higher power was investigated for several devices and repetition rates, and again the experimental data showed that an increase in injected power could be beneficial but only to a certain extent. With an increase in the lasers power up to 1 mW ($K = 0.05$) the generated train of pulses showed a lower pedestal, while increasing the power further ($K > 0.05$) would cause the slave device to collapse into dual mode emission and the pulses to disappear from the IAC trace. The improvement in the generated pedestal is shown in Figure 3.14, which compares the IAC and OSA traces for injection at 250 μW and 1 mW, leaving all the other laser parameters (current in the gain section, lasers wavelength and mutual spacing) unchanged. Despite the OSA trace not displaying noticeable changes, the IAC pulses have a clearly lower pedestal under stronger injection. It is worth mentioning that the detuning behaviour has been re-assessed also under strong injection conditions ($K = 0.05$), and as expected it still showed the same results as previously stated.

3.3.6 *Dependence on injection wavelengths*

All the experiments have been carried out aligning one of the external CW lasers to the peak of the OSA trace and successively tuning the second CW laser depending on the desired repetition rate. Further tests were carried out in order to assess if this configuration was the one that optimised the generated optical pulses, or if there could be an improvement in the quality of the injection ML by shifting the injected wavelength towards the blue or red end of the spectrum.

Figure 3.15 compares the IAC and OSA traces for injection locking at 72 GHz changing the wavelength of the external injection. This was the only parameter changed between the different graphs, whereas other PMLL parameters (SA reverse voltage, gain section current, injected power, sub-mount temperature) were left untouched. The traces show that a better performance is obtained for the *centred* injection,

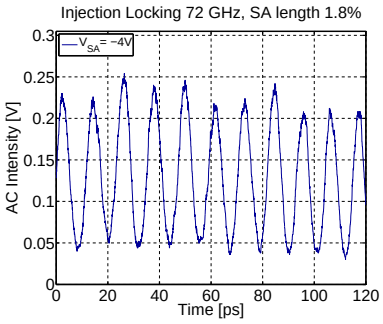

(a) IAC trace with external injection at 72 GHz, lasers power 250μW.

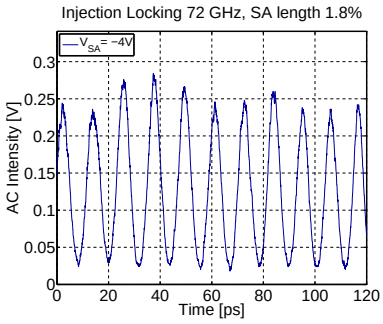

(b) IAC trace with external injection at 72 GHz, lasers power 1 mW.

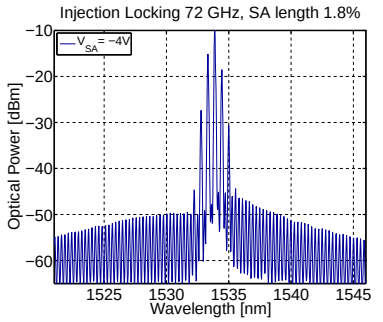

(c) OSA trace with external injection at 72 GHz, lasers power 250μW.

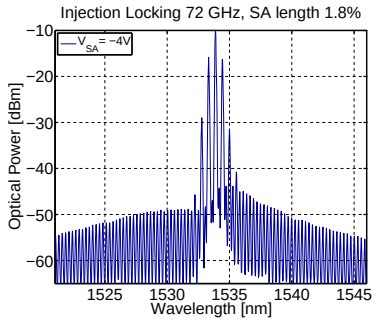

(d) OSA trace with external injection at 72 GHz, lasers power 1 mW.

Figure 3.14: Comparison between low injected power and high injected power locking.

giving a pedestal to peak ratio value of 9 %, whereas the *red* injection showed 17 % and the *blue* injection provided the worst result with a 21 % pedestal. The OSA trace for the *centred* injection also shows the FWM products being ∼10 dB higher than in the other two cases. This behaviour can be explained by the fact that the unperturbed PMLL optical spectrum peak wavelength is due to the relative position of the gain curve with respect to the SA bandedge [7], therefore an overlap of the externally injected CW lines with the centre of the spectrum ensures that also the optical signals generated at higher harmonics profit from optimal gain-SA dynamics. Thus stable injection locked optical signals will be obtained for the injected wavelengths being symmetrical with respect to the peak of the optical spectrum, in accordance with the results from the *centred* injection case.
Another thing worth discussing is the fact that once fixing one of the CW signals in correspondence with the peak of the optical spectrum, more stable injection locked IAC traces are obtained when the other CW line is chosen to be on the blue side of the spectrum. This is consistent with the well known fact that is easier to lock the emission of a slave laser for the case of a negative detuning [148, 149]. Furthermore, recent experimental results on quantum-dot PMLLs and FP lasers measured by an injection locking method suggest that devices

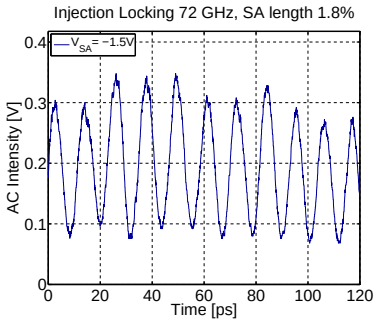

(a) IAC trace for injection locking at 72 GHz, *centred* injection.

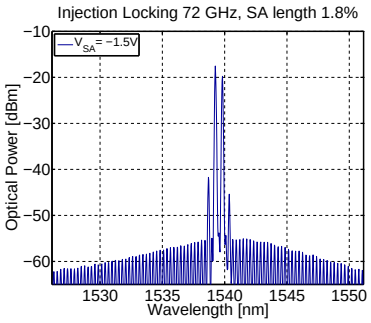

(b) OSA trace for injection locking at 72 GHz, *centred* injection.

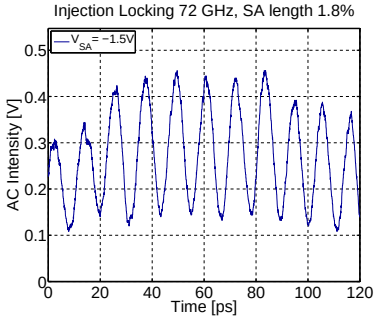

(c) IAC trace for injection locking at 72 GHz, *blue* injection.

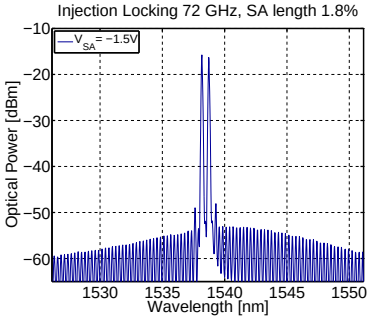

(d) OSA trace for injection locking at 72 GHz, *blue* injection.

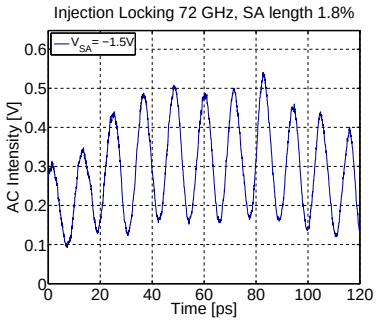

(e) IAC trace for injection locking at 72 GHz, *red* injection.

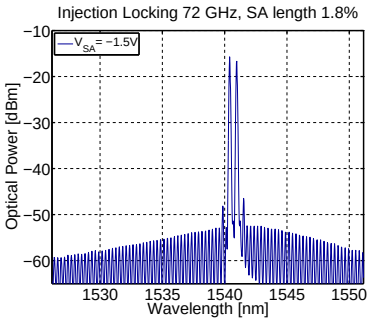

(f) OSA trace for injection locking at 72 GHz, *red* injection.

Figure 3.15: Comparison of IAC and OSA traces between *centred*, *blue* and *red* injection locking at 72 GHz.

operating with a ∼10 nm blue-shift from the gain peak exhibit shorter output pulses with lower chirp [150], also supporting the configuration employed in this work.

3.4 CONCLUSIONS

The experimental data have shown how dual CW injection can be a successful technique for generation of optical pulses at ultra-high frequencies (> 100 GHz). Wide discrete tunability has been demon-

strated up to 936 GHz, corresponding to 26 times the fundamental mode spacing of the cavity (36 GHz). Despite the obtained repetition rate not being the highest ever obtained from an integrated mode-locked device (2.1 THz were obtained in [45]), it is the first time a monolithic PMLL is shown to emit stable pulses with such wide tunability (900 GHz) on a 36 GHz grid. The performance is thought to be limited mainly by the absorption recovery time, with the lowest value measured in [147] being 2.5 ps even with −4 V applied to the SA section. This translates in the losses not completely recovering between consecutive pulses for repetition rates above 400 GHz, and explains why 936 GHz was the maximum achieved in this work, and why it was only obtained for the shortest available absorber (1.8 % of the total cavity length, corresponding to 22 µm) providing the shortest loss recovery time between the devices tested. Another factor limiting the maximum repetition rate is the lasers gain 3 dB bandwidth, which is ∼30 nm for the considered MQW material platform [6, 7]. A 936 GHz mode spacing corresponds in wavelength to 7.3 nm, ∼25 % of the gain bandwidth, meaning that only 5 modes are lasing and can be locked. The higher the frequency of the generated optical signals, the lower the number of modes participating to the locking mechanism, but ML will still be possible as long as at least 2 modes are lasing. This suggests that if sub-ps absorption recovery times can be obtained, external injection could successfully induce locking at repetition rate beyond 1 THz.

The discussion has analysed the dependence of the injection locking mechanism on a number of system and device parameters, and despite some of the results for the detuned injected wavelengths not being completely satisfactory (with the slave PMLL unlocking for a detuning of 125 MHz), this is thought to improve with integration of the technique on a single chip. In that case there would not be optical isolation between the injecting lasers and the mode-locked ones, with beneficial effects on the injection locking mechanism, making it more robust because of the mutual feedback between cavities. The technique proves suitable for integration on a monolithic platform, with several possibilities available for implementation of the CW lasers and PMLLs on the same chip. Research towards integration approaches has been carried out and the obtained results will be discussed in the next chapter.

4

ULTRA-HIGH REPETITION RATE GENERATION, INTEGRATION

There would be many advantages in tranferring the injection locking mechanism described in the previous chapter on a monolithic chip: besides the general advantages of an integrated optical chip such as compactness and low cost, first of all the coupling between master and slave devices would greatly improve; furthermore, the polarisation of the three signals involved would be automatically matched; finally, the level of injection could be simply controlled by placing integrated absorbers between the CW lasers and the injected PMLL. Several approaches could be used to transfer the proposed configuration on a monolithically integrated platform, and they will be described in the following sections. Furthermore, an integrated configuration involving coupled ring cavities will also be presented; despite not being a transposition of the injection locking technique described in the previous chapter, it is a promising approach for on-chip generation of THz signals using coupled cavities effects, and it has therefore been included in the description.

4.1 OPTIONS FOR DUAL INJECTION LOCKING INTEGRATION

The first elements needing integration would be the external CW lasers, which would need to be fabricated on the same chip as the PMLL. The most direct and obvious possibility to integrate a CW single-mode optical source on a chip is to rely on a SRL or on a DFB laser. The Optoelectronics Group at the University of Glasgow has expertise in the fabrication of both kind of devices, and both could provide wavelength tunability through current and temperature tuning. The SRLs are less controllable with regards to the lasing direction and wavelength stability, issues not present in the DFB laser but at the price of higher fabrication complexity because of the grating definition. As for the PMLL, the standard cavity with a linear FP geometry would have to be abandoned in favour of a mode-locked structure that allows routing and coupling on chip of the signal from the CW lasers. Again the use of SRLs is a possibility also for PMLLs, with different configurations available depending on the number of absorbing sections and their position with respect to the output coupler, as shown in Figure 4.1.

The first ML configuration based on SRLs has a single SA placed symmetrically opposite the output coupler, so that counterpropagating pulses will experience similar conditions and exit the ring simultan-

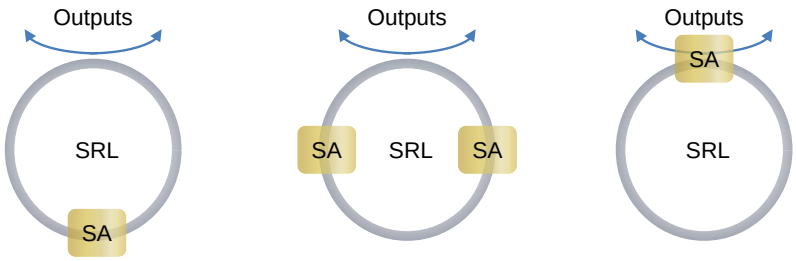

(a) Symmetric single SA configuration.

(b) Symmetric dual SA configuration.

(c) Output coupler SA configuration.

Figure 4.1: Illustration of the different configurations available for ML in SRLs.

eously (Figure 4.1a). Despite this being the most simple and obvious ML scheme for a SRL, the best pulse characteristics are given by symmetrically placing two SAs in the cavity [151], as shown in Figure 4.1b. Such implementation is not compatible with injection locking, given the importance of coupling the external CW light directly into the SA, so a scheme as the one in Figure 4.1c is needed.
Given these considerations, three possible routes for generation of high-repetition rate optical signals on chip have been identified, all of them depicted in Figure 4.2:

- The first approach exploits two DFB lasers as integrated sources of CW signals, with their output combined in a single waveguide through an MMI coupler and subsequently coupled into a SRL mode-locked cavity by means of a directional coupler, as shown in Figure 4.2a. As previously stated the CW lines need to be coupled directly into the absorber, making the dual SA mode-locking configuration unsuitable and requiring a single SA contact placed on the directional coupler; secondly, the intrinsic behaviour of SRLs makes it impossible to anticipate if the clockwise or anticlockwise direction will be preferred for lasing, therefore two DFB lasers are needed on each side of the SRL to ensure co-directionality between the injected CW signals and the lasing modes. Finally, several sets of DFB lasers covering a broad spectral range are necessary as well, since it is not possible to predict exactly the wavelength at which the SRL lases.

- The second proposed approach relies on two DFB lasers injecting in a semicircular PMLL. Between the integration options, this is probably the most similar to the technique demonstrated with discrete components, and it would require half the chip area compared with the previous approach. Figure 4.2b illustrates this technique for injection in a CPML laser, even though injecting into a single SA positioned next to the cleaved facet could also prove effective for generation of high frequency optical sig-

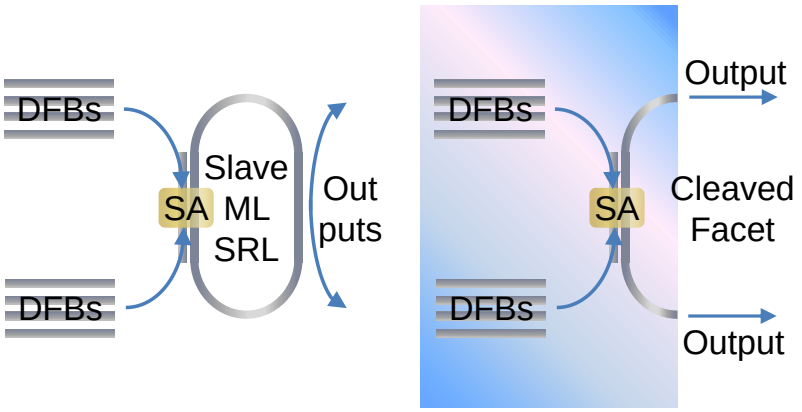

(a) Integrated injection locking scheme, DFBs in mode-locked SRL.

(b) Integrated injection locking scheme, DFBs in CPML laser.

Figure 4.2: Schemes depicting the available configurations for on-chip generation of ultra-high frequency optical signals.

nals. The difference between the two cases is the amount of optical feedback in the DFBs cavities, minimised if the injecting laser is not subject to direct reflection from the facet. A certain amount of optical feedback is thought to sustain the injection locking mechanism, whereas too much would hinder and eventually stop the lasing operation.

It must be mentioned that since all proposed devices involve curved geometries, their fabrication on the 3QW material platform is not advised; despite this material displaying improved ML performance for PMLLs in a FP cavity configuration, the far-field reduction layer pulling the mode down increases bending losses and makes it unsuitable for SRLs fabrication. For this reason the fabrication of all devices involving curved waveguides took place on the 5QW material.

4.2 HARMONIC LOCKING THROUGH VERNIER EFFECT

Generation of optical signals at higher harmonics of the PMLL fundamental repetition rate can also be obtained by exploiting the interaction of only two coupled cavities, thanks to a phenomenon called Vernier effect. This section will briefly explain this phenomenon and how it can be applied to laser cavities for several applications, before presenting the experimental results from coupled SRLs.

4.2.1 *Vernier Effect*

The Vernier effect is well known for its application in high-resolution distance measurements, but its principle can be applied also to optical combs and it has been applied to expand the tuning range of

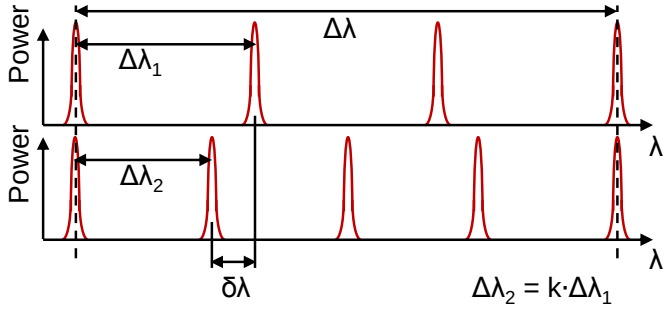

Figure 4.3: Longitudinal modes spectra for two laser with different FSRs. A 25 % shift of the FSR leads to a shift of the point where the two combs coincide by $12\delta\lambda$.

semiconductor lasers [152]. It is based on the fact that two optical combs whose FSRs differ by $\delta\lambda$ will coincide for wavelengths spaced by:

$$\Delta\lambda = \frac{\Delta\lambda_1 \Delta\lambda_2}{\delta\lambda} \tag{4.1}$$

This effect is depicted in Figure 4.3; in the case of the two optical combs being reflection spectra of the two mirrors of a FP cavity laser, lasing can only occur for wavelengths where both reflection combs are non-zero, which yields a large tuning capability for the semiconductor laser, limited only by the gain bandwidth. The practical implementation of the comb-like reflection spectra is normally achieved through spatial Bragg gratings, generally sampled gratings [153]. The Vernier effect has been applied not only for wavelength tuning of active devices, but also for increasing the FSR of ring resonators fabricated on Silicon-on-Insulator (SOI) platforms while avoiding the non-negligible bending losses experienced when the ring radius is less than few µm [152, 154]. Moreover, it was also exploited for mm-wave generation using DBRs and DFB lasers injection into SRLs [155]. In this work the Vernier effect has been used as mean for generation of quasi-THz repetition rate optical pulses, based on the chip design presented in Figure 4.4. It is based on the combination of two SRLs, with the one dubbed the "slave" device being mode-locked by placing one or multiple SAs within the cavity.

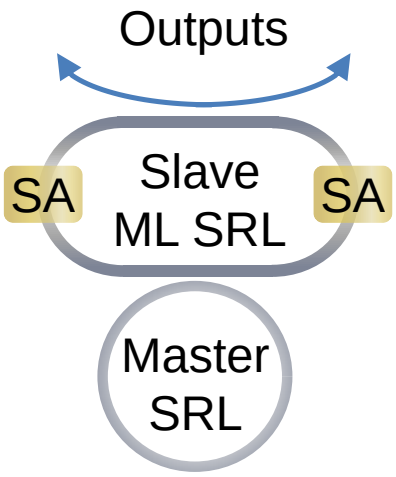

Figure 4.4: Scheme depicting the chip topology for mutually coupled Vernier SRLs.

The device dubbed "master" laser would also be a SRL, but with continuous wave emission (without SAs). Since both devices share the same material, by a proper design of the respective cavity lengths the Vernier effect can be exploited in order to achieve an overlap between the optical combs only every N modes. Optical injection from the master CW into the slave mode-locked SRL will then induced pulsed emission at the cause its pulsed emission at the N^{th} multiple of its fundamental repetition rate. The validity of this technique for pulsed emission at very high repetition rates (up to THz) has been tested experimentally; the results are object of the next paragraph.

4.2.2 *Coupled ring cavities, experimental results*

A chip containing coupled cavities SRLs was fabricated on the 5QW material. The FSR of the "slave" mode-locked laser was chosen to be 60 GHz, corresponding to a cavity length of ∼1.4 mm. All fabricated mode-locked SRL had a racetrack cavity to facilitate output coupling of the laser light. The length of the output coupler was 234 µm and the gap between the ring and the output waveguide was chosen to be 800 nm in order to provide ∼30 % coupling. The "master" SRLs were chosen to be circular so that injection would take place through a point coupler. The master SRL was designed to have an output coupler as well for monitoring purposes. An optical microscope image of one of the devices fabricated is shown in Figure 4.5.

The two coupled cavities are pointed out in the picture, both the slave and the master one. The output waveguides can also be seen for both lasers; it is worth mentioning that the they are tilted by 10 ° next to the cleaved facet to minimise back-reflections. The gap of the point coupler used for mutual injection was chosen to be 800 nm, cor-

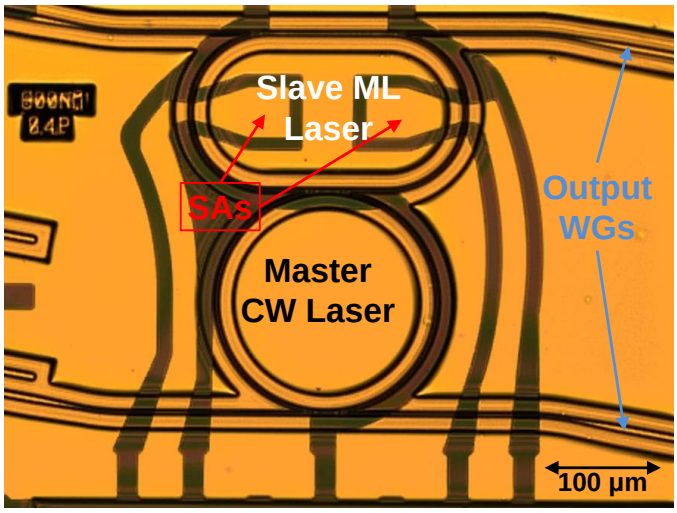

Figure 4.5: Optical microscope image depicting one of the fabricated Vernier devices.

responding to a simulated mutual coupling of 0.4 %. While the FSR of the slave SRL was fixed to 60 GHz, that of the master ring had a different cavity length for each device. It was decided to fabricate the following ratios between coupled cavities: 5/6, 10/11, 15/16, and 20/21. For each ratio two sets of devices were fabricated with the total lengths of the absorbing sections being either 2 % or 5 % of the total cavity length, split equally through a dual contact split geometry. The large area occupied on the chip by each device did not allow evaluating a broader range of SA lengths or cavity lengths ratios. The choice of 2 % and 5 % SAs was motivated by the fact that they are known to provide the best ML performance for SRLs on the 5QW material [106].
The absence of external CW lasers made the experimental setup much simpler, with the output of the passively mode-locked ring first coupled into a tapered fibre lens, and then split by a fused coupler with a 9 : 1 ratio between an auto-correlator and an OSA for monitoring purposes. Unfortunately a stable IAC trace displaying clean ultra-high repetition rate optical signals was never obtained no matter what device, SA reverse voltage or current in the master or slave device was applied.
Some encouraging results were obtained though, with the most interesting behaviour presented by the two SRLs whose relative cavity ratio was 20/21. Characterisation of the single SRL cavities without external perturbation showed a well-known and documented behaviour, with both lasers displaying bidirectional operation close to threshold, then switching to unidirectional operation for increased pumping. After the unidirectional mode is reached, increase in current causes the cavity to alternate between the clockwise and counter-clockwise direction for different current intervals [156]. The non mode-locked SRL had a threshold current of ∼80 mA (correspondind to a current density J_{th} of 2.9 kA/cm^2), while the mode-locked one had a threshold of ∼125 mA (J_{th} = 4.8 kA/cm^2). With both devices turned on, best results were recorded with the injecting laser biased just below threshold, whereas an increase caused the mode-locked ring to collapse into single-mode operation at the same wavelength and direction of the other ring, suggesting an excessively perturbed cavity.
Figure 4.6 shows the wavelength map of the mode-locked SRL for a fixed current of 58 mA (∼0.66I_{th}) in the other laser. One of the SA was left floating while the other one had a reverse voltage of −1 V applied. The multiple peaks displayed by the optical spectrum have a spacing of ∼1.26 THz corresponding to 20 times the FSR of the mode-locked device (60 GHz). This is consistent with the cavities ratio and it confirms the non mode-locked one acts as a filter for the emission of the other SRL through the Vernier effect. The IAC trace presented a 70 % average pedestal and the superposition of two modulations corresponding to the frequencies of 60 GHz and 1.26 THz. Such behaviour was stable for currents in the mode-locked SRL ranging between 175

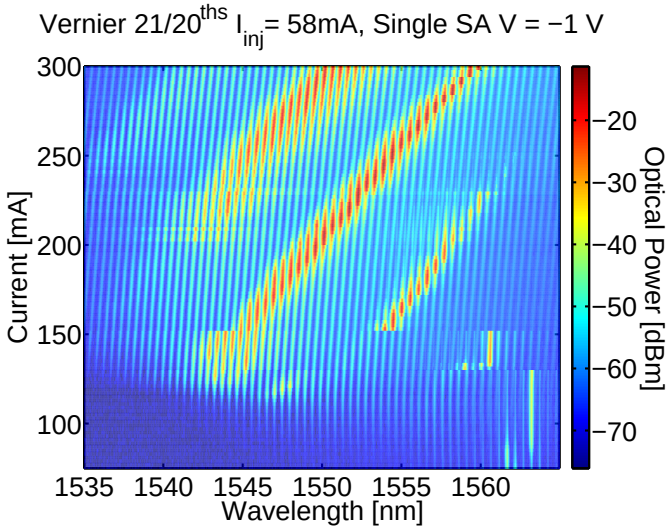

Figure 4.6: Wavelength Map for injected SRL for 58 mA in the round ring cavity.

mA and 255 mA, with the 60 GHz modulation component on the IAC trace minimised for low currents. Figure 4.7 shows the IAC and OSA traces for a current of 178 mA and 58 mA in the mode-locked and non mode-locked device, respectively.

The integrated Vernier devices have shown promising results, suggesting that an improved device design might lead to an effective generation of ultra-high frequencies pulses. The incomplete locking shown by the fabricated devices suggest the 0.4 % mutual coupling typical of a point coupler with a 800 nm gap is not enough for a good shaping of the produced pulses for high frequencies. One of the possible modifications could be increasing the injection between the master and slave SRL. Since a reduction of the gap between the waveguides below 800 nm would present RIE lag issues and possibly jeopardise effective device coupling, an alternative solution could rely on implementation of a racetrack geometry for the master SRL

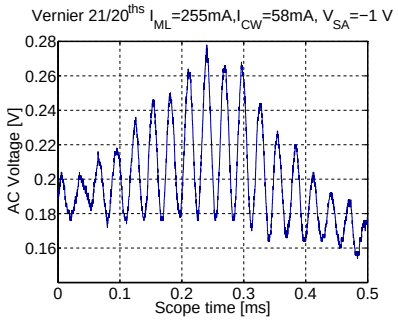

(a) IAC trace of Vernier integrated coupled cavities.

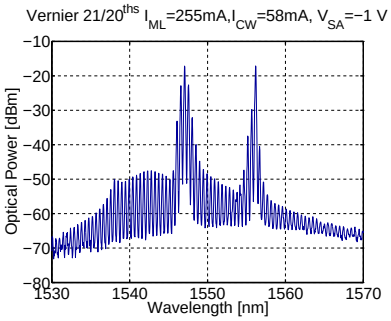

(b) OSA trace of Vernier integrated coupled cavities.

Figure 4.7: IAC and OSA traces for Vernier integrated coupled ring cavities.

as well, with the possible situations illustrated in Figure 4.8. The

(a) Coupling of racetrack SRLs.

(b) Coupling between SRLs with laterally shifted coupler.

Figure 4.8: Schemes depicting the available configurations for increasing the coupling between SRLs with respect to the point coupler case.

most straightforward way to couple two racetrack SRLs is using their straight sections to realise a directional coupler, as Figure 4.8a shows. Simulations have been carried out with BeamProp™to find the amount of optical power coupled between two waveguides having a length L of 234 μm (the same length as the straight section in the racetrack geometry for a 60 GHz ring) varying the gap d between them, with the results in terms of mutual coupled power displayed in Table 4.1. The fabrication of a variable gap between

Gap d [nm]	Coupling [%]
800	33
1100	10
1400	3

Table 4.1: Coupling ratio for different gap widths on the 5QW material, with a coupling length of 234 µm.

the non mode-locked and mode-locked SRLs can be challenging as very precise control of lithography and RIE lag is required. A simpler and more robust way to tune the coupling between ring cavities is a lateral shift of the devices with respect to each other, in order to change the coupling length, as shown in Figure 4.8b. The amount of power coupled as a function of the length follows a sine-squared law, therefore given a certain gap between waveguides the percentage of optical power mutually coupled between them could be precisely chosen simply by choosing an appropriate length L_1. The use of a racetrack geometry for both rings and the use of directional couplers can increase the mutual coupling, thus is likely to provide better results at high repetition rates. Care must be taken through the design stage so that the final Vernier devices will present a good balance between the benefit of an increased coupling to the locking mechanism and an excessive injection, where high perturbation might trigger complex phenomena; a coupling below a few percent would most likely prove ideal.

Another point which would need further investigation is the optimum length of the SA section, in the preliminary coupled SRLs the only absorbing lengths present were 2 % and 5 % of the total cavity length, but there is probably room for improvement regarding the ML stability and the range of currents over which ML takes place.

4.3 CONCLUSIONS

The first part of this chapter has reported on the possible routes for monolithic integration of the dual CW injection technique described in the previous chapter. The fabrication of integrated devices exploiting dual CW injection in a PMLL will be implemented in future work. The second part of this chapter has discussed a different technique to achieve harmonic locking of mode-locked SRLs, based on the Vernier effect. The best results were obtained from coupled micro-ring cavities having a 20/21 ratio between their cavity lengths, with one of the devices being mode-locked. Consistently with expectations, the optical spectrum displayed the superposition of two modal comb spacings, the FSR of the mode-locked device (60 GHz) and the spacing for which the combs of master and slave SRL overlap (1.26 THz). The IAC trace showed the same behaviour in the time domain, with the superposition of two modulations at 60 GHz and at 1.26 THz. The presence of the unwanted 60 GHz modulation and the high pedestal (70 %) measured in the IAC trace suggests the coupling between the two cavities (0.4 %, obtained by use of a point coupler with a 800 nm gap) was not optimised. Despite the further optimisation needed, the experimental characterisation shown in this chapter has confirmed the use of the Vernier effect as a potential route for THz-frequencies signal generation. Several approaches to change and optimise the coupling between master and slave SRL have been discussed, such as the use of standard directional couplers or laterally shifted ones, to be implemented in future work.

5

MODE LOCKING WITH INTERMIXED SATURABLE ABSORBERS

This chapter describes how a bandgap shift of the SA section can be used to improve the performance of PMLL lasers. The two QWI techniques described in Chapter 2 have been applied to induce a bandgap blue-shift in the SA regions, and the ML characteristics have been analysed and compared for QWI and as grown devices. The structure of this chapter is as follows: first the benefits of a detuned absorber bandgap will be discussed; the analysis of results from the intermixed devices employing both QWI techiques will follow, with particular attention to the way the SA detuning affects ML operation; finally, the last section will outline the main achievements and possible future work.

5.1 BANDGAP SHIFTED ABSORBERS, MOTIVATION

As explained in Chapter 1, a successful pulse formation is based on the joint action of gain and absorbing sections, with an optimum combination of gain and absorption characteristics. The operating conditions providing optimal SA performance are in contrast with those maximising the gain, therefore ML is typically limited to a narrow region of gain currents and reverse voltages on the SA by the fact that both gain and SA sections share the same material composition, unless especially targeted integration techniques are used. This was the case for the first application of bandgap wavelength detuning between SA and gain section [97], where a bandgap shift in the absorber was obtained by growing a material with different bandgap for the SA through selective area growth [157]. This is one of the active-passive integration techniques listed in Table 1.1, with its main advantage consisting in the flexibility to define different bandgaps on a single sample, allowing also to have both red and blue shifts in the bandgap. The downside of the selective growth technique is the added fabrication and epitaxial complexity because of the non planarity of the sample; moreover, there is a transition region between chip areas with different bandgaps and this composition gradient affects the spatial resolution. There was no mention of this issue in [97], where the main focus was on the changes affecting the temporal width of the pulse as a function of the induced bandgap shifts between gain and absorbing section. The cited work compared both *blue* and *red* detuning of the SA for a number of devices, with the best results given by blue-shifted SAs. In particular, detuning the bandgap of the SA towards shorter

wavelengths by 20 nm reduced the FWHM of the generated pulses by a factor of two in comparison with a non-detuned SA. This behaviour can be ascribed to a reduced absorption recovery time, following the fact that a blue-shifted SA is more transparent to the propagating optical mode and therefore needs a larger reverse bias to shift its bandedge until this and the peak of the gain curve are in the same situation as in the non-detuned devices. Increasing the SA blue shift too much though (above 25 nm) results in increased reverse voltage values to achieve the same recovery times, increasing the leakage current in the absorber as well.

Following the first demonstration of ML with bandgap shifted SAs, more recently Scollo et al. have reported on mode-locked devices whose SAs were detuned by 40 and 60 nm with respect to the bandgap of the emission (1530 nm), which were able to emit sub-ps pulses [158]. In both reports the aim of the research was the generation of ultra-short optical pulses. In [97] the main focus was the development of an effective pulse-shortening technique, and the best results were obtained with a 24 nm shift, providing pulse compression from 2.6 ps to 1.2 ps. In this work instead the primary goal of inducing a bandgap shift in the absorbing sections was to improve the emitted power performance of semiconductor PMLLs. The region of optimal ML operation for devices fabricated on the 3QW material is presently limited to low currents (∼100 mA) corresponding to a few milliwatts of total power. As the analysis presented in Chapter 1 has pointed out, good ML in MQW systems is obtained for limited intervals of gain section currents and SAs reverse voltages because of the wavelength-dependent properties of the absorbing section. Starting from a mode-locked situation, an increase of the current in the gain section induces a growth in the generated photocurrent of the SA section. The associated Joule heating causes the SA bandedge to drift towards longer wavelengths with respect to the bandedge of the gain section, thus the change in relative detuning between the two regions modifies the SA absorption properties, eventually leading to the ML mechanism being hindered or disappearing altogether.
Based on this theoretical interpretation for the interplay between gain and absorbing regions, a bandgap blue shift applied on an integrated SA would therefore be able to extend the ML range to higher currents. The photocurrent-induced Joule heating would of course still exist, but the blueshift of the SA will cause the optimal absorber-gain detuning for ML to occur for higher currents in the gain section with respect to a non-detuned SA. Moreover, the application of a bandgap shift to the SA region could increase the escape rate of the photo-generated carriers, leading to higher saturation intensities and narrower pulses. Between the possible approaches to induce a blue-shift in a MQW material platform, QWI is a good candidate, being a fully post-growth technique compatible with the standard fabrication flow and not re-

quiring complex re-growth steps. The QWI techniques described in Chapter 2 were therefore applied to fabricate FP lasers and PMLLs. Given the improved output power performance of PMLLs on the 3QWs material and the absence of curved structures from the designs (meaning bending losses were not an issue) the 3QW material was preferred over the 5QW one.

5.2 POST-ETCH QWI DEVICES, EXPERIMENTS

The *post-etch* technique was introduced as part of this work as an attempt to address some of the limitations of the standard one. Since apart from the preliminary results shown in Chapter 2, devices exploiting this new proposed QWI technique had never been fabricated, the realised mask contained two kinds of devices, some PMLLs with the standard split contact geometry for gain and absorbing regions, and some FP cavity lasers for basic characterisation. The results obtained from both kinds of devices will be described in the following paragraphs.

5.2.1 *FP lasers*

The FP laser that were fabricated had the contact section not covering the entire length of the device, and had the regions in direct proximity of the cleaving edges thus left unpumped, but intermixed. The distance between the areas that underwent QWI and the pumped section was varied between -40 and 40 µm, with a negative value meaning an overlap between the intermixed area and the p-contact. A schematic of the fabricated pattern is depicted in Figure 5.2a. The total cavity length was 2050 µm corresponding to a mode spacing of $\sim$20.6 GHz while the contact on the gain section was 1750 µm long. By assessing the performance of each of the FP lasers in terms of threshold current density (which should vary depending on the distance from the QWI region) it is possible to extrapolate important information about spatial resolution and gain degradation displayed by the post-etch-QWI technique. Unfortunately, time constraints prevented the fabrication of a large number of samples to be annealed at a different temperatures for an extensive characterisation of the devices behaviour as a function of different bandgap blue-shifts. The target value for the detuning was therefore set to $\sim$15 nm, even though this was less than what deemed optimal in previous experiments [97], especially regarding the operation of the mode-locked devices described in the next paragraph. Given the limited number of fabrication runs available a conservative approach was preferred, in order to avoid a SA whose losses would be too low to effectively trigger pulsed operation. Given the results of the preliminary tests regarding the PL shifts (see Chapter 2) and in light of the considerations regarding the

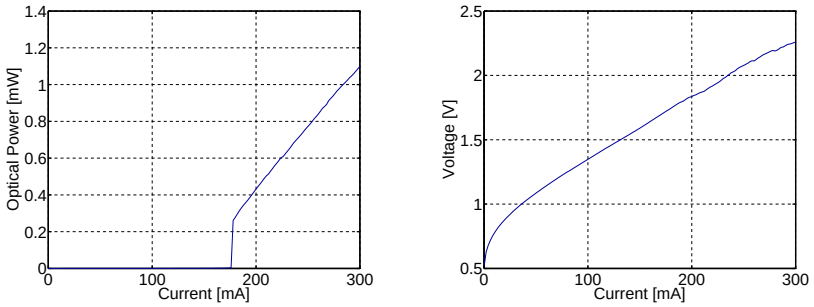

(a) Emitted power vs. injected current. (b) Junction voltage vs. injected current.

Figure 5.1: LI curves for a FP laser with intermixed mirror sections.

achieved bandgap shifts varying between 2 mm test samples and final devices (having size $11x12$ mm) [105], it was decided to anneal the sample for 1 minute at 600°C after the copper-doped silica sputtering and the deposition of the protective PECVD silica layer. The sample showed an effective lift-off of the sputtered layer, confirming once again the robustness of the PMMA quadruple layer recipe targeted for lift-off of sputtered material on non-planar surfaces. The fabrication followed the steps shown in Figure 2.1 for the post-etch-QWI case.

After completion of the devices, the FP lasers characterisation started from the LI curves. For this measurement current was injected in the gain region by means of a single probe. The output power was collected by a broad area power sensor (*ThorLabs S132C*) whose output was read by a digital power meter (*ThorLabs PM100D*). All measurements were made with the sample placed on a copper submount whose temperature was controlled through a TEC module, and kept constant at 20 °C. The LI power and voltage curves for one of the FP lasers are shown in Figure 5.1. All devices showed a lasing threshold averaging 175 mA, suggesting the optical mode was experiencing propagation losses ∼5 times as high compared to standard 3QW PMLLs. The discontinuity in the emitted power at threshold is a clear indication of a highly lossy optical cavity, needing very high pumping before a stable lasing oscillation can be maintained.

The evolution of the threshold current density against the distance of the intermixed section from the gain region is plotted in Figure 5.2b, with no significant changes observed in the threshold current density value; the measured value was on average ∼5 times higher than what typically measured for this material system [6, 107], suggesting a degradation in the gain characteristics of the material. The fact that such gain deterioration does not depend on the distances from the QWI region suggests it is not due to the QWI process itself, but most likely to the high-temperature annealing process happening after dry etch. Despite the sample undergoing RTA at a lower

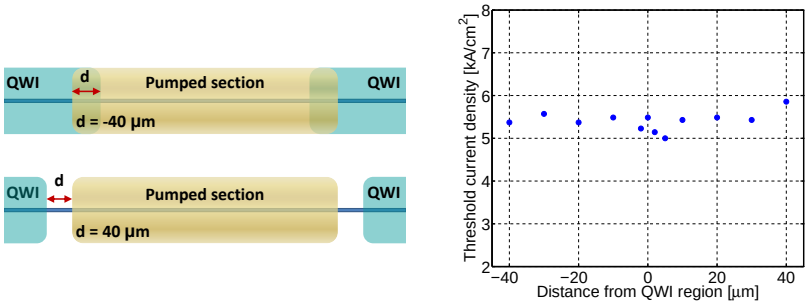

(a) Schematic of the fabricated FP lasers. (b) Threshold current density vs. distance from the intermixed area for the fabricated FP lasers.

Figure 5.2: Schematic of the fabricated pattern and summary of the threshold current density for FP lasers fabricated with the *post-etch*-QWI technique.

temperature with respect to the classic-QWI technique, the fact that the material has already been etched to the top of the MQW layer is likely to increase its sensitivity towards high-temperature processes.

The sample contained also sets of 2 µm waveguides, some completely intermixed and some non-intermixed at all, in order to allow assessing the actual energy bandgap shift obtained on the final sample from the post-etch-QWI process. The spatial resolution of the process was assessed using the same experimental setup described in Chapter 2, Figure 2.18. Comparison between the two wavelength scans (Figure 5.3) shows a bandgap shift of ∼21 nm, slightly larger than what expected at this temperature. The results of Figure 5.3 also suggest that the high losses cannot be ascribed to a lack of blue detuning causing photoelectric absorption, but rather to other effects needing further investigation. Moreover, being the two measured waveguides 50 µmm apart this measurement also confirms the spatial resolution is less than this value, excluding the hypothesis of the whole sample being intermixed as an explanation for the lasers poor performance.

The possible causes to explain a gain deterioration when the post-etch-QWI process is used are: dislocations caused by the introduction of copper atoms [159]; phosphorus desorption during the annealing step hindering the quality of the p-cladding [160]; the p-dopant (Zinc) diffusing to the QWs and precluding lasing operation [161]; and finally, reactions at the interface between the PECVD silica protective layer and the material, affecting the QW region [162–164]. In particular this last phenomenon is believed to be the most likely cause, considering that it is the only one exclusive to the post-etch-QWI technique. In fact, copper is introduced in the material system also when using the classic-QWI technique, the annealing temperature has higher values

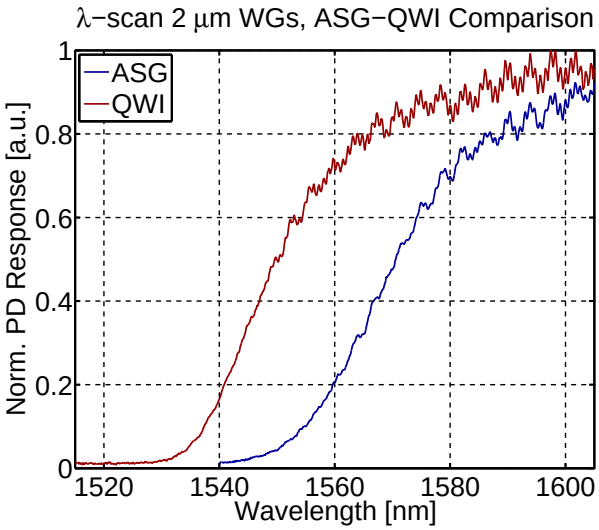

Figure 5.3: Wavelength scan results for QWI and as grown waveguides bandgap. The two traces have been normalised for ease of comparison.

and therefore those devices are bound to be more affected by phosphorous desorption and Zinc diffusion phenomena; instead, as it will be discussed later despite some gain degradation issue the change in threshold for devices fabricated with the classic-QWI technique is not as penalising as what was observed in Figure 5.2b. The explanation for the post-etch-QWI showing bad lasing performance is thought to lie in the chemical reactions happening at the interface between the PECVD silica layer and the material. One of them regards the interaction between the dielectric and the p-cladding, while the remaining two involve the QWs layers. These phenomena can be described by the following chemical formulae:

$$2InP + 4SiO_2 \rightarrow In_2O_3 + P_2O_5 + 4Si \tag{5.1}$$

$$4Al + 3SiO_2 \rightarrow 2Al_2O_3 + 3Si \tag{5.2}$$

$$4Ga + SiO_2 \rightarrow 2Ga_2O + Si \tag{5.3}$$

The first reaction (Equation 5.1) takes place at the interface between the indium phosphide p-cladding and the silica layer (just PECVD in the non-intermixed area or both sputtered and PECVD where QWI is implemented), where it forms indium and phosphorus oxides. This phenomenon is documented in [162], which states it becomes relevant for annealing temperatures higher than 400°C. The fact that causes this reaction to be detrimental for the material system is the free silicon it produces, since silicon, being a IV group element, acts as an

n-dopant and reduces the p-doping of the material top layer. Furthermore, the high temperature RTA could drive diffusion of free silicon atoms towards the QWs causing an n-doping of a region which should remain undoped for good lasing operation. The second and third reaction (Equations 5.2 and 5.3) regard instead the interaction of the atoms of the wells and barriers region with the silica layers above. The considered MQW system is based on Al-quaternary compounds, and the presence of Aluminium and Gallium leads to the formation of their respective oxides [163, 164]; again these phenomena are negligible at temperatures lower than 400°C, but grow exponentially for temperatures above that threshold. Similarly to the first reaction they hinder the material lasing operation through release of free silicon, which laterally diffuses to the waveguide core thanks to the high annealing temperature. All these phenomena arise because of the intermixing phenomenon taking place after the waveguides definition, thus allowing direct contact of the deposited silica with both the indium phosphide top cladding and the QW region before the sample is brought to high temperature. This issue is not present when employing the classic-QWI technique, where both sputtered and PECVD silica are deposited prior to the dry etch process, in direct contact with the InGaAs cap layer.

A chance of improving the performance of this technique could be to replace silica with a different dielectric, both for the sputtering step and the protective layer deposition. One possible candidate is silicon nitride, whose main advantage is the high compatibility with the existing process, since it can be deposited through both sputtering, PECVD and ICP techniques. One of the possible problems with this alternative is the use of another silicon-based dielectric, which could trigger the same phenomena observed with silica at high temperatures, despite reactions similar to those above not being documented so far. Another possibility is the use of magnesium oxide (MgO), which can be deposited by means of sputtering and PECVD techniques [165, 166]. Its wide use as refractory material proves its physical and chemical stability when subject to high temperature RTA steps. Furthermore, similarly to silica it can be easily wet-etched in diluted hydrofluoric acid [167], thus proving good compatibility with the fabrication process already in place. Unfortunately, the implementation of any of the suggested changes would require a complete re-assessment of the QWI recipe, from the sputtering deposition rates to the adequate copper content and annealing temperatures necessary for a certain bandgap shift, and this was incompatible with the time frame assigned to this work. The re-assessment and optimisation of the post-etch QWI will be the object of future work.

5.2.2 *Passively mode-locked lasers*

Despite the FP lasers not showing good lasing performance, the ML performance of the mode-locked devices fabricated on the same chip as the FP lasers was assessed for completeness, also to gain a further insight on the post-etch-QWI dynamics. ML was observed for all devices having a SA section between 0.5 % and 8 % of the cavity length, with the applied reverse voltage spanning from −4.5 V and −1.75 V depending on the length of the SA section. In all cases the generated pulses showed a *coherence spike*, which is when the pulse shape is characterised by a narrow peak atop a broader pedestal of finite duration. Figure 5.4 uses two IAC traces generated from standard PMLLs fabricated on the 3QW material platform (without use of the *post-etch*-QWI technique) to illustrate what pulses unaffected (5.4a) and affected (5.4b) by a *coherence spike* look like.

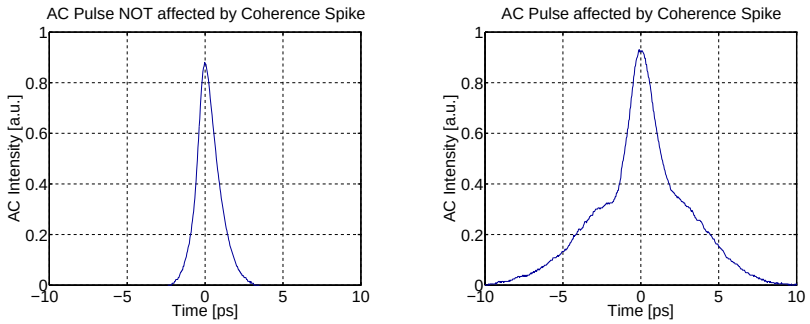

(a) (b)

Figure 5.4: Example of IAC traces showing pulses unaffected (a) and affected (b) by *coherence spikes*.

The presence of coherence spikes on the pulse train is a clear indication of optical emission affected by noise bursts [168–170]. A continuous noise source would in fact give rise to a constant pedestal between consecutive pulses on the IAC, whereas noise bursts oscillating at the cavity round-trip frequency produce a shallow modulation on the pedestal. The presence of coherence spikes suggests incomplete ML, affected from double or satellite pulses and generally having a complex intensity profile. It is often an indication of excessive gain pumping, as it is definitely the case for these post-etch-QWI devices, since the measurements on the FP lasers have shown very high threshold carrier density (5 kA/cm^2), and the threshold obviously increases even more when a reverse biased region is present, e. g. going from 175 mA to 250 mA for a device with a 3.5 % absorber biased at −1.75 V.

The SA lengths providing the best performance for the post-etch-QWI devices are the same that produce the best overall performance for non-intermixed devices (between 2 % and 5 % of the total cavity

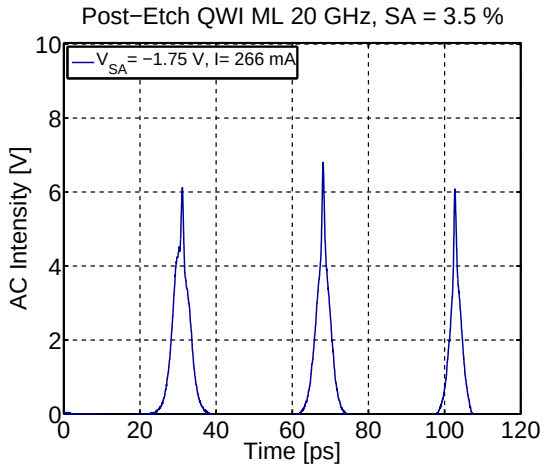

(a) IAC trace.

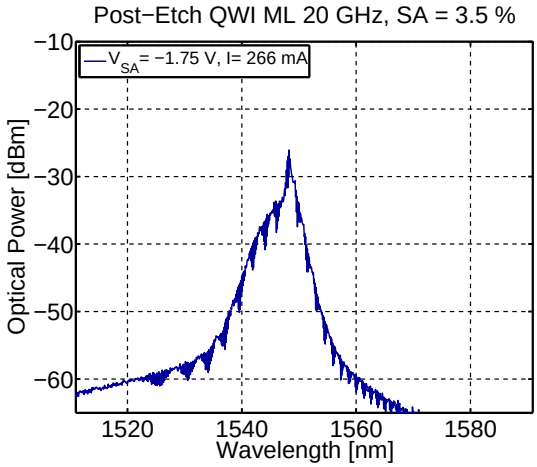

(b) OSA trace.

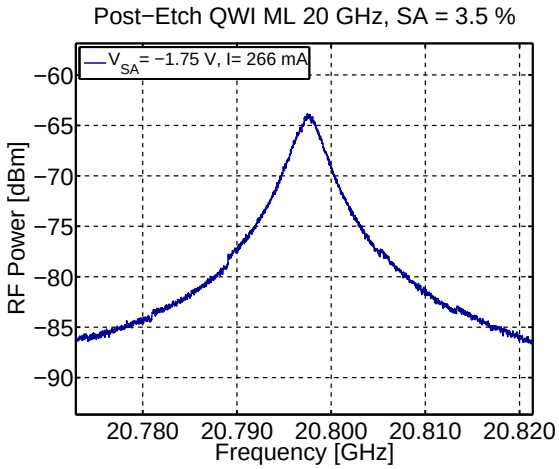

(c) RF trace.

Figure 5.5: IAC, OSA and RF trace for a laser with a 3.5 % intermixed SA section.

length). Between all devices producing optical pulses, the one with a 3.5 % SA length was the least affected by coherence spikes. The IAC trace, the RF trace and the OSA trace for this case are displayed in Figure 5.5. It can be clearly observed from Figure 5.5a that the optical pulses are not free from coherence spikes, with this being more obvious for the first pulse. The poor quality of ML is confirmed also from the OSA trace (Figure 5.5b), where the comb of optical modes displays a very shallow modulation, together with an asymmetry and a narrow-peaked spectral shape. Furthermore, from a zoom of the RF trace (Figure 5.5c), if a Lorentzian shape is assumed for the RF signal, the obtained linewidth at -3 dB has a value of 3 MHz, about three times higher than the best achieved result for PMLLs with non-intermixed SAs. Such a wide RF spectrum agrees with the very high gain pumping (7.5 kA/cm^2) and is yet another indication of phase locking instability. Because of the poor lasing performance exhibited by the post-etch-QWI devices, no extensive characterisation of their ML performance was carried out. The very high current and the consequent considerable amount of Joule heating present in the post-etch-QWI devices caused a red-shift in the emission wavelength at threshold, with all measured devices starting to lase at $\sim$1550 nm, whereas the same non-intermixed FP cavity PMLL would start lasing at $\sim$1530 nm. Operation at high currents induces large photocurrents also on the SA section, causing early electric failure of the absorber and a generally limited lifetime of the laser. Because of the issues previously discussed, the post-etch-QWI technique did not allow to test the effects of a bandgap detuned SA on the devices ML operation. It was therefore decided to fabricate another chip where the bandgap of the absorber was shifted by means of the classic-QWI technique.

5.3 CLASSIC-QWI DEVICES, EXPERIMENTS

The classic-QWI technique was well-established and had been widely used by the Optoelectronics group at the University of Glasgow, though mostly for passive interconnects or phase shifters. Thus the fabricated chip did not include any FP lasers, only PMLLs with the split-contacts geometry were realised. The only characterisation structure added to the designed mask was a spatial resolution test pattern, since a fluctuation in this parameter between repeated fabrication runs was one of the known limitations of this technique.

5.3.1 *Passively mode-locked lasers, basic characterisation*

A set of PMLLs was fabricated with SA section lengths varied between 1 % and 15 % of the total FP cavity length. That was chosen to be 1250 μm in order to produce optical pulses with a repetition rate of $\sim$36 GHz (quasi 40 GHz). The sample contained bars with intermixed

absorbers and bars whose absorbing section was not bandgap shifted. The target bandgap shift for the whole sample was set to ∼15 nm, with the same considerations previously mentioned about the post-etch-QWI case still holding, and this detuning being considered an optimal trade-off. In order to tackle the aforementioned poor reproducibility of the classic-QWI technique, a test sample underwent the copper and silica sputtering alongside the main one, then it was subject to RTA tests and PL measurement to calibrate the required annealing temperature for the targeted shift. As a result of this preliminary test it was decided to anneal the sample for one minute at 660°C after lift-off of the sputtered copper and silica layer and deposition of the protective PECVD silica. Once fabrication of the sample was completed with cleaving and mounting, the first characterisation step was the measurement of the LI curves. These measurements were of significance especially for those bars having intermixed SAs, to check if undergoing the classic-QWI technique had caused significant changes in the lasing threshold. During the LI measurements, only the gain section was probed, while the SA contact was left floating; the temperature was always kept at 20 °C as in the previously described LI experiments. The power and voltage LI curves for devices with SA length varying between 1 % and 15 % are displayed in Figure 5.6.

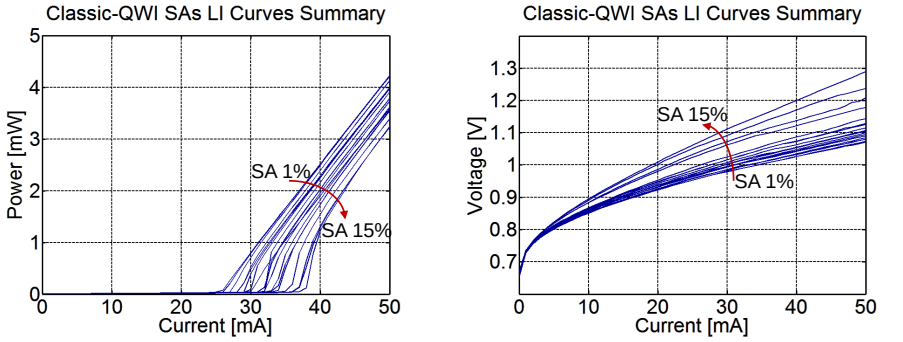

(a) Emitted power vs. injected current.

(b) Junction voltage vs. injected current.

Figure 5.6: LI curves for PMLLs with intermixed SA sections of various lengths, with the absorber left floating. The step in SA length for the displayed family of curves is 1 %.

All devices were found to be lasing with their optical total emitted power (Figure 5.6a) at 50 mA ranging between 4.2 mW and 3.2 mW for the shortest and longest absorbers, respectively. The threshold current varied between 27 mA and 37 mA for the shortest and longest absorbing regions, respectively. The voltage traces (Figure5.6b) were used to determine the series resistance of the devices, which was calculated at 50 mA to be between 21.5 Ω and 26 Ω for increasing SA lengths. These values are quite high considering that non-intermixed PMLLs fabricated on the 3QW material normally exhibit a resistance of only few Ω for the same current value, but this is a known con-

sequence of the classic-QWI process [106]. In fact, the doping level in the heavily doped GaInAs cap layer, designed to improve the electric performance of the devices, is affected by the high annealing temperature and by the introduction of copper, and this translates into an increased device series resistance. It has been shown by several publications how the presence of copper in III-V materials affects their electrical properties, producing p-doped, n-doped or even semi-insulating layers depending on growth and thermal conditions [171–173]. During the QWI fabrication step the gain sections were not covered by copper and sputtered silica but only by the protective PECVD silica, so a copper contribution to the high contact resistance could be ascribed only to copper laterally diffusing or to an insufficient thickness of the layer preventing annealing-induced damage. Copper is thought to have a much higher diffusivity in the heavily doped InGaAs cap layer than in the p-doped indium phosphide cladding, therefore at high temperatures it diffuses laterally in the cap-layer level. A bandgap detuning is therefore induced only in the sputtered zones, but unfortunately the contact resistance degrades everywhere on the sample. Dry etching of the cap layer between the SA and the gain region before the QWI annealing step could provide a solution to this problem, although adding additional lithography and etch steps and increasing fabrication complexity.
Besides characterising the LI response of the bars with intermixed SAs, the actual bandgap shift obtained on the final sample was also checked by using the same experimental setup recalled earlier in this chapter for the assessment of the spatial resolution (Figure 2.18). One of the bars on the sample contained a pattern alternating intermixed and as grown waveguides with a 100 μm spacing as shown in Figure 5.7a.

Figure 5.7 also contains, other than a picture of the spatial resolution test pattern, the response to a scan of the tunable laser wavelengths. Three plots are present, with Figure 5.7b showing the raw data of the voltage output from the photodetector vs. the wavelength scanned. A substantial difference between signal levels for the as grown and intermixed case can be inferred from this trace. Furthermore, from the normalised data in Figure 5.7c one can see there has been a bandgap blue shift in the QWI case, even though this displays a shallower fringe modulation for photon energies below bandedge with respect to the as grown waveguide. The scans have been done sequentially for the as grown and intermixed waveguides without changing any parameter of the setup (CW laser input power, polarisation, detector gain, etc.) and a similar coupling efficiency between them can be assumed. The difference in trace amplitude and modulation depth above bandedge can therefore be ascribed to higher propagation losses for the QWI case. As for the spatial resolution, the PECVD silica protected waveguide not showing

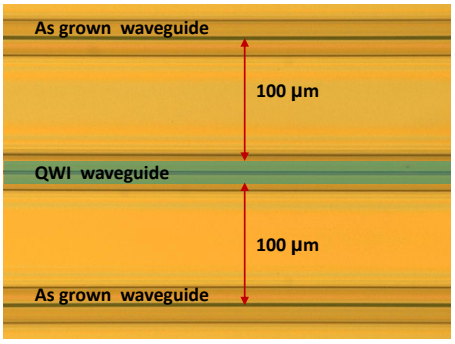

(a) Picture of the QWI spatial resolution test pattern.

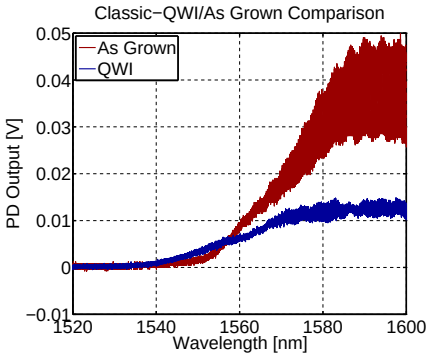

(b) Photodetector output vs. tunable laser wavelength, raw data.

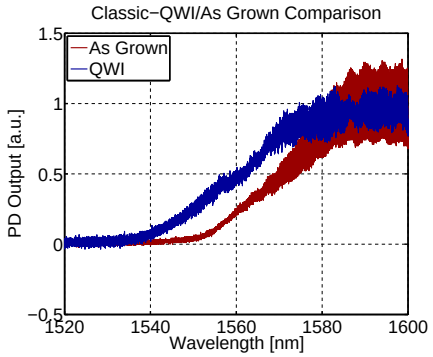

(c) Normalised photodetector output vs. tunable laser wavelength.

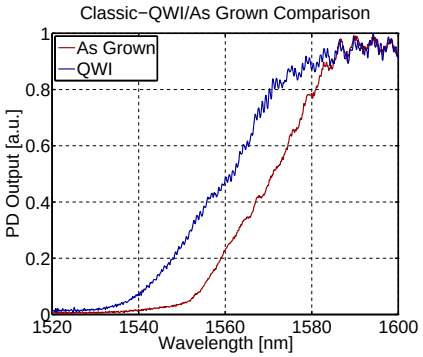

(d) Normalised and low-pass filtered photodetector output vs. tunable laser wavelength.

Figure 5.7: Picture of the QWI spatial resolution test pattern (a), and comparison of energy bandgaps between as grown and classic-QWI waveguides(b,c,d).

any bandgap shift suggests that the spatial resolution of the process is less than 100 µm.

For a clearer assessment of the intermixing level, the normalised bandgap shift data have been low-pass filtered, with the result shown in Figure 5.7d. It can be observed that the obtained energy bandgap shift is ∼10 nm, falling slightly short of the target value of 15 nm. This result is yet another confirmation that the classic-QWI technique only allows an approximate control of the bandgap detuning, particularly when small energy bandgap shifts are required, even with the use of test samples to address the inconsistencies of the technique. It is worth mentioning that while the classic-QWI recipe produced an SA detuning of ∼10 nm after one minute of RTA at 660° C, the post-etch technique discussed in the previous paragraph achieved a shift in excess of ∼20 nm with an annealing temperature of only 600°. This further confirms that the post-etch-QWI technique can provide greater bandgap shifts at lower temperatures if the gain issues are dealt with.

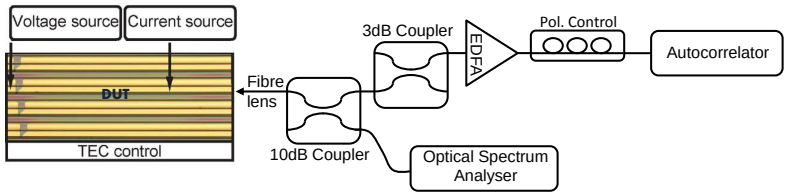

Figure 5.8: Experimental setup used for the characterisation of the classic-QWI devices.

After the preliminary experiments which assessed the basic lasing operation and the spatial resolution, the ML performance of all devices was assessed using the experimental setup shown in Figure 5.8. The lasers were mounted on a copper sub-mount kept at 20°C as for the LI characterisation while two probes were used to inject current and to apply a reverse voltage in the gain and SA sections, respectively. The output from the gain side of the device was collected with a fibre lens and then monitored using the traces from the IAC and the OSA. Before being input to the autocorrelator the pulses were amplified through anErbium-Doped Fibre Amplifier (EDFA) kept at a constant gain throughout the whole experiments. The low dispersion figure of the EDFA (< 35 fs/nm) ensured that there was no broadening of the output pulses, for pulse widths down to 300 fs.

A LabView™ code was used for automating the data collection, in order to simultaneously acquire the traces from the different pieces of equipment and to extensively characterise a great range of currents and voltages. The bar with QWI applied to the SAs was measured first and each device whose absorbing length fell between 1 % and 7 % of the entire cavity displayed pulses for a certain range of gain section currents and negative voltages applied to the SA.

The IAC data were post-processed using MATLAB™ , the FWHM of the pulses was extracted and filled contour plots were used to trace the FWHM evolution with respect to gain section current and SA voltage. The results for SA lengths ranging from 1 % to 7 % are presented in Figure 5.9, with all the colour maps depicting the region where the FWHM of the generated pulses was below 2.5 ps for ease of comparison. The traces from Figure 5.9a to Figure 5.9f immediately show an expansion of the range of voltages and currents providing stable ML with increasing absorbing length. This feature is not dependent on the bandgap shift of the SA but it is characteristic of monolithic passively mode-locked devices; a longer SA will require higher gain pumping for saturation of the losses, and have the shortest recovery time for higher values of reverse voltage. The overall effect of these combined phenomena is an expansion of the stable ML region towards larger currents and SA reverse biases. In fact, the apparent very limited range of SA voltages producing pulses for a 7 % absorbing length

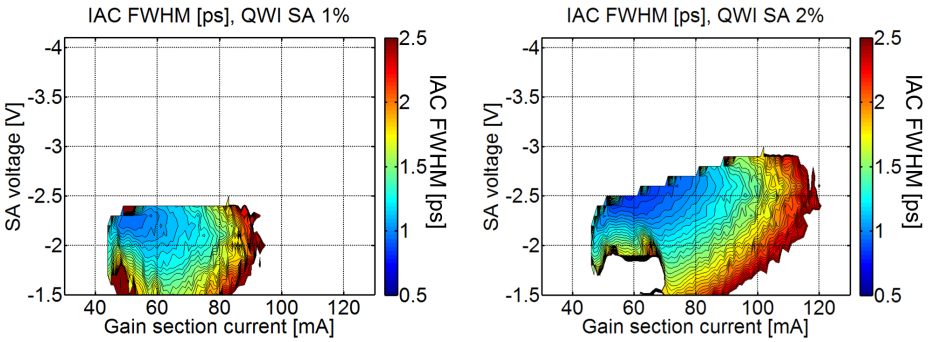

(a) PMLL with intermixed SA, 1 %.

(b) PMLL with intermixed SA, 2 %.

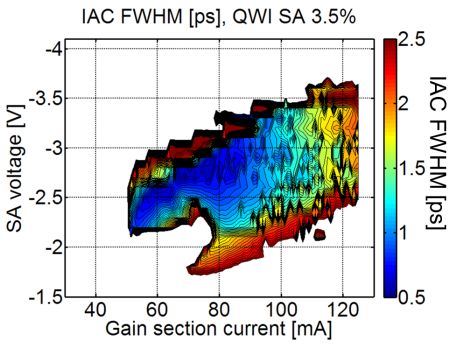

(c) PMLL with intermixed SA, 3.5 %.

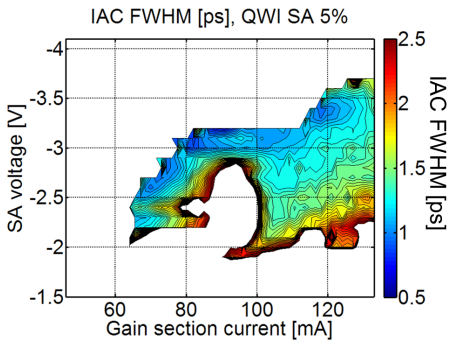

(d) PMLL with intermixed SA, 5 %.

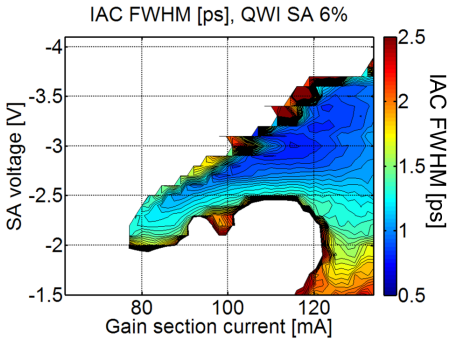

(e) PMLL with intermixed SA, 6 %.

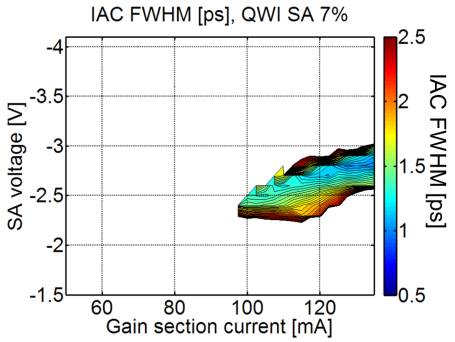

(f) PMLL with intermixed SA, 7 %.

Figure 5.9: Colour maps of the FWHM of the pulses displayed by the IAC for intermixed devices. The upper limit is 2.5 ps

(Figure 5.9f) stems from the ML spanning much higher currents than those scanned. If the range of currents scanned is extended to 350 mA, the range of stable ML proves to cover a much larger interval of currents and voltages, as it will be shown later on in this chapter.
Another feature which is apparent from the colour maps, especially from the 5 % absorber (Figure 5.9d), is the presence of an "*hole*", i.e. a region of parameter space where no pulses were observed, but nearly enclosed by regions where pulses below 2.5 ps were emitted. The region where narrow pulses were not observed is dominated by self-pulsation phenomena [6, 7]. When self-pulsation dominates over ML

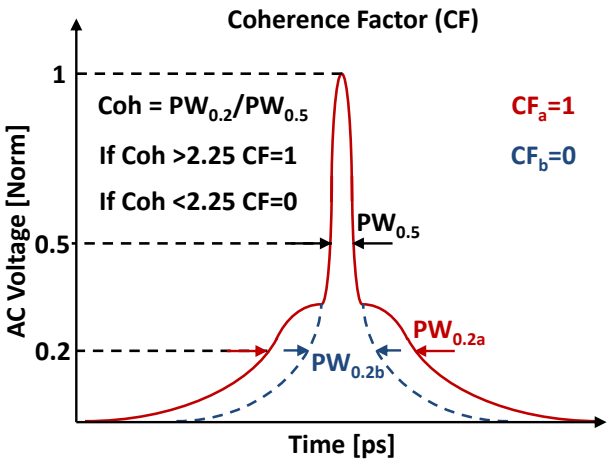

Figure 5.10: Diagram illustrating how the coherence factor is calculated.

the IAC displays a shallow and non pedestal-free modulation at the fundamental repetition rate of the system; the RF displays low frequency components, while the optical spectrum becomes wider but its modulation depth decreases. This regime is an indication of an absorber recovery time being too long or of the gain being insufficient to bleach the SA losses.

Between all tested devices, the PMLL with a 7 % SA was the one that provided the most extensive range of operating conditions producing pulses below 2.5 ps. Other than the pulses FWHM, another quantity can be extracted from the IAC, called the *coherence factor*. This can be calculated by the MATLAB™ routine simply checking if the pulses present a *coherence spike*, which was discussed earlier regarding the post-etch-QWI devices. In order to assess if the measured pulses presented this feature or not, the ratio between the pulse duration at 20 % and 50 % of its peak amplitude was calculated, and if the value obtained was lower than the threshold (set to 2.25) the pulse would be assigned a *coherence factor* value of 0; otherwise it would be classified as affected by coherence-spike and be given a value of 1. A diagram illustrating how the coherence factor is calculated is depicted in Figure 5.10. It is worth mentioning that despite the name, the presence of a coherence spike is not related to the coherence time of the pulses because an IAC measurement is unable to resolve the phase of the pulse train. More complex pulses characterisation techniques would be needed for that, such as the Frequency Resolved Optical Gating (FROG) [174], but their use went beyond the scope of this work.

The coherence factor and the FWHM of the obtained pulses are just two of a number of quantities that was extracted by means of MATLAB™ post-processing to gain a better understanding on how the detuning of the SA affected the ML performance. The following list includes

all the parameters of interest that were extracted from the measured data:

- Temporal FWHM of the pulses displayed by the IAC trace.
- Spectral FWHM of the trace displayed by the OSA.
- Time-Bandwidth Product (TBP) between the FWHMs of IAC and OSA traces.
- Peak power to average power ratio for the obtained IAC trace.
- Peak wavelength of the lasing operation.
- Total output power.
- Peak power of the pulses.
- Coherence factor.

An in-depth analysis of the listed quantities only for the PMLLs having intermixed absorbers would indeed allow a complete assessment of their ML behaviour, but it would not provide any information on how their ML performance compares with standard devices. A thorough comparative characterisation of PMLLs with and without intermixed absorbers was therefore preferred, focussing especially on the device with the longest SA section (7 %) for two reasons: first of all this SA length exhibited the broadest ML range; secondly, given the initial goal of increasing the pulses power, longer absorbing sections were preferred to avoid an excessive induced photocurrent and subsequent SA electric failure. Three kinds of devices were compared, and in the following they will be referred to in brief for fluency:

"COLD" AS GROWN This category refers to PMLLs whose absorbers have not undergone the intermixing process, and fabricated on samples where none of the devices was intermixed; during the fabrication flow these samples have never been brought to temperatures higher than 380°C, that of the ohmic contact annealing.

"HOT" AS GROWN These lasers belonged to samples which experienced high temperatures ($> 650\,^{\circ}\mathrm{C}$) during the fabrication process, despite not having intermixed absorbers.

INTERMIXED Finally, this category simply refers to PMLLs whose SAs have undergone the classic-QWI process.

A comparison of the ML operation for all three kinds of devices allows to establish which changes are due to the detuning of the SA bandgap and which are instead mainly a consequence of the material being annealed at very high temperatures. As mentioned previously, the analysis focussed on three devices having the same percentage

of absorbing length with respect to the entire cavity, always 7 %. The length of the cavity changed slightly between the three devices because of the unavoidable cleaving error with the available tools. However, the ML behaviour of PMLLs has been demonstrated to depend on the ratio between SA and total cavity length rather than on its absolute size [6]. The comparison between devices was therefore judged to be meaningful as long as absorbing lengths constituting the same percentage of the cavity are considered. This was indeed the case, with SAs of 85 μm, 90 μm and 88 μm for the "cold", "hot" and intermixed case respectively, whose bars were 1240 μm, 1275 μm and 1250 μm long, respectively. It is worth mentioning that all the experiments were carried out sequentially for all devices, only realigning the setup to maximise the power coupled to the lensed fibre when a device was swapped with the next one. The lack of changes in the experimental setup guarantees a meaningful comparison between different bars.

5.3.2 *Passively mode-locked lasers, "cold" as grown/QWI comparison*

This section presents an analysis of the results from the comparison between intermixed and "cold" as grown PMLLs. This was particularly significant because "cold" as grown lasers represented the state-of-the-art for monolithic devices fabricated on a MQW material system, thus provided an ideal benchmark for the QWI devices to be compared against.

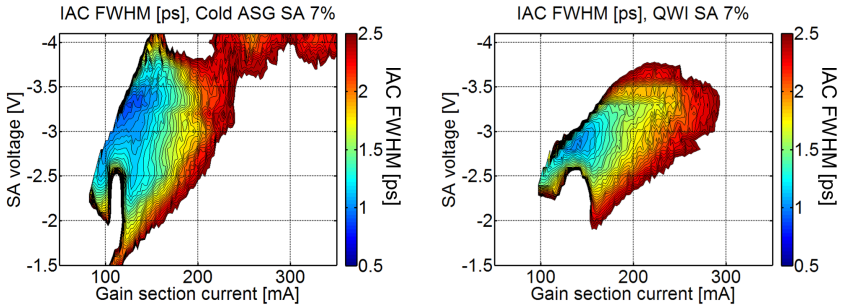

(a) (b)

Figure 5.11: Comparison of pulse FWHM between "cold" as grown and QWI devices. Absorber length is 7 %.

One of the most important quantities for the comparison is the FWHM of the pulses displayed by the IAC, which highlights the differences in current and voltage range providing stable ML. Figure 5.11 compares the FWHM of the pulses between "cold" as grown and QWI case, with the displayed values having an upper limit of 2.5 ps. At a first glance the performance do not differ much, though the ML of the "cold" as grown device extends to slightly higher currents. However,

it must be pointed out that as the ML region shifts to high currents it shifts to higher reverse biases as well, increasing the photocurrent in the SA for a given level of intracavity optical power.

An analysis of the *coherence factor* maps between intermixed and "cold" absorber, depicted in Figure 5.12, shows a larger region of pulses free from coherence spikes for the non-intermixed PMLL. This is not thought to be related to the detuning of the SA, but rather to the high temperature RTA to which the material was subject, causing a degradation of the optical gain. This gain deterioration makes the ML performance more affected by phenomena like self pulsation and noise bursts, translating in a complex intensity profile and a coherence spike on the IAC trace.

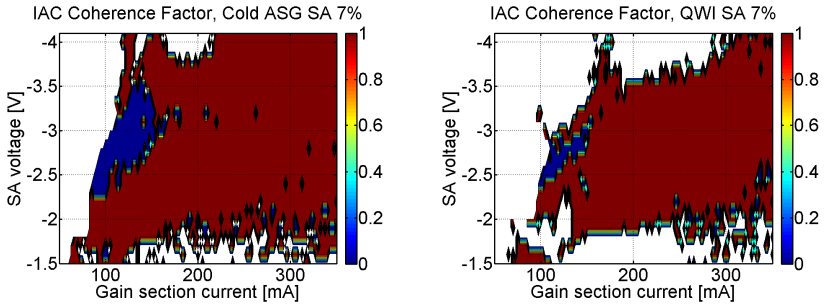

(a) (b)

Figure 5.12: Comparison of pulse *Coherence Factor* between "cold" as grown and QWI devices. Absorber length is 7 %.

Another parameter which was regarded with interest during the characterisation was the peak wavelength of the optical spectrum. The colour maps displaying the peak wavelength of the emission for the range of currents and voltages scanned are shown in Figure 5.13. There were two possible scenarios for the evolution of the device mode-locked operation following a detuning of the SA bandgap towards shorter wavelengths, the first being a shift in the range of voltages providing stable ML; another possibility was a shift in the emission peak wavelength with the lasing operation "following" the absorber bandedge, given the broad gain bandwidth. A comparison between Figure 5.13a and Figure 5.13b indeed shows a blue shift of the peak wavelength, more obvious for higher gain section currents and SA reverse biases.

If the analysis is focussed on currents between 250 and 350 mA, more interesting for comparison since it is where the QWI case outperforms the "cold" as grown in terms of IAC FWHM for absorber voltages between -3.0 V and -3.5 V, the blue shift in the OSA peak wavelength becomes more obvious, as it can be observed in the upper right corner of the colour map. These results seem to suggest there is a change in the emission wavelength of the PMLL when a blue bandgap shift is applied to the SA, even though this needs verification

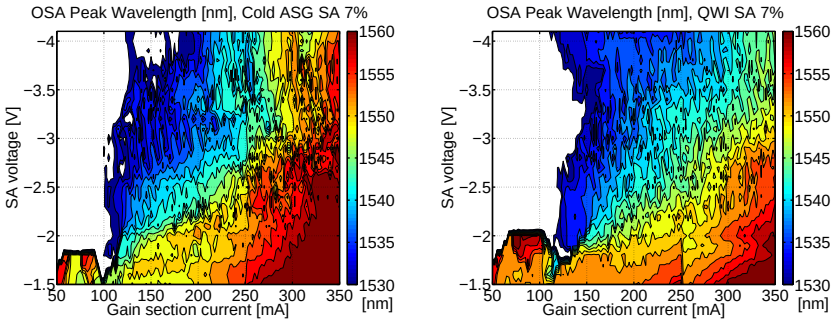

(a) (b)

Figure 5.13: Comparison of OSA peak wavelength between "cold" as grown and QWI devices. Absorber length is 7 %.

and requires further tests on devices with a greater blue shift applied to their absorber.

Another quantity that gives further information on the ML quality is the FWHM of the optical spectrum which, if multiplied with the temporal FWHM of the pulses extracted from the IAC trace, gives the so-called Time-Bandwidth Product (TBP). This quantity is useful in establishing how close a pulse is to its transform limit, which is characterised by the narrowest possible spectrum for a given pulse duration. The TBP of a transform-limited pulse has a value of 0.315 if it is fitted with a sech^2-shaped function, which is the shape that better describes the pulses obtained from a PMLL on the 3QW material platform. The TBP data for the intermixed and "cold" as grown case are compared in Figure 5.14.

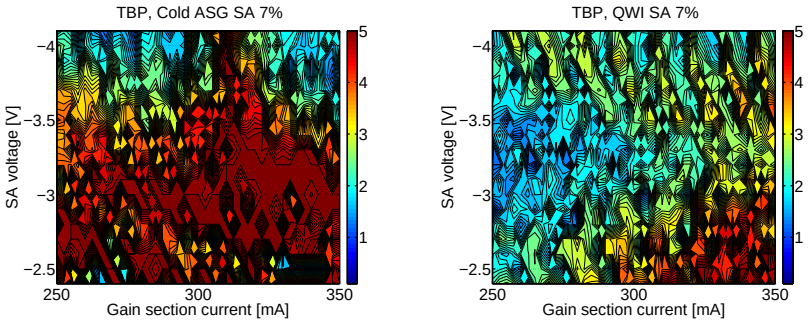

(a) (b)

Figure 5.14: Comparison of TBP between "cold" as grown and QWI devices, for gain section currents spanning between 250 and 350 mA. Absorber length is 7 %.

It is straightforward from a comparison of the diagrams in Figures 5.14a and 5.14b that the QWI device exhibits superior performance in terms of TBP for the considered interval of gain section currents and SA reverse voltages. This is a confirmation that a PMLL with a blue bandgap detuning applied to the SA produces optical pulses

which are less chirped than those emitted from a "cold" as grown device. Both intermixed and "cold" as grown bar are far from being transform limited, but this is in line with what previously obtained for an absorbing region equal to 7 % of the FP cavity length [6].
In view of the initial motivations behind this project, one of the most important quantities to be compared was the peak power of the train of pulses. This was calculated by using the total power extracted from the OSA traces through an integration of the trace, and then normalising the obtained power to the setup losses. These were estimated to be 16 dB, and in order to verify this method provided an accurate evaluation of the total power further LI scans with the broad area detector were compared with the data derived from the measured optical spectrum. The LI curves between 250 and 350 mA and the total power extracted from the OSA trace for the QWI case are shown in Figure 5.15. Good correspondence can be seen between the two plots, both showing for example a power of ∼7 mW for a gain section current of 350 mA and a SA reverse bias of −4.1 V.

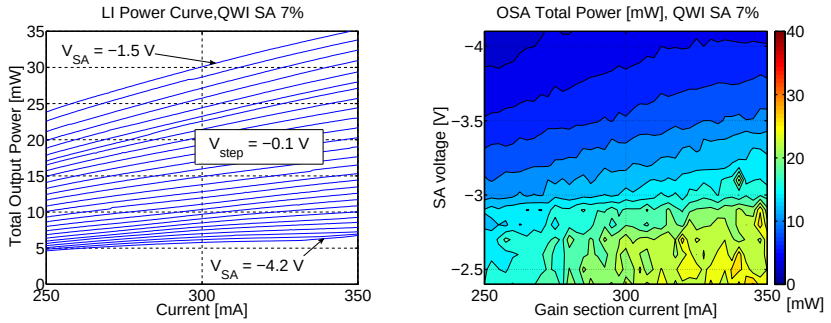

(a) Total power dependence on SA reverse voltage (varied with −0.1 V steps) and gain section current obtained directly from broad area detector.

(b) Total power dependence on SA reverse voltage (varied with −0.1 V steps) and gain section current extracted from OSA trace through post-processing.

Figure 5.15: Comparison between the total power obtained from a broad area detector and extracted from the OSA trace for a QWI device, with 7 % absorbing length.

A summary of the differences between the performance of "cold" as grown intermixed lasers in terms of FWHM of the pulses, peak power and ratio between this and the average power can be inferred from the juxtaposition of the maps shown in Figure 5.16.

Considering a fixed current of 250 mA for ease of comparison, the device having an intermixed absorber displays the best train of pulses (smallest temporal FWHM and highest peak to average ratio for the IAC trace) when a voltage of −3 V is applied to the SA, with a corresponding total output power for this operating point of 10 mW. The "cold" as grown laser instead gives the narrowest pulses for higher reverse biases of the SA, and at −4.1 V on the absorber and 250 mA

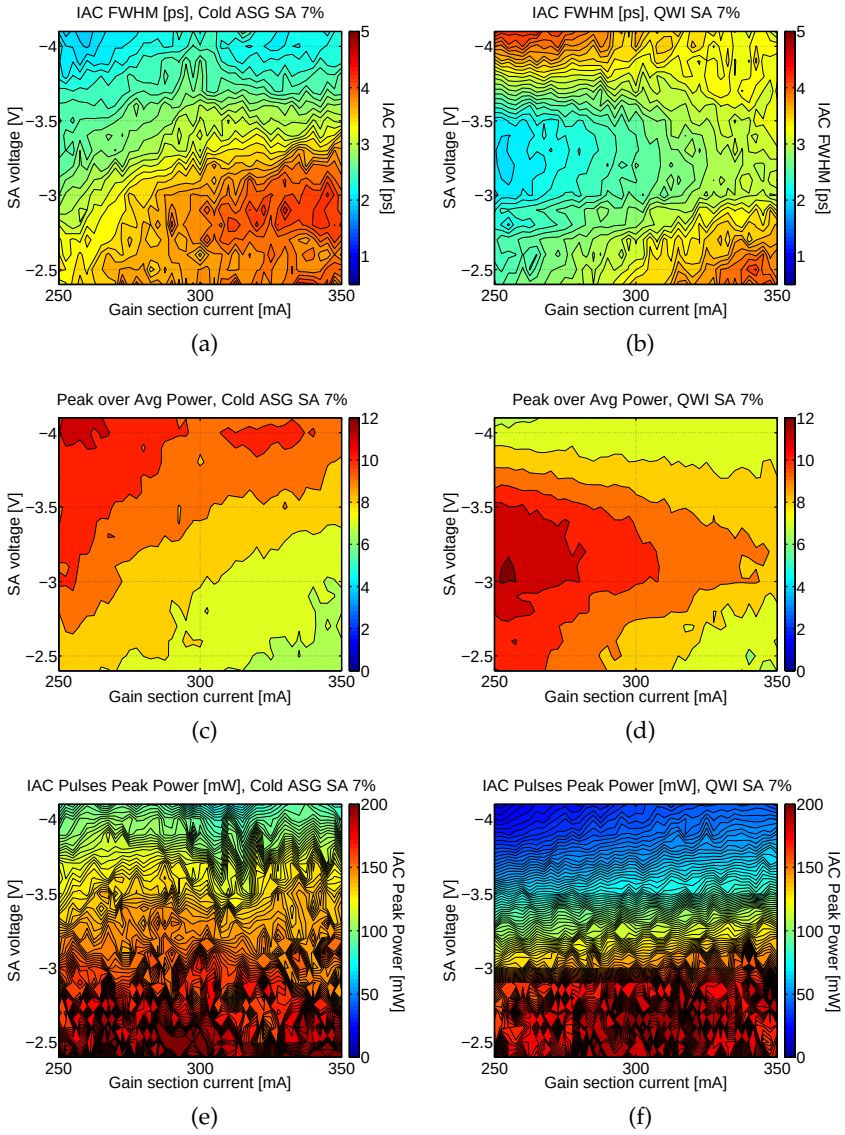

Figure 5.16: Comparison of the FWHM of the IAC pulses, peak to average power ratio and peak power between PMLLs with a "cold" as grown and classic-QWI absorber. Absorber length is 7 %.

in the gain section, the corresponding total output power is 8 mW. Comparing the peak power for the two operating points listed above (Figures 5.16e and 5.16f), this translates into a 20 mW pulse peak power difference, with 100 and 120 mW extrapolated respectively for the "cold" as grown case and the intermixed one. If one is to compare the "cold" as grown with the intermixed one for the same current-voltage pair though, i.e. 250 mA and -3 V, from the diagrams it is immediately clear that the QWI case has a poorer performance.

The difference in peak power performance between the "cold" as grown and QWI can be better explained through a further comparison of the devices in terms of total power. The LI curves for currents

between 0 and 250 mA and reverse voltages applied to the absorber between −1.4 and −4.2 V are compared in Figure 5.17.

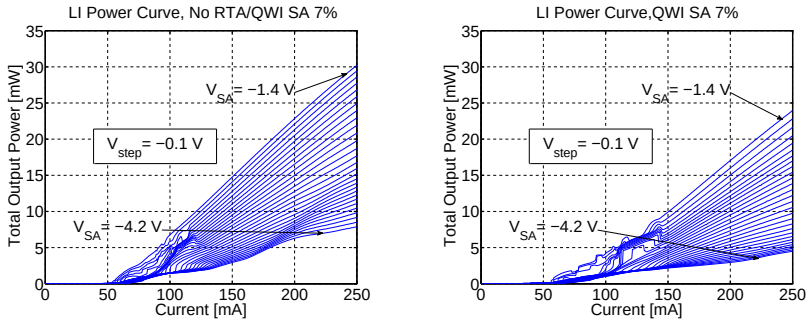

(a) (b)

Figure 5.17: LI curves comparison between "cold" as grown and QWI devices, for gain section currents spanning between 0 and 350 mA. Absorber length is 7 %.

A comparison of Figure 5.17a with Figure 5.17b, which have been plotted on the same vertical scale for ease of comparison, immediately shows that the intermixed PMLL is penalised in terms of total emitted power. This is because of the gain degradation experienced by the 3QW material when subject to high annealing temperatures. It is also the reason behind the fact that despite the device with detuned absorber producing narrower pulses between −3 and −3.5 V (Figure 5.16b), and having a higher ratio between peak power and average power (Figure 5.16d), has a lower peak power than pulses from the "cold" as grown PMLL.

5.3.3 *Passively mode-locked lasers, "hot" as grown/QWI comparison*

The fact that a blue detuning of the absorber can be beneficial to the performance of PMLLs on the 3QW material system is confirmed from a comparison between the "hot" as grown and intermixed cases. This case is more meaningful as both sets of devices suffer from the same degradation of the gain and therefore any changes in the ML performance can be directly ascribed to the SA shift. The fact that both devices suffer from a similar gain deterioration can be seen from a comparison of their power LI curves, shown in Figure 5.18.

The shape of the LI curves showed several differences, the most obvious being a much noisier trace from the "hot" as grown case. This was deemed to be the consequence of the laser being more affected by mode instabilities as the current was increased. However, the most relevant outcome from this comparison was that both sets of devices exhibited a similar performance in terms of maximum emitted optical power, confirming the optical gain was similarly impaired in

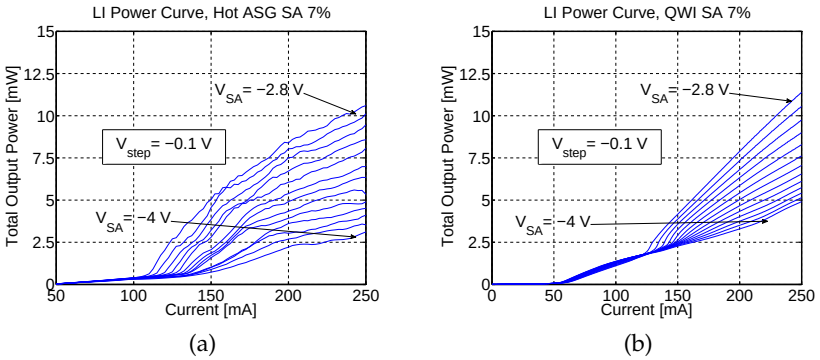

(a) (b)

Figure 5.18: LI curves comparison between "hot" as grown and classic-QWI devices for variying SA reverse biases. Absorber length is 7 %.

both lasers by the high annealing temperature.
As for the ML operation, a clearly superior performance for the QWI device can be inferred from the colour maps depicting the FWHM of the pulses displayed on the IAC trace, shown in Figure 5.19. The maps have been plotted for the same current and voltage intervals, using the same colour scale for ease of comparison. It can be seen that the intermixed device produces pulses under 2.5 ps up to currents nearing 300 mA, whereas for the "hot" as grown PMLL pulses under the 2.5 ps limit only happen for currents up to 215 mA. This confirms that the use of a blue-shifted SA is effective in mitigating the thermal effects which cause the relative detuning between absorber and amplifier section to increase with the current, and which eventually lead to ML ceasing.

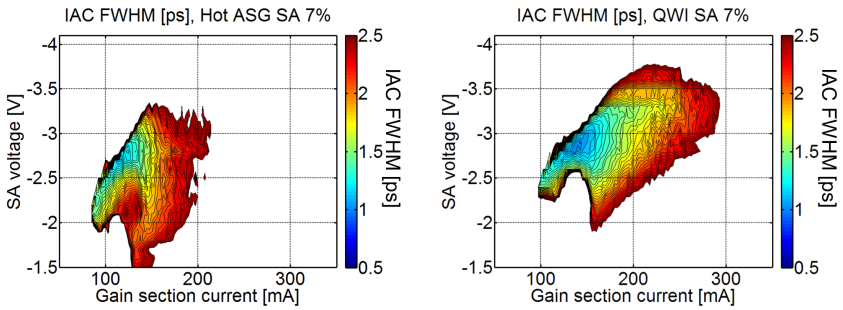

(a) (b)

Figure 5.19: Comparison of pulse FWHM between "hot" as grown and QWI devices. Absorber length is 7 %.

The shortest measured FWHM of the pulses was ∼700 fs for the intermixed case, while 1 ps for the "hot" as grown, with generally shorter pulses emitted from the intermixed PMLL. This suggests a shorter recovery time for the blue-detuned SA, in agreement with a

shallower QW having a lower escape time for the photogenerated carriers.
As for the range of SA voltages providing the narrowest pulse durations, there is a shift of ~ 0.5 V towards more negative reverse biases in the QWI case, in line with expectations as well. It was previously discussed how for a detuned absorber the stable ML region should move to higher reverse biases, since a more transparent SA requires higher reverse voltage to establish the same gain-loss interplay of non-detuned devices. The fact that the ML region shifts towards higher SA reverse biases corroborates this interpretation.

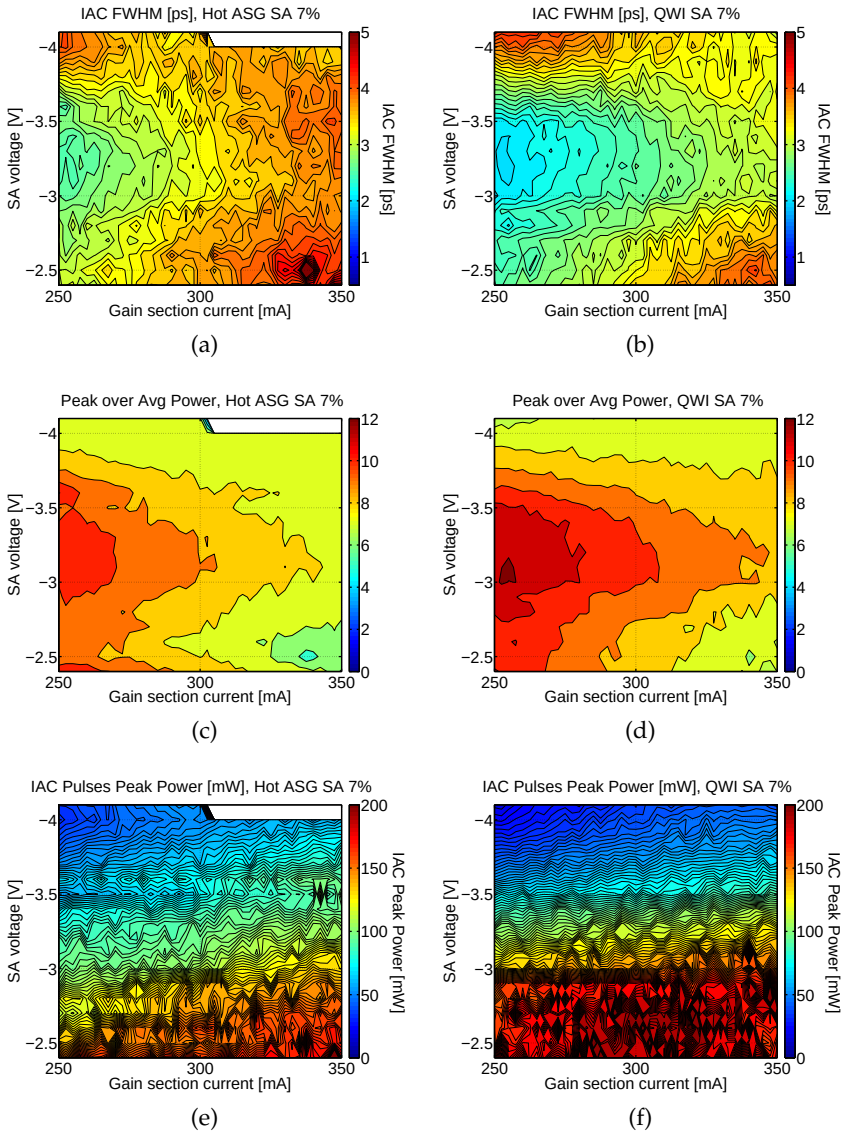

Figure 5.20: Comparison of the FWHM of the IAC pulses, peak to average power ratio and peak power between "hot" as grown and intermixed case. Absorber length is 7 %.

The lasers with intermixed absorbers showed a better performance with respect to the "hot" as grown device, and Figure 5.20 summarises the main results from the comparison. Again the analysis focussed on the current range from 250 to 350 mA, coherently with the previous analysis and also because in this interval the intermixed device most clearly outperforms the "hot" as grown one. This is obvious in terms of FWHM of the produced pulses (Figures 5.20a and 5.20b) and of peak to average power ratio (Figures 5.20c and 5.20d), which mainly retraces the contours of the graph above since both devices have almost identical cavity lengths and thus repetition rates. The similar output power performance between "hot" as grown and intermixed PMLLs together with the fact that the latter emitted narrower pulses caused its peak power performance to be superior with respect of that of the other device (Figures 5.20e and 5.20f).

The maps of the TBP, presented in Figure 5.21, definitely corrob-

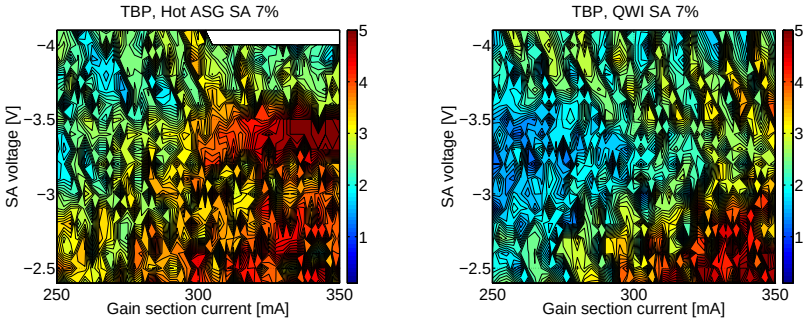

(a) (b)

Figure 5.21: Comparison of pulse TBP between the "hot" as grown and the QWI case. Absorber length is 7 %.

orated the fact that a blue bandgap shift applied to the absorber reduces the chirp experienced by the pulses.

5.4 CONCLUSIONS

In conclusion, the application of a ∼10 nm blue bandgap shift to the absorbing section of a PMLL has proved to be beneficial for ML operation for the following reasons: it has been shown to mitigate the detrimental effect caused by the temperature increase in the SA section, extending the current range where narrow pulses (below 2.5 ps) are emitted by 30 % with respect to the "hot" as grown device. Furthermore, the experimental results suggest a decrease in the SA recovery time, supported by the fact that the shortest pulses obtained with a blue-detuned SA had a FWHM of 700 fs against the best value of 1 ps achieved by the "hot" as grown PMLL. A reduction of 30 % in

the SA recovery time can therefore be estimated. Thanks to the shorter pulses emitted by the QWI device and to the similar levels of total output power between the compared PMLL, the intermixed case provided pulses with a maximum peak power of 215 mW against a 182 mW value from the"hot" as grown device. Furthermore, the application of a blue-detuning to the SA brought a reduction in the amount of optical chirp, with the minimum value of TBP obtained for the QWI case being 0.82, against 1.22 obtained from the "hot" as grown device, a reduction of more than 30 %. Despite the clear improvement in device performance for the intermixed devices with respect to the "hot" as grown ones, the comparison with the "cold" as grown PMLLs has highlighted the need for a technique able to shift the SA bandgap without reducing the material gain. In fact, both the post-etch QWI (which was found to greatly reduce the gain by $\sim$5 times) and the classic QWI (which showed a 20 % reduction in the maximum emitted optical power with respect to "cold" as grown devices) techniques need further optimisation. Moreover, it is believed that a blue-shift greater than 10 nm applied to the SA will show a much clearer change in the device performance, and the individuation of the optimum bandgap blue-shift for the 3QW material system ML performance will be one of the primary future activities.

6 CONCLUSIONS AND FUTURE WORK

6.1 SUMMARY OF THE PROJECT

This thesis explored possible ways of improving the performance of monolithic passively mode-locked lasers, focussing on ways to offer tunability of their repetition rate and to increase their pulses peak power. The starting point was the performance of devices emitting sub-picosecond pulses at a wavelength 1.55 µm and a quasi-40 GHz repetition rate on an aluminium quaternary MQW platform, which had been extensively characterised and whose ML behaviour was well understood. The reason for extending the devices performance towards higher frequencies ($>$ 100 GHz) and powers lies in the constant evolution of optical communication systems towards faster networks, as well as the possible applications to spectroscopy, imaging and sensing.
The first objective of the present work was the investigation of the PMLL behaviour when subject to optical injection from two CW lasers, assessing if such technique could be exploited for generation of optical signals at ultra-high frequency (up to quasi-THz). The usefulness of this approach stems from the fact that no high-speed electronics is required, and moreover tunability from few tens of GHz to quasi-THz is obtained by simply scanning the wavelength of one of the lasers.
The second target of this project was the study of possible ways for improvement of the ML perfomance in monolithic PMLL with regards to the emitted optical power. The research carried out focussed on the development of a new QWI process aimed to address the limitations of the previous one, while also assessing the changes induced to the ML behaviour by a bandgap shift of the SA, obtained by applying the classic-QWI technique.
Both parts of the project proved challenging in terms of fabrication, experimental characterisation and data analysis, but allowed to gain a deep insight into the techniques used.

6.2 MAIN ACHIEVEMENTS

The highlights from this thesis and the main achievements from this work are:

- The successful and discretely tunable locking of monolithic PMLLs with fundamental repetition rate of 36 GHz through ex-

ternal injection of two CW lasers. Optical pulses with repetition rate up to 936 GHz were obtained, with tunability on a 36 GHz grid. This is the first time that pulses from a monolithic mode-locked device are obtained at quasi-THz rate with wide tunability.

- The application of the Vernier effect to integrated SRLs to obtain harmonic ML at very high frequencies, more than THz. On ring cavities whose length ratio was 20/21, pulses at 1.26 THz (corresponding to 20 times 60 GHz, FSR of the mode-locked ring) were obtained, despite with a 70 % pedestal and a residual modulation at the fundamental repetition rate.
- The demonstration of the benefits of a blue-detuning applied to the SA section of a PMLL. A 10 nm bandgap blue-shift applied to the absorber has been shown to induce a 30 % increase in the range of currents providing pulses below 2.5 ps, as well as a 30 % reduction in the losses recovery time and the pulses chirp. The intermixed devices also provided narrower pulses (700 fs against 1 ps) and increased pulse peak power (215 mW against 182 mW).
- The introduction of a new post-etch QWI recipe, which has been shown to reduce by 50 ° on average the RTA temperature needed for a given badngap blue-shift, while also bringing the spatial resolution from few tens of µm to below 5 µm. The newly introduced technique still needs further optimisation, especially regarding degradation of the gain (currently reduced by ∼5 times in post-etch QWI devices).

6.3 FUTURE WORK

As stated previously in the thesis, one of the major goals for the future is the integration of the external injection technique, allowing on-chip generation of signals with ultra-high repetition rate. The possible geometries for monolithic integration were previously discussed, and some preliminary experiments were carried out as proof-of-principle for on-chip generation. The experimental setup used was similar to the one depicted n Figure 3.1, with the exception that the two external CW sources were replaced with two integrated DFB lasers fabricated at the JWNC. This experiment was important to verify if the locking mechanism would still hold with the CW sources not being optically isolated from the injected cavity, and if there was any deterioration or improvement in the quality of the generated signals. The first results showed a behaviour similar to what described in Chapter 3, suggesting that the lack of optical isolation between devices is not an issue. The maximum achievable repetition rate could be somewhat limited by the integrated DFBs tunability. Figure 6.1 shows the IAC and OSA

traces for an optical signal generated at 324 GHz, 9 times the mode-locked cavity FSR. It can be concluded that the route to integration of the devices looks promising, even though an in-depth assessment of the locking mechanism is necessary, for conditions reproducing as much as possible those of an integrated device.

With regards to the intermixing processes, one of the future activit-

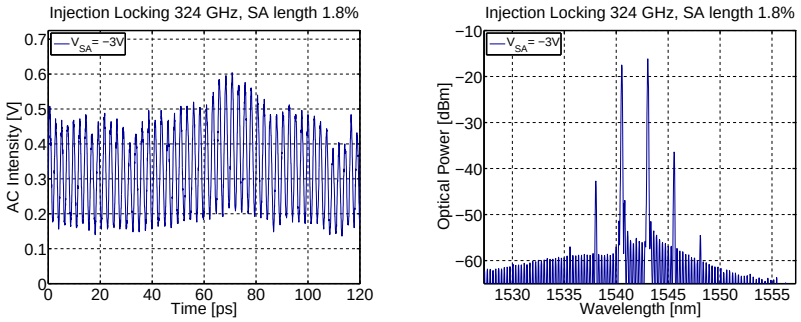

(a) IAC trace. (b) OSA trace.

Figure 6.1: IAC and OSA traces for external injection of monolithic DFB laser into a semiconductor PMLL.

ies is a re-evaluation of the post-etch-QWI technique with the use of a different dielectric protective layer. Furthermore, more PMLLs will be fabricated in the future with different bandgap shifts applied to their absorber, in order to identify the SA detuning which is the most beneficial to the devices mode-locked operation.

Since the experimental results presented in this work suggest that an intermixed SA is characterised by a shorter recovery time, an interesting future activity would be an extensive characterisation of this parameter as a function of the bandgap shift applied to the SA. Furthermore, SAs with faster recovery of the losses should be capable of locking at higher frequencies if the locking technique described in Chapter 3 is applied, therefore other potential future work could be the application of the external injection locking technique to PMLLs with intermixed absorbers.

Finally, based on the results discussed at the end of Chapter 3, it is believed that the maximum achieved repetition rate could be brought beyond 1 THz without being limited by the available gain bandwidth. One of the factors limiting the maximum repetition rate in this work were probably the temperature and current fluctuations experienced by the PMLL, inducing noise which prevented locking at more than quasi-THz frequencies. Another future activity is therefore the improvement of the injection locking setup to make it more robust, in order to bring the repetition rate beyond 1 THz.

BIBLIOGRAPHY

[1] A. C. Bryce. High Power, High Frequency Mode-locked Semiconductor Lasers, Sept. 2007. URL http://gow.epsrc.ac.uk/NGBOViewGrant.aspx?GrantRef=EP/E065112/1. EP/E065112/1.

[2] E. A. Avrutin, J. H. Marsh, and E. L. Portnoi. Monolithic and multi-Gigahertz mode-locked semiconductor lasers: Constructions, experiments, models and applications. *Optoelectronics, IEE Proceedings*, 147(4):251–278, Aug. 2000.

[3] M. Zanola, M. J. Strain, G. Giuliani, and M. Sorel. Post-Growth Fabrication of Multiple Wavelength DFB Laser Arrays With Precise Wavelength Spacing. *Photonics Technology Letters, IEEE*, 24 (12):1063–1065, Jun. 2012.

[4] G. Mezosi, M. J. Strain, S. Furst, Z. Wang, S. Yu, and M. Sorel. Unidirectional Bistability in AlGaInAs Microring and Microdisk Semiconductor Lasers. *Photonics Technology Letters, IEEE*, 21 (2):88–90, Jan. 2009.

[5] L. Hou, P. M. Stolarz, J. Javaloyes, R. P. Green, C. N. Ironside, M. Sorel, and A. C. Bryce. Subpicosecond Pulse Generation at Quasi-40-GHz Using a Passively Mode-Locked AlGaInAs-InP 1.55-µm Strained Quantum-Well Laser. *IEEE Photonics Technology Letters*, 21(23):1731–1733, Dec. 2009. URL http://eprints.gla.ac.uk/34946/.

[6] P. M. Stolarz. *Development of a phase-sensitive pulse measurement technique for semiconductor mode-locked lasers*. PhD thesis, University of Glasgow, 2012. URL http://theses.gla.ac.uk/3368/1/2012stolarzphd.pdf.

[7] P. M. Stolarz, J. Javaloyes, G. Mezosi, L. Hou, C. N. Ironside, M. Sorel, A. C. Bryce, and S. Balle. Spectral Dynamical Behavior in Passively Mode-Locked Semiconductor Lasers. *Photonics Journal, IEEE*, 3(6):1067–1082, Dec. 2011.

[8] K. Yvind, D. Larsson, L. J. Christiansen, C. Angelo, L. K. Oxenlwe, J. Mrk, D. Birkedal, J. M. Hvam, and J. Hanberg. Low-Jitter and High-Power 40-GHz All-Active Mode-Locked Lasers. *Photonics Technology Letters, IEEE*, 16(4):975–977, Apr. 2004.

[9] S. V. Kukarin, S. M. Kobtsev, S. V. Smirnov, and S. K. Turitsyn. Mode-Locked Fibre Lasers with High-Energy Pulses. In K. Jakubczak, editor, *Laser Systems for Applications*, pages 39–58. InTech, New York, 2011. URL http://www-users.aston.ac.uk/~turitssk/InTech.pdf.

[10] S. Lee and University of Central Florida. *High Power Mode-locked Semiconductor Lasers and Their Applications*. University of Central Florida, 2008. ISBN 9780549701767. URL http://books.google.co.uk/books?id=iLVPbxVztIgC.

[11] L. Hou, M. Haji, J. Akbar, B. Qiu, and A. C. Bryce. Low divergence angle and low jitter 40 GHz AlGaInAs/InP 1.55µm mode-locked lasers. *Optics Letters*, 36(6):966–968, Mar. 2011. URL http://eprints.gla.ac.uk/50473/.

[12] J. H. Marsh. Quantum well intermixing. *Semiconductor Science and Technology*, 8(6):1136, Jun. 1993. URL http://stacks.iop.org/0268-1242/8/i=6/a=022.

[13] M. J. Strain, P. M. Stolarz, and M. Sorel. Passively Mode-Locked Lasers with Integrated Chirped Bragg Grating Reflectors. *Quantum Electronics, IEEE Journal of*, 47(4):492–499, Apr. 2011.

[14] W. E. Lamb. Theory of an Optical Maser. *Phys. Rev.*, 134:A1429–A1450, Jun. 1964. doi: 10.1103/PhysRev.134.A1429. URL http://link.aps.org/doi/10.1103/PhysRev.134.A1429.

[15] W. Koechner. *Solid-State Laser Engineering*, chapter Mode Locking. Springer Series in Optical Sciences. Springer, 2006. URL http://books.google.co.uk/books?id=8yM4yF_B72QC.

[16] H. A. Haus. Mode-locking of lasers. *Selected Topics in Quantum Electronics, IEEE Journal of*, 6(6):1173–1185, Nov.-Dec. 2000. URL http://wr.lib.tsinghua.edu.cn/sites/default/files/1174986066162.pdf.

[17] F. X. Kurtner, J. A. der Au, and U. Keller. Mode-Locking with Slow and Fast Saturable Absorbers-What's the Difference? *Selected Topics in Quantum Electronics, IEEE Journal of*, 4(2):159–168, Mar.-Apr. 1998.

[18] H. A. Haus. Theory of mode locking with a fast saturable absorber. *Journal of Applied Physics*, 46(7):3049–3058, Jul. 1975. URL http://link.aip.org/link/?JAP/46/3049/1.

[19] H. A. Haus. Theory of mode locking with a slow saturable absorber. *Quantum Electronics, IEEE Journal of*, 11(9):736–746, Sept. 1975.

[20] R. Paschotta and U. Keller. Passive mode locking with slow saturable absorbers. *Applied Physics B*, 73:653–662, Nov. 2001. URL http://dx.doi.org/10.1007/s003400100726.

[21] C. Harder, J. S. Smith, Y. L. Kam, and A. Yariv. Passive mode locking of buried heterostructure lasers with nonuniform current injection. *Applied Physics Letters*, 42(9):772–774, May 1983.

[22] B. N. Gomatam and A. P. DeFonzo. Theory of hot carrier effects on nonlinear gain in GaAs-GaAlAs lasers and amplifiers. *Quantum Electronics, IEEE Journal of*, 26(10):1689–1704, Oct. 1990.

[23] Y. Nambu and A. Tomita. Spectral hole burning and carrier-heating effect on the transient optical nonlinearity of highly carrier-injected semiconductors. *Quantum Electronics, IEEE Journal of*, 30(9):1981–1994, Sept. 1994.

[24] T. Yilmaz, C. M. DePriest, A. Braun, J. H. Abeles, and P. J. Delfyett. Noise in fundamental and harmonic modelocked semiconductor lasers: experiments and simulations. *Quantum Electronics, IEEE Journal of*, 39(7):838–849, Jul. 2003.

[25] Young-Kai C. and M. C. Wu. Monolithic colliding-pulse modelocked quantum-well lasers. *Quantum Electronics, IEEE Journal of*, 28(10):2176–2185, Oct. 1992.

[26] A. A. Tager. Mode competition and mode locking in compound cavity semiconductor lasers. *Photonics Technology Letters, IEEE*, 6(2):164–166, Feb. 1994.

[27] D. Bitauld, S. Osborne, and S. O'Brien. Passive harmonic modelocking of discrete mode diode lasers. In *Lasers and Electro-Optics Europe (CLEO EUROPE/EQEC), 2011 Conference on and 12th European Quantum Electronics Conference*, May 2011.

[28] Fork R. L., Greene B. I., and Shank C. V. Generation of optical pulses shorter than 0.1 psec by colliding pulse mode locking. *Applied Physics Letters*, 38(9):671–672, May 1981. URL http://link.aip.org/link/?APL/38/671/1.

[29] J. F. Martins-Filho and C. N. Ironside. Multiple colliding pulse mode-locked operation of a semiconductor laser. *Applied Physics Letters*, 65(15):1894–1896, Oct. 1994. URL http://userweb.eng.gla.ac.uk/charles.ironside/CNI65B94.pdf.

[30] J. F. Martins-Filho, E. A. Avrutin, C. N. Ironside, and J. S. Roberts. Monolithic Multiple Colliding Pulse Mode-Locked Quantum-Well Lasers, Experiment and Theory. *Selected Topics in Quantum Electronics, IEEE Journal of*, 1(2):539–551, Jun. 1995.

[31] Y. K. Chen, M. C. Wu, T. Tanbun-Ek, R. A. Logan, and M. A. Chin. Subpicosecond monolithic colliding-pulse modelocked multiple quantum well lasers. *Applied Physics Letters*, 58 (12):1253–1255, Mar. 1991. URL http://nanophotonics.eecs.berkeley.edu/pdf/3296291841uatum%20well%20lasers.pdf.

[32] M. S. Stix and E.P. Ippen. Pulse shaping in passively mode-locked ring dye lasers. *Quantum Electronics, IEEE Journal of*, 19 (4):520–525, Apr. 1983.

[33] L. M. Zhang and J. E. Carroll. Dynamic Response of Colliding-Pulse Mode-Locked Quantum-Well Lasers. *Quantum Electronics, IEEE Journal of*, 31(2):240–243, Feb. 1995.

[34] S. D. Brorson, Z. Wang, T. Franck, S. Bischoff, A. Moller-Larsen, J. M. Nielsen, J. Mork, and M. P. Sorensen. Characterization of Wavelength Chirping in Modelocked Monolithic CPM Lasers. *Photonics Technology Letters, IEEE*, 7(10):1148–1150, Oct. 1995.

[35] S. Bischoff, M. P. Sorensen, J. Mork, S. D. Brorson, T. Franck, J. M. Nielsen, and A. Moller-Larsen. Pulse-shaping mechanism in colliding-pulse mode-locked laser diodes. *Applied Physics Letters*, 67(26):3877–3879, Dec. 1995. URL http://link.aip.org/link/?APL/67/3877/1.

[36] M. Hofmann, S. Bischoff, T. Franck, L. Prip, S. D. Brorson, J. Mork, and K. Frojdh. Chirp of monolithic colliding pulse mode-locked diode lasers. *Applied Physics Letters*, 70(19):2514–2516, May 1997. URL http://link.aip.org/link/?APL/70/2514/1.

[37] L. Hou, M. Haji, C. Li, B. C. Qiu, and A. C. Bryce. 80-GHz AlGaInAs/InP 1.55 µm colliding-pulse mode-locked laser with low divergence angle and timing jitter. *Laser Physics Letters*, 8 (7):535, May 2011. URL http://stacks.iop.org/1612-202X/8/i=7/a=008.

[38] L. Hou, M. Haji, J. Akbar, A. C. Bryce, and J. H. Marsh. Colliding-Pulse Mode-Locked AlGaInAs Laser Operating at 20 GHz with Narrow RF Linewidth. In *Photonics Conference (PHO), 2011 IEEE*, pages 759–760, Oct. 2011.

[39] L. Hou, M. Haji, J. Akbar, A. C. Bryce, and J. H. Marsh. 160-GHz 1.55 µm Colliding-Pulse Mode-locked AlGaInAs/InP Laser With High Power and Low Divergence Angle. *Photonics Technology Letters, IEEE*, 24(12):1057–1059, Jun. 2012.

[40] S. Arahira, S. Oshiba, Y. Matsui, T. Kunii, and Y. Ogawa. 500 GHz optical short pulse generation from a monolithic passively mode-locked distributed bragg reflector laser diode. *Applied Physics Letters*, 64(15):1917–1919, Apr. 1994.

[41] S. Arahira, S. Oshiba, Y. Matsui, T. Kunii, and Y. Ogawa. Terahertz-rate optical pulse generation from a passively mode-locked semiconductor laser diode. *Optics Letters*, 19(11):834–836, Jun. 1994. URL http://ol.osa.org/abstract.cfm?URI=ol-19-11-834.

[42] S. Arahira, Y. Matsui, and Y. Ogawa. Mode-Locking at Very High Repetition Rates More than Terahertz in Passively Mode-Locked Distributed-Bragg-Reflector Laser Diodes. *Quantum Electronics, IEEE Journal of*, 32(7):1211–1224, Jul. 1996.

[43] E. A. Avrutin, J. H. Marsh, J. M. Arnold, T. F. Krauss, H. Pottinger, and R. M. de la Rue. Analysis of harmonic (sub) THz passive mode-locking in monolithic compound cavity Fabry-Perot and ring laser diodes. *Optoelectronics, IEE Proceedings*, 146 (1):55–61, Aug. 1999.

[44] A. A. Tager and K. Petermann. High-Frequency Oscillations and Self-Mode Locking in Short External-Cavity Laser Diodes. *Quantum Electronics, IEEE Journal of*, 30(7):1553–1561, Jul. 1994.

[45] D. A. Yanson, M. W. Street, S. D. McDougall, I. G. Thayne, J. H. Marsh, and E. A. Avrutin. Ultrafast Harmonic Mode-Locking of Monolithic Compound-Cavity Laser Diodes Incorporating Photonic-Bandgap Reflectors. *Quantum Electronics, IEEE Journal of*, 38(1):1–11, Jan. 2002. URL http://eprints.whiterose.ac.uk/656/1/avrutinea1.pdf.

[46] L. Hou, P. Stolarz, R. Dylewicz, M. Haji, J. Javaloyes, Qiu B. C., and A. C. Bryce. 160-GHz Passively Mode-Locked AlGaInAs 1.55 µm Strained Quantum-Well Compound Cavity Laser. *Photonics Technology Letters, IEEE*, 22(10):727–729, May 2010.

[47] J. Patchell, D. Jones, B. Kelly, and J. O'Gorman. Specifying the wavelength and temperature tuning range of a Fabry-Perot laser containing refractive index perturbations (invited paper). *Proceedings of SPIE 5825, Opto-Ireland*, pages 1–13, Jul. 2005. URL http://dx.doi.org/10.1117/12.611334.

[48] R. Phelan, B. Kelly, D. Jones, C. Herbert, J. O'Carroll, M. Rensing, B. Cai, A. Kaszubowska-Anandarajah, P. Perry, J. Stopford, P. Anandarajah, L. P. Barry, and J. O'Gorman. Discrete Mode Laser Diodes with Ultra Narrow Linewidth Emission < 3kHz. In *Optical Fiber Communication Conference and Exposition and The National Fiber Optic Engineers Conference*, page OThK5, Feb. 2008. URL http://www.opticsinfobase.org/abstract.cfm?URI=OFC-2008-OThK5.

[49] B. Kelly, R. Phelan, D. Jones, C. Herbert, J. O'Carroll, M. Rensing, J. Wendelboe, C. B. Watts, A. Kaszubowska, P. P. Anandarajah, C. Guignard, and L. R. Barry. Discrete mode laser diodes with very narrow linewidth emission. *Electronics Letters*, 43(23), Nov. 2007.

[50] S. O'Brien, S. Osborne, D. Bitauld, and A. Amann. Design and applications of discrete mode Fabry-Perot diode lasers. *Photonics and Nanostructures - Fundamentals and Applications*, 8(4):218–227, May 2010. URL http://www.sciencedirect.com/science/article/pii/S1569441010000490.

[51] D. Bitauld, S. Osborne, and S. O'Brien. Passive harmonic mode locking by mode selection in Fabry-Perot diode lasers with patterned effective index. *Optics Letters*, 35(13):2200–2202, Jul. 2010. URL http://ol.osa.org/abstract.cfm?URI=ol-35-13-2200.

[52] S. O'Brien, S. Osborne, D. Bitauld, N. Brandonisio, A. Amann, R. Phelan, B. Kelly, and J. O'Gorman. Optical Synthesis of Terahertz and Millimeter-Wave Frequencies With Discrete Mode Diode Lasers. *Microwave Theory and Techniques, IEEE Transactions on*, 58(11):3083–3087, 2010.

[53] D. Bitauld, S. Osborne, and S. O'Brien. Timing characterization of 100 GHz passively mode-locked discrete mode laser diodes. *Optics Express*, 19(15):13989–13999, Jul. 2011. URL http://www.opticsexpress.org/abstract.cfm?URI=oe-19-15-13989.

[54] M. Bennett, M. F. Schatz, H. Rockwood, and K. Wiesenfeld. Huygens's clocks. *Proceedings of the Royal Society of London. Series A: Mathematical, Physical and Engineering Sciences*, 458(2019):563–579, 2002. URL http://rspa.royalsocietypublishing.org/content/458/2019/563.full.pdf.

[55] R. Adler. A Study of Locking Phenomena in Oscillators. *Proceedings of the IRE*, 34:351–356, Jun. 1946.

[56] H. L. Stover and W. H. Steier. Locking of laser oscillators by light injection. *Applied Physics Letters*, 8(4):91–93, Feb. 1966. URL http://link.aip.org/link/?APL/8/91/1.

[57] V. Annovazzi-Lodi, A. Scire, M. Sorel, and S. Donati. Dynamic Behavior and Locking of a Semiconductor Laser Subjected to External Injection. *Quantum Electronics, IEEE Journal of*, 34(12):2350–2357, Dec. 1998.

[58] R. Lang and K. Kobayashi. External Optical Feedback Effects on Semiconductor Injection Laser Properties. *Quantum Electronics, IEEE Journal of*, 16(3):347–355, Mar. 1980.

[59] M. Margalit, M. Orenstein, and H.A. Haus. Injection Locking of a Passively Mode-Locked Laser. *Quantum Electronics, IEEE Journal of*, 32(1):155–160, Jan. 1996.

[60] E.A. Avrutin and B.M. Russell. Dynamics and Spectra of Monolithic Mode-Locked Laser Diodes Under External Optical Feedback. *Quantum Electronics, IEEE Journal of*, 45(11):1456–1464, Nov. 2009.

[61] B. K. Mathason and P. J. Delfyett. Pulsed Injection Locking Dynamics of Passively Mode-Locked External-Cavity Semiconductor Laser Systems for All-Optical Clock Recovery. *Lightwave Technology, Journal of*, 18(8):1111, Aug. 2000. URL http://jlt.osa.org/abstract.cfm?URI=jlt-18-8-1111.

[62] T. Jung, Shen J-L., D. T. K. Tong, S. Murthy, M.C. Wu, T. Tanbun-Ek, Wang W., R. Lodenkamper, R. Davis, L. J. Lembo, and J. C. Brock. CW Injection Locking of a Mode-Locked Semiconductor Laser as a Local Oscillator Comb for Channelizing Broad-Band RF Signals. *Microwave Theory and Techniques, IEEE Transactions on*, 47(7):1225–1233, Jul. 1999.

[63] Strain M. J. and Sorel M. Post-Growth Fabrication and Characterization of Integrated Chirped Bragg Gratings on GaAs-AlGaAs. *IEEE Photonics Technology Letters*, 18:2566–2568, Dec. 2006. URL http://eprints.gla.ac.uk/14466/.

[64] J. Javaloyes and S. Balle. Detuning and Thermal Effects on the Dynamics of Passively Mode-Locked Quantum-Well Lasers. *Quantum Electronics, IEEE Journal of*, 48(12):1519–1526, Dec. 2012.

[65] D. J. Derickson, R. J. Helkey, A. Mar, J. R. Karin, J. G. Wasserbauer, and J. E. Bowers. Short Pulse Generation Using Multisegment Mode-Locked Semiconductor Lasers. *Quantum Electronics, IEEE Journal of*, 28(10):2186–2202, Oct. 1992.

[66] L. Hou, M. Haji, J. H. Marsh, and A. C. Bryce. 10 GHz AlGaInAs/InP 1.55 μm passively mode-locked laser with low divergence angle and timing jitter. *Optics Express*, 19(26):B75–B80, Dec. 2011. URL http://www.opticsexpress.org/abstract.cfm?URI=oe-19-26-B75.

[67] L. Hou, M. Haji, B. Qiu, J. Akbar, A.C. Bryce, and J.H. Marsh. 10-GHz AlGaInAs/InP 1.55 μm Passively Mode-Locked Laser with Low Divergence Angle and Timing Jitter. *IEEE Photonics Technology Letters*, 23(15):1079–1081, Aug. 2011. URL http://eprints.gla.ac.uk/61251/.

[68] D. J. Jones, L. M. Zhang, J. E. Carroll, and D. D. Marcenac. Dynamics of Monolithic Passively Mode-Locked Semiconductor Lasers. *Quantum Electronics, IEEE Journal of*, 31(6):1051–1058, Jun. 1995.

[69] J. Javaloyes and S. Balle. Anticolliding design for monolithic passively mode-locked semiconductor lasers. *Optics Letters*, 36 (22):4407–4409, Nov. 2011. URL http://ol.osa.org/abstract.cfm?URI=ol-36-22-4407.

[70] A. Thelen. *Design of Optical Interference Coatings*. McGraw-Hill Optical and Electro-Optical Engineering Series. McGraw-Hill, 1989. URL http://books.google.co.uk/books?id=uUqaAAAAIAAJ.

[71] N. Kaiser and H. K. Pulker. *Optical Interference Coatings*. Springer Series in Optical Sciences. Springer, 2010. URL http://books.google.co.uk/books?id=Z1h2cgAACAAJ.

[72] D. Marcuse. Reflection loss of laser mode from tilted end mirror. *Lightwave Technology, Journal of*, 7(2):336–339, Feb. 1989.

[73] A. Mar, R. Helkey, W. X. Zou, D. Bruce Young, and J. E. Bowers. High-power mode-locked semiconductor lasers using flared waveguides. *Applied Physics Letters*, 66(26):3558–3560, Jun. 1995. URL http://link.aip.org/link/?APL/66/3558/1.

[74] S. Gee, G. Alphonse, J. Connolly, and P. J. Delfyett. High-Power Mode-Locked External Cavity Semiconductor Laser Using Inverse Bow-Tie Semiconductor Optical Amplifiers. *Selected Topics in Quantum Electronics, IEEE Journal of*, 4(2):209–215, Mar.-Apr. 1998.

[75] S. Gee, G. Alphonse, C. Barty, J. Connolly, and P. J. Delfyett. Intracavity spectral shaping and Inverse bow-tie semiconductor optical amplifiers for high-power hybrid mode-locked semiconductor lasers. In *Conference on Lasers and Electro-Optics (CLEO) 1998, Proceedings of*, pages 442–443, May 1998.

[76] D. I. Nikitichev, Y. Ding, M. Ruiz, M. Calligaro, N. Michel, M. Krakowski, I. Krestnikov, D. Livshits, M. A. Cataluna, and E. U. Rafailov. High-power passively mode-locked tapered InAs/GaAs quantum-dot lasers. *Applied Physics B*, 103:609–613, Jun. 2011. URL http://dx.doi.org/10.1007/s00340-010-4290-5.

[77] A. Mar, R. Helkey, J. E. Bowers, D. Mehuys, and D. Welch. Mode-Locked Operation of a Master Oscillator Power Amplifier. In *Lasers and Electro-Optics Society Annual Meeting, 1993. LEOS '93 Conference Proceedings, IEEE*, pages 290–291, Nov. 1993.

[78] J. Akbar, L. Hou, M. Haji, M. J. Strain, J. H. Marsh, A. C. Bryce, and A. E. Kelly. High power (130 mW) 40 GHz 1.55 µm mode-locked distributed Bragg reflector lasers with integrated optical amplifiers. *Optics Letters*, 37(3):344–346, Feb. 2012. URL http://ol.osa.org/abstract.cfm?URI=ol-37-3-344.

[79] J. Akbar, L. Hou, M. Haji, M. J. Strain, J. H. Marsh, A. C. Bryce, and A. E. Kelly. High-Power AlGaInAs Mode-Locked DBR Laser With Integrated Tapered Optical Amplifier. *Photonics Technology Letters, IEEE*, 25(3):253–256, Feb. 2013.

[80] J. R. Marciante and G. P. Agrawal. Spatio-Temporal Characteristics of Filamentation in Broad-Area Semiconductor Lasers. *Quantum Electronics, IEEE Journal of*, 33(7):1174–1179, Jul. 1997. URL http://www.optics.rochester.edu/workgroups/marciante/pdfs/1997-07_---_spatiotemp_char.pdf.

[81] A. S. Logginov and K. I. Plisov. On the stability of lateral self-mode locking in an injection laser. *Quantum Electronics*, 34(9):833, Sept. 2004. URL http://stacks.iop.org/1063-7818/34/i=9/a=A12.

[82] J. Martín-Regalado, G. H. M. van Tartwijk, S. Balle, and M. San Miguel. Mode control and pattern stabilization in broad-area lasers by optical feedback. *Physical Review A*, 54:5386–5393, Dec. 1996. URL http://link.aps.org/doi/10.1103/PhysRevA.54.5386.

[83] L. E. Adams, E. S. Kintzer, M. Ramaswamy, J. G. Fujimoto, U. Keller, and M. T. Asom. Mode locking of a broad-area semiconductor laser with a multiple-quantum-well saturable absorber. *Optics Letters*, 18(22):1940–1942, Nov. 1993. URL http://ol.osa.org/abstract.cfm?URI=ol-18-22-1940.

[84] J. Kaiser, I. Fischer, W. Elsasser, E. Gehrig, and O. Hess. Mode-Locking in Broad-Area Semiconductor Lasers Enhanced by Picosecond-Pulse Injection. *Selected Topics in Quantum Electronics, IEEE Journal of*, 10(5):968–973, Sept.-Oct 2004. URL http://epubs.surrey.ac.uk/296/1/fulltext.pdf.

[85] J. Kaiser, I. Fischer, and W. Elsasser. Mode locking of lateral modes in broad-area semiconductor lasers by subharmonic optical pulse injection. *Applied Physics Letters*, 88(10):101–110, Mar. 2006. URL http://link.aip.org/link/?APL/88/101110/1.

[86] G. A. Evans and J. M. Hammer. *Surface emitting semiconductor lasers and arrays*, chapter External Methods of Phase Locking and Coherent Beam Addition of Diode Lasers. Series on Quantum electronics–principles and applications. Academic Press, 1993. URL http://books.google.co.uk/books?id=neRRAAAAMAAJ.

[87] L. J. Mawst, D. Botez, C. Zmudzinski, M. Jansen, C. Tu, T. J. Roth, and J. Yun. Resonant self-aligned-stripe antiguided diode laser array. *Applied Physics Letters*, 60(6):668–670, Feb. 1992. URL http://link.aip.org/link/?APL/60/668/1.

[88] R. K. Huang, L. J. Missaggia, J. P. Donnelly, C. T. Harris, and G. W. Turner. High-Brightness Slab-Coupled Optical Waveguide Laser Arrays. *Photonics Technology Letters, IEEE*, 17(5): 959–961, May 2005.

[89] R. K. Huang, B. Chann, L. J. Missaggia, S. J. Augst, R. B. Swint, J. P. Donnelly, A. Sanchez-Rubio, and G. W. Turner. High-Power Coherent Beam Combination of Semiconductor Laser Arrays. In *Lasers and Electro-Optics, 2008 and 2008 Conference on Quantum Electronics and Laser Science. CLEO/QELS 2008, Conference on*, pages 1–2, May 2008.

[90] J. H. Zarrabi, E. L. Portnoi, and A. V. Chelnokov. Passive mode locking of a multistripe single quantum well GaAs laser diode with an intracavity saturable absorber. *Applied Physics Letters*, 59(13):1526–1528, Sept. 1991.

[91] J. J. Plant, J. T. Gopinath, B. Chann, D. J. Ripin, R. K. Huang, and P. W. Juodawlkis. 250 mW, 1.5 µm monolithic passively mode-locked slab-coupled optical waveguide laser. *Optics Letters*, 31 (2):223–225, Jan. 2006. URL http://ol.osa.org/abstract.cfm?URI=ol-31-2-223.

[92] J.T. Gopinath, J.J. Plant, B. Chann, R.K. Huang, C. Harris, L. Missaggia, J. P. Donnelly, P. W. Juodawlkis, and D. J. Ripin. High Power Monolithic Passively Mode-Locked Slab-Coupled Optical Waveguide Lasers. In *Lasers and Electro-Optics, 2006 and 2006 Quantum Electronics and Laser Science Conference. CLEO/QELS 2006. Conference on*, pages 1–2, May 2006.

[93] F. R. Ahmad and F. Rana. Passively Mode-Locked High-Power (210 mW) Semiconductor Lasers at 1.55 µm Wavelength. *Photonics Technology Letters, IEEE*, 20(3):190–192, Feb. 2008.

[94] Y. L. Chang, I. Tan, C. Reaves, J. Merz, E. Hu, S. DenBaars, A. Frova, V. Emiliani, and B. Bonanni. Passivation of InGaAs/InP surface quantum wells by ion-gun hydrogenation. *Applied Physics Letters*, 64(20):2658–2660, May 1994.

[95] V.I. Tolstikhin, A. Densmore, K. Pimenov, and S. LaFramboise. Single-Mode Vertical Integration of p-i-n Photodetectors with Optical Waveguides for Monitoring in WDM Transmission Systems. *Photonics Technology Letters, IEEE*, 15(6):843–845, Jun. 2003.

[96] T. Sasaki and M. Yamaguchi. Narrow-Stripe Selective MOVPE for High-Quality InGaAsP MQWS and its Application to Photonic Integrated Circuits. In *Indium Phosphide and Related Materials, 1998 International Conference on*, pages 353–356, May 1998.

[97] D. Kunimatsu, S. Arahira, Y. Kato, and Y. Ogawa. Passively Mode-Locked Laser Diodes with Bandgap-Wavelength Detuned Saturable Absorbers. *Photonics Technology Letters, IEEE*, 11(11):1363–1365, Nov. 1999.

[98] Y. Barbarin, E.A.J.M. Bente, T. de Vries, J.H. den Besten, P.J. van Veldhoven, M.J.H. Sander-Jochem, E. Smallbrugge, F.W.M. van Otten, E.J. Geluk, M.J.R. Heck, X.J.M. Leijtens, J.G.M. van der Tol, F. Karouta, Y. S. Oei, R. Notzel, and M. K. Smit. Butt-Joint Interfaces in InP/InGaAsP Waveguides with Very Low Reflectivity and Low Loss. In *Proceedings of the 10th Annual Symposium IEEE/LEOS Benelux Chapter*, pages 89–93, Dec. 2005. URL http://alexandria.tue.nl/repository/articles/598830.pdf.

[99] R. Scollo, H.-J. Lohe, J. F. Holzman, F. Robin, H. Jäckel, D. Erni, W. Vogt, and E. Gini. Mode-locked laser diode with an ultrafast integrated uni-traveling carrier saturable absorber. *Optics Letters*, 30(20):2808–2810, Oct. 2005. URL http://ol.osa.org/abstract.cfm?URI=ol-30-20-2808.

[100] B. S. Ooi, S. G. Ayling, A. C. Bryce, and J. H. Marsh. Fabrication of Multiple Wavelength Lasers in GaAs-AlGaAs Structures Using a One-Step Spatially Controlled Quantum-Well Intermixing Technique. *Photonics Technology Letters, IEEE*, 7(9):944–946, Sept. 1995.

[101] B. S. Ooi, K. McIlvaney, M. W. Street, A. S. Helmy, S. G. Ayling, A. C. Bryce, J. H. Marsh, and J. S. Roberts. Selective Quantum-Well Intermixing in GaAs-AlGaAs Structures Using Impurity-Free Vacancy Diffusion. *Quantum Electronics, IEEE Journal of*, 33 (10):1784–1793, Oct. 1997.

[102] J. H. Teng, S. J. Chua, Y. H. Huang, G. Li, Z. H. Zhang, A. S. Helmy, and J. H. Marsh. Multi-wavelength lasers fabricated by an Al layer controlled quantum well intermixing technology. *Journal of Applied Physics*, 88(6):3458–3462, Sept. 2000. URL http://link.aip.org/link/?JAP/88/3458/1.

[103] N. Holonyak. Impurity-Induced Layer Disordering of Quantum-Well Heterostructures: Discovery and Prospects. *Selected Topics in Quantum Electronics, IEEE Journal of*, 4(4):584–594, Jul. 1998.

[104] L. Fu, P. Lever, P. L. Gareso, M. Buda, H.H. Tan, C. Jagadish, P. Reece, and M. Gal. Impurity-Free Vacancy Disordering of Quantum Wells and Quantum Dots for Optoelectronic/-Photonic Integrated Circuits. In *Semiconducting and Insulating Materials, 2004. SIMC-XIII-2004. 13th International Conference on*, pages 107–112, Sept. 2005.

[105] S. Furst. *Monolithic integration of semiconductor ring lasers*. PhD thesis, University of Glasgow, 2008. URL http://theses.gla.ac.uk/447/2/2008furstphd.pdf.

[106] S. McMaster. *Monolithically integrated mode-locked ring lasers and Mach-Zehnder interferometers in AlGaInAs*. PhD thesis, University of Glasgow, 2010. URL http://theses.gla.ac.uk/1831/1/2010mcmasterphd.pdf.

[107] G. Mezosi. *Semiconductor ring lasers for all-optical signal processing*. PhD thesis, University of Glasgow, 2010. URL http://theses.gla.ac.uk/2349/1/2010Mezosiphd.pdf.

[108] Yiyong Tan, Rongchun Zhou, Haixia Zhang, Guizhang Lu, and Zhihong Li. Modeling and simulation of the lag effect in a deep reactive ion etching process. *Journal of Micromechanics and Microengineering*, 16(12):2570–2575, Dec. 2006. URL http://stacks.iop.org/0960-1317/16/i=12/a=008.

[109] M. J. Loboda, C. M. Grove, and R. F. Schneider. Properties of a–SiO_x:H Thin Films Deposited from Hydrogen Silsesquioxane Resins. *Journal of The Electrochemical Society*, 145(8):2861–2866, Aug. 1998. doi: 10.1149/1.1838726. URL http://jes.ecsdl.org/content/145/8/2861.full.pdf.

[110] H. Namatsu, T. Yamaguchi, M. Nagase, K. Yamazaki, and K. Kurihara. Nano-patterning of a hydrogen silsesquioxane resist with reduced linewidth fluctuations. *Microelectronic Engineering*, 41-42(0):331–334, Mar. 1998. URL http://www.sciencedirect.com/science/article/pii/S0167931798000768. International Conference on Micro- and Nanofabrication.

[111] G. T. Edwards, A. Sobiesierski, D. I. Westwood, and P. M. Smowton. Fabrication of high-aspect-ratio, sub-micron gratings in AlGaInP/GaAs laser structures using a $BCl3/Cl_2/Ar$ inductively coupled plasma.

[112] Lee Chee-Wei and Chin Mee-Koy. Room-Temperature Inductively Coupled Plasma Etching of InP Using Cl_2/N_2 and $Cl_2/CH_4/H_2$. *Chinese Physics Letters*, 23(4):903, Apr. 2006. URL http://stacks.iop.org/0256-307X/23/i=4/a=039.

[113] K. Kennedy, K. M. Groom, and R. A. Hogg. Fabrication of v-groove gratings in InP by inductively coupled plasma etching with $SiCl_4$/Ar. *Semiconductor Science and Technology*, 21(1):L1, Jan. 2006. URL http://stacks.iop.org/0268-1242/21/i=1/a=L01.

[114] P. Strasser, R. Wuest, F. Robin, D. Erni, and H. Jackel. Process Optimization for Dry Etching of InP-InGaAsP-Based Photonic Crystals with a $Cl_2/CH_4/H_2$ Mixture on an ICP-RIE. In *Indium Phosphide and Related Materials, 2004. 16th IPRM. 2004 International Conference on*, pages 175–178, May-Jun. 2004.

[115] R. Grover, J. V. Hryniewicz, O. King, and V. Van. Deep dry etching of InP with Ti-SiO2 bi-level mask in methane-hydrogen-argon for photonics applications. In *Integrated Photonics Research*, page IWB4. Optical Society of America, Jun. 2001. URL http://www.opticsinfobase.org/abstract.cfm?URI=IPR-2001-IWB4.

[116] T. R. Hayes, M. A. Dreisbach, P. M. Thomas, W. C. Dautremont-Smith, and L. A. Heimbrook. Reactive ion etching of InP using CH_4/H_2 mixtures: Mechanisms of etching and anisotropy. *Journal of Vacuum Science & Technology B: Microelectronics and Nanometer Structures*, 7(5):1130–1140, Sept. 1989. URL http://link.aip.org/link/?JVB/7/1130/1.

[117] J. E. Schramm, D. I. Babic, E. L. Hu, J. E. Bowers, and J. L. Merz. Fabrication of high-aspect-ratio InP-based vertical-cavity laser mirrors using $CH_4/H_2/O_2$/Ar reactive ion etching. *Journal of Vacuum Science & Technology B: Microelectronics and Nanometer Structures*, 15(6):2031–2036, Nov.-Dec. 1997.

[118] K. Shinoda, K. Nakahara, and H. Uchiyama. InGaAlAs/InP Ridge-Waveguide Lasers Fabricated by Highly Selective Dry Etching in $CH_4/H_2/O_2$ Plasma. In *Indium Phosphide and Related Materials, 2003. International Conference on*, pages 550–553, May 2003.

[119] O. P. Kowalski, C. J. Hamilton, S. D. McDougall, J. H. Marsh, A. C. Bryce, R. M. De La Rue, B. Vogele, C. R. Stanley, C. C. Button, and J. S. Roberts. A universal damage induced technique for quantum well intermixing. *Applied Physics Letters*, 72(5):581–583, Feb. 1998. URL http://link.aip.org/link/?APL/72/581/1.

[120] C. M. Syktich, G. A. Vincent, and K. A. Scheibert. Hydrogen silsesquioxane resin coating composition, Apr. 1997. URL http://www.patentlens.net/patentlens/patent/US_5618878/en/.

[121] L. Shi, J. M. Sun, X. P. Wang, X. Y. Su, and T. X. Cai. High Activity and Selectivity of Cu/SiO_2 Catalyst for the Direct Synthesis of Indole. *Chinese Chemical Letters*, 13 (3):211–212. URL http://www.imm.ac.cn/journal/ccl/1303/1303009-211-01-381-p2.pdf.

[122] V. Hongpinyo, Y. H. Ding, C. E. Dimas, Y. Wang, B. S. Ooi, W. Qiu, L. L. Goddard, E. M. Behymer, G. D. Cole, and T. C. Bond. Intermixing of InGaAs/GaAs Quantum Well Using Multiple Cycles Annealing. In *PhotonicsGlobal@Singapore, 2008. IPGC 2008. IEEE*, pages 1–3, Dec. 2008. URL https://e-reports-ext.llnl.gov/pdf/362306.pdf.

[123] L. E. Ocola and A. Stein. Effect of cold development on improvement in electron-beam nanopatterning resolution and line roughness. *Journal of Vacuum Science & Technology B*, 24(6): 3061–3065, Nov.-Dec. 2006. URL http://scitation.aip.org/content/avs/journal/jvstb/24/6/10.1116/1.2366698.

[124] A.M. Fox, D.A.B. Miller, G. Livescu, J.E. Cunningham, and William Y. Jan. Quantum Well Carrier Sweep Out: Relation to Electroabsorption and Exciton Saturation. *Quantum Electronics, IEEE Journal of*, 27(10):2281–2295, Oct. 1991.

[125] A. McKee, C. J. McLean, G. Lullo, A.C. Bryce, R.M. De La Rue, J.H. Marsh, and C.C. Button. Monolithic Integration in InGaAs-InGaAsP Multiple-Quantum-Well Structures Using Laser Intermixing. *Quantum Electronics, IEEE Journal of*, 33(1):45–55, Jan. 1997. URL http://www.intenseltd.com/downloads/papers/25.pdf.

[126] F. Devaux, E. Bigan, A. Ougazzaden, B. Pierre, F. Huet, M. Carre, and A. Carenco. InGaAsP/InGaAsP Multiple-Quantum-Well Modulator with Improved Saturation Intensity and Bandwidth Over 20 GHz. *Photonics Technology Letters, IEEE*, 4(7):720–723, Jul. 1992.

[127] Y. Liu, H. F. Chen, J. M. Liu, P. Davis, and T. Aida. Communication Using Synchronization of Optical-Feedback-Induced Chaos in Semiconductor Lasers. *IEEE Transactions on Circuits & Systems Part I: Fundamental Theory & Applications*, 48(12):1484–1490, Dec. 2001. URL http://search.ebscohost.com/login.aspx?direct=true&db=buh&AN=5879096&site=ehost-live.

[128] J. Ohtsubo. Chaos Synchronization and Chaotic Signal Masking in Semiconductor Lasers With Optical Feedback. *Quantum Electronics, IEEE Journal of*, 38(9):1141–1154, Sept. 2002. URL http://search.ebscohost.com/login.aspx?direct=true&db=buh&AN=7398339&site=ehost-live.

[129] S. Kobayashi, J. Yamada, S. Machida, and T. Kimura. Single-Mode Operation of 500 Mbit/s Modulated AlGaAs Semiconductor Laser by Injection Locking. *Electronics Letters*, 16(19): 746–748, Sept. 1980.

[130] S. Inoue, S. Lathi, and Y. Yamamoto. Longitudinal-mode-partition noise and amplitude squeezing in semiconductor lasers. *Journal of the Optical Society of America B*, 14(11):2761–2766, Nov. 1997. URL http://josab.osa.org/abstract.cfm?URI=josab-14-11-2761.

[131] Y. Yamamoto and T. Kimura. Coherent Optical Fiber Transmission Systems. *Quantum Electronics, IEEE Journal of*, 17(6):919–935, Jun. 1981.

[132] M. Bondiou, R. Gabet, G. M. Stéphan, and P. Besnard. Linewidth of an optically injected semiconductor laser. *Journal of Optics B: Quantum and Semiclassical Optics*, 2(1):41, Feb. 2000. URL http://stacks.iop.org/1464-4266/2/i=1/a=307.

[133] D. J. Derickson, P. A. Morton, J. E. Bowers, and R. L. Thornton. Comparison of timing jitter in external and monolithic cavity mode-locked semiconductor lasers. *Applied Physics Letters*, 59 (26):3372–3374, Dec. 1991.

[134] W. Lee, H. Izadpanah, R. Menendez, S. Etemad, and P. J. Delfyett. Synchronized Mode-Locked Semiconductor Lasers and Applications in Coherent Communications. *Lightwave Technology, Journal of*, 26(8):908–921, Apr. 2008.

[135] H. Kurita, T. Shimizu, and H. Yokoyama. Experimental Investigations of Harmonic Synchronization Conditions and Mechanisms of Mode-Locked Laser Diodes Induced by Optical-Pulse Injection. *Selected Topics in Quantum Electronics, IEEE Journal of*, 2(3):508–513, Sept. 1996.

[136] C. Otto, K. Lüdge, A. G. Vladimirov, M. Wolfrum, and E. Schöll. Delay-induced dynamics and jitter reduction of passively mode-locked semiconductor lasers subject to optical feedback. *New Journal of Physics*, 14(11):113033, Nov. 2012. URL http://stacks.iop.org/1367-2630/14/i=11/a=113033.

[137] O. Gat and D. Kielpinski. Frequency comb injection locking of mode locked lasers. *New Journal of Physics*, 15(3):033040, Mar. 2013. URL http://stacks.iop.org/1367-2630/15/i=3/a=033040.

[138] N. Rebrova, T. Habruseva, G. Huyet, and S. P. Hegarty. Stabilization of a passively mode-locked laser by continuous wave optical injection. *Applied Physics Letters*, 97(10):101105, Sept. 2010. URL http://link.aip.org/link/?APL/97/101105/1.

[139] E. Sooudi, S. Sygletos, A. D. Ellis, G. Huyet, J. G. McInerney, F. Lelarge, K. Merghem, R. Rosales, A. Martinez, A. Ramdane, and S. P. Hegarty. Optical Frequency Comb Generation Using Dual-Mode Injection-Locking of Quantum-Dash Mode-Locked Lasers: Properties and Applications. *Quantum Electronics, IEEE Journal of*, 48(10):1327–1338, Aug. 2012.

[140] L. G. Joneckis, P.-T. Ho, and G. L. Burdge. CW Injection Seeding of a Modelocked Semiconductor Laser. *Quantum Electronics, IEEE Journal of*, 27(7):1854–1858, Jul. 1991.

[141] S. Pitois, J. Fatome, and G. Millot. Generation of a 160-GHz transform-limited pedestal-free pulse train through multiwave mixing compression of a dual-frequency beat signal. *Optics Letters*, 27(19):1729–1731, Oct. 2002. URL http://ol.osa.org/abstract.cfm?URI=ol-27-19-1729.

[142] X. Fang, P. K. A. Wai, C. Lu, H. Y. Tam, and X. Dong. High-repetition-rate pulse generation using dual-mode self-injection locking in a Fabry-Perot laser diode. *Optical Engineering*, 49(7): 074201–074201–5, Jul. 2010. URL http://dx.doi.org/10.1117/1.3456597.

[143] M. Schell, A. G. Weber, and D. Bimberg. Hybrid Mode-Locking of Semiconductor Lasers. In *Lasers and Electro-Optics Society Annual Meeting, 1993. LEOS '93 Conference Proceedings. IEEE*, pages 294–295, Nov. 1993.

[144] F. Kefelian, S. O'Donoghue, M.T. Todaro, John G. McInerney, and G. Huyet. RF Linewidth in Monolithic Passively Mode-Locked Semiconductor Laser. *Photonics Technology Letters, IEEE*, 20(16):1405–1407, Aug. 2008.

[145] R. Paschotta. Noise of mode-locked lasers (Part II): timing jitter and other fluctuations. *Applied Physics B*, 79(2):163–173, Jul. 2004. URL http://dx.doi.org/10.1007/s00340-004-1548-9.

[146] Leaf A. Jiang, S.T. Wong, M.E. Grein, E.P. Ippen, and H. Haus. Measuring Timing Jitter with Optical Cross Correlations. *Quantum Electronics, IEEE Journal of*, 38(8):1047–1052, Aug 2002.

[147] R. P. Green, M. Haji, L. Hou, G. Mezosi, R. Dylewicz, and A. E. Kelly. Fast saturable absorption and 10 GHz wavelength conversion in Al-quaternary multiple quantum wells. *Optics Express*, 19(10):9737–9743, May 2011. URL http://www.opticsexpress.org/abstract.cfm?URI=oe-19-10-9737.

[148] I. Petitbon, P. Gallion, G. Debarge, and C. Chabran. Locking Bandwidth and Relaxation Oscillations of an Injection-Locked Semiconductor Laser. *Quantum Electronics, IEEE Journal of*, 24 (2):148–154, Feb. 1988.

[149] C.H. Henry, N.A. Olsson, and N.K. Dutta. Locking Range and Stability of Injection Locked 1.54 µm InGaAsP Semiconductor Lasers. *Quantum Electronics, IEEE Journal of*, 21(8):1152–1156, Aug. 1985.

[150] Jimyung Kim and Peter J. Delfyett. Above threshold spectral dependence of linewidth enhancement factor, optical duration and linear chirp of quantum dot lasers. *Optics Express*, 17(25): 22566–22570, Dec. 2009. URL http://www.opticsexpress.org/abstract.cfm?URI=oe-17-25-22566.

[151] S. Yu, T. F. Krauss, and P. J. R. Laybourn. Mode locking in large monolithic semiconductor ring lasers. *Optical Engineering*, 37 (4):1164–1168, Apr. 1998. URL http://dx.doi.org/10.1117/1.601950.

[152] R. Todt, T. Jacke, R. Laroy, G. Morthier, and M.-C. Amann. Demonstration of Vernier effect tuning in tunable twin-guide laser diodes. *Optoelectronics, IEE Proceedings*, 152(2):66–71, Apr. 2005.

[153] V. Jayaraman, M.E. Heimbuch, L.A. Coldren, and S.P. DenBaars. Widely tunable continuous-wave InGaAsP/InP sampled grating lasers. *Electronics Letters*, 30(18):1492–1494, Sept. 1994.

[154] R. Boeck, N. A. Jaeger, N. Rouger, and L. Chrostowski. Series-coupled silicon racetrack resonators and the Vernier effect: theory and measurement. *Optics Express*, 18(24):25151–25157, Nov. 2010. URL http://www.mina.ubc.ca/files/Optics%20Express%20Published%20Version.PDF.

[155] S. Furst, G. Mezosi, S. Yu, and M. Sorel. Monolithic integration of semiconductor ring lasers with distributed Bragg gratings. In *Lasers and Electro-Optics, 2008 and 2008 Conference on Quantum Electronics and Laser Science. CLEO/QELS 2008. Conference on*, pages 1–2, May 2008.

[156] M. Sorel, P. J. R. Laybourn, G. Giuliani, and S. Donati. Unidirectional bistability in semiconductor waveguide ring lasers. *Applied Physics Letters*, 80(17):3051–3053, Apr. 2002. URL http://www-3.unipv.it/optoele/Giuliani/Backup_2008_09_29/APL%20ring.pdf.

[157] M. Aoki, H. Sano, M. Suzuki, M. Takahashi, K. Uomi, and A. Takai. Novel structure MQW electroabsorption modulator/DFB-laser integrated device fabricated by selective area MOCVD growth. *Electronics Letters*, 27(23):2138–2140, Nov. 1991.

[158] R. Scollo, H. J Lohe, Franck Robin, D. Erni, Emilio Gini, and H. Jäckel. Mode-Locked InP-Based Laser Diode With a Monolithic Integrated UTC Absorber for Subpicosecond Pulse Generation. *Quantum Electronics, IEEE Journal of*, 45(4):322–335, Apr. 2009.

[159] St Griehl, M. Herms, J. Klober, J. R. Niklas, and W. Siegel. New aspects of copper diffusion in semi-insulating gallium arsenide. *Applied Physics Letters*, 69(12):1767–1769, Sept. 1996.

[160] Y. Sun, D.C. Law, and R.F. Hicks. Kinetics of phosphine adsorption and phosphorus desorption from gallium and indium phosphide (0 0 1). *Surface Science*, 540(1):12 – 22, 2003. URL http://www.sciencedirect.com/science/article/pii/S0039602803008343.

[161] K. Itaya, Mark J. Mondry, P.D. Floyd, L.A. Coldren, and James L. Merz. Low Temperature Impurity-Induced Disordering of AlGaInAs/InP Quantum Wells for Long Wavelength Optoelectronic Applications. In *Indium Phosphide and Related Materials, 1995. Conference Proceedings., Seventh International Conference on*, pages 593–596, May 1995.

[162] C.W. Wilmsen, R.W. Kee, J.F. Wager, J. Stannard, and L. Messick. Interface Formation of Deposited Insulator Layers on GaAs and InP. *Thin Solid Films*, 64(1):49–55, Nov. 1979. URL http://www.sciencedirect.com/science/article/pii/004060907990542X. International Conference on Metallurgical Coatings, San Diego, 1979-Part III.

[163] S. Roberts and P. J. Dobson. Evidence for reaction at the Al-SiO_2 interface. *Journal of Physics D: Applied Physics*, 14(3):L17–L22, Mar. 1981. URL http://stacks.iop.org/0022-3727/14/i=3/a=001.

[164] C. N. Cochran and L. M. Foster. Reactions of Gallium with Quartz and with Water Vapor, with Implications in the Synthesis of Gallium Arsenide. *Journal of The Electrochemical Society*, 109(2):149–154, Feb. 1962. URL http://jes.ecsdl.org/content/109/2/149.abstract.

[165] Y. Kaneko, N. Mikoshiba, and T. Yamashita. Preparation of MgO Thin Films by RF Magnetron Sputtering. *Japanese Journal of Applied Physics*, 30(5):1091–1092, May 1991. URL http://jjap.jsap.jp/link?JJAP/30/1091/.

[166] Y.-W. Zhao and H. Suhr. Thin Films of Magnesium Oxide Prepared by Plasma-Enhanced Chemical Vapour Deposition. *Applied Physics A*, 54(5):451–454, May 1992. ISSN 0947-8396. URL http://dx.doi.org/10.1007/BF00324170.

[167] W. Eidelloth, W. J. Gallagher, R. P. Robertazzi, R. H. Koch, B. Oh, and R. L. Sandstrom. Wet etch process for patterning insulators suitable for epitaxial high T_c superconducting thin film multilevel electronic circuits. *Applied Physics Letters*, 59(10):1257–1259, Sept. 1991.

[168] A. Weiner. *Ultrafast Optics*. Wiley Publishing, 2009.

[169] R. Trebino. *Frequency Resolved Optical Gating: the measurement of ultrashort laser pulses*. Kluwer Academic Publishers, 2002.

[170] J. Ratner, G. Steinmeyer, T. C. Wong, R. Bartels, and R. Trebino. Coherent artifact in modern pulse measurements. *Optics Letters*, 37(14):2874–2876, Jul. 2012. URL http://ol.osa.org/abstract.cfm?URI=ol-37-14-2874.

[171] R. Leon, M. Kaminska, Z. Liliental-Weber, K. M. Yu, M. Chandramouli, and E. R. Weber. Semi-Insulating Behavior of Cu Doped InP. In *Indium Phosphide and Related Materials 1991, International Conference on,*, pages 464–467, Apr. 1991.

[172] K. Zdansky, J. Zavadil, L. Pekarek, V. Gorodynskyy, and H. Kozak. Investigation of copper doped InP single crystals grown by Czochralski technique for use in X-ray detection. *physica status solidi (a)*, 202(4):555–560, Mar. 2005. URL http://dx.doi.org/10.1002/pssa.200460420.

[173] K. Zdansky, L. Pekarek, and P. Hlidek. Electronic and Optical Properties of Copper Doped InP Single Crystals. In *Indium Phosphide and Related Materials 2005, International Conference on*, pages 171–174, May 2005.

[174] R. Trebino and D. J. Kane. Using phase retrieval to measure the intensity and phase of ultrashort pulses: frequency-resolved optical gating. *Journal of the Optical Society of America A*, 10(5): 1101–1111, May 1993. URL http://josaa.osa.org/abstract.cfm?URI=josaa-10-5-1101.

COLOPHON

This document was typeset using the typographical look-and-feel `classicthesis` developed by André Miede. The style was inspired by Robert Bringhurst's seminal book on typography "*The Elements of Typographic Style*". `classicthesis` is available for both LaTeX and LyX:

http://code.google.com/p/classicthesis/

Happy users of `classicthesis` usually send a real postcard to the author, a collection of postcards received so far is featured here:

http://postcards.miede.de/

Final Version as of 12th May 2014 (`classicthesis` version 1.0).

VINCENZO PUSINO

HIGH POWER, HIGH FREQUENCY MODE-LOCKED SEMICONDUCTOR LASERS